Synthesis and Characterization of Nanocrystalline Nickel-Zinc Spinel Ferrite Thin Films Using the Spin-Spray Deposition Method

by

Nicole M. Ray

A Dissertation Presented in Partial Fulfillment
of the Requirements for the Degree
Doctor of Philosophy

Approved April 2013 by the
Graduate Supervisory Committee:

William Petuskey, Chair
Rodolfo Diaz
Ralph Chamberlin

ARIZONA STATE UNIVERSITY

May 2013

ABSTRACT

The overall objective of this project is to optimize the development of magnetic ferrite thin films targeted for enabling low-loss broadband communication devices, miniaturized low-microwave inductors and electromagnetic noise suppressors. The focus of this objective is to design and build a reactor and improve the spin-spray process. Each film is then characterized and optimized to have a high permeability and high frequency in the range of 500 MHz – 3 GHz. Films produced by the μ-droplet deposition regime yields a higher Snoek's product than the continuous liquid layer regime. The highest Snoek's product occurs when it is deposited at an oxidant pH of 8.28. The Ni-Zn-Co ferrite magnetic domains were imaged using the Lorentz TEM in which multi-grain domains are experimentally observed for the first time.

ACKNOWLEDGMENTS

I would like to acknowledge my advisor, Professor William T. Petuskey, for all his guidance and support through this research. I would also thank Prof. Rudy Diaz, Prof. Ralph Chamberlin, Prof. Dave Smith, and Prof. Molly McCartney. Additional thanks to my colleagues Dr. Sergio Clavijo, Dr. Heath Lorzel, Blake Rogers, Tom Sebastian, Kaushik Venkata, and Desai Zhang for their time and commitment to this project. I would also like to thank Northrop Grumman and ASU for their support through the years. Finally, and most importantly I would like to thank my family for all their support and encouragement.

TABLE OF CONTENTS

Chapter 1

INTRODUCTION

There a many challenges in thin film science. Conceivably one of the most difficult is growing a dense and well adherent ceramic oxide film, normally produced at high temperatures, onto a plastic substrate at low temperatures. With the continued down scaling of device dimensions and increased demand for system-on-chip (SOC), applications are driving significant improvement in performance with lower fabrication cost. There is a lot of room to improve the performance for high frequency circuits from the passive circuits, such as transmission lines and capacitors through reducing losses at high frequency.

APPLICATIONS

The major objective of this research is to develop magnetic ferrite thin films for applications relating to low-loss broadband communication devices, miniature low-microwave inductors and electromagnetic noise suppressors. This project integrates fundamental materials research with materials development targeted towards optimizing synthesis for achieving desired properties of high permeability, low core losses, high density films, and low temperature synthesis. Success of this project is measured by demonstrating the nanostructural properties of spinel ferrites, such as nickel zinc cobalt ferrite, $(Ni^{2+}, Zn^{2+}, Co^{2+}, Fe^{2+,\,3+})_3O_4$, or magnetite, $(Fe^{2+}, Fe^{3+})_3O_4$, capable of enhancing the sensitivity and versatility of RF antennas while providing the significant advantage of synthesizing at low temperatures, thus enabling the use of polymer substrates [1, 2].

Global positioning systems (GPS), and synthetic aperture radar (SAR) require a dual-band, or tri-band antenna which would benefit from avoiding the use of two different antennas. Microstrip antennas (i.e. patch antennas) are of great interest for wireless and mobile applications due to their physical characteristics [1]. Patch antennas are light weight, low volume, a flexible design, low sensitivity to manufacturing tolerances, and are easy to install [1].

RESEARCH OBJECTIVES

There are four main objectives in this research study, which control the focus of this project. They are:

- How does the pH effect the texturing and composition of the thin films?
- Is there a correlation between texturing and electromagnetic properties?
- How does Snoek's product change after annealing at high temperature?
- What happens to the magnetite microstructure and morphology after annealing?

The section on research methodology explains the process in which the research objectives have been executed, thus far.

CLASSIFICATION OF FERRITES

Ferrites, specifically the spinel ferrite structure, belong to a unique crystal structure, shown in Fig. 1. It is a structurally isotropic material belonging to the cubic Bravais lattice with an *fd3m* space group [3]. This general formula is AB_2O_4, where (A)

and (B) are metal cations and oxygen as the anion. Magnetite and nickel zinc ferrites are suitable candidates among many for high frequency applications such as transformer cores and antenna applications.

Normal Spinel.

A normal spinel ferrite has eight divalent ions in the eight available tetrahedral sites (A site) and the sixteen trivalent ions occupying the sixteen octahedral sites (B site) [4]. The oxygen ions are in the face-centered cubic configuration. An example of a normal spinel is magnesium aluminate, $MgAl_2O_4$, which is used for applications in refractory, electromagnetic windows and transparent armor. The magnesium ions are formally located on the tetrahedral sites, and the aluminum ions are located on the octahedral sites. Fig. 1. shows the magnesium aluminate spinel in the normal spinel crystal structure form. At high temperatures, however, there is significant mixing of magnesium and aluminum between the two cation sites, which gives rise to magnesium/aluminum stoichiometry. The composition of magnesium aluminate spinel is known to range from MgO-rich to Al_2O_3-rich compositions.

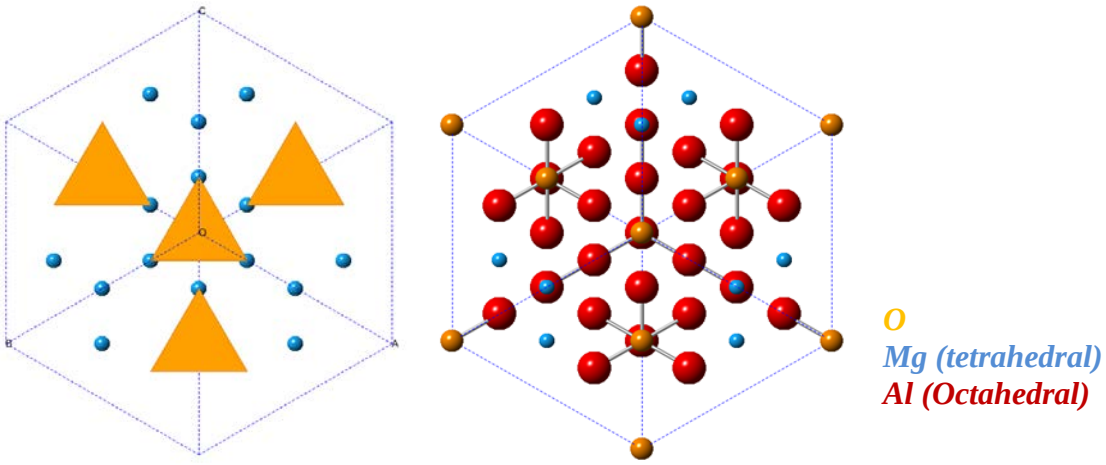

Fig. 1. Normal spinel in [111] direction.

Inverse Spinel.

Nickel zinc ferrite is an inverse spinel, where iron has two different oxidation states, Fe^{2+} and Fe^{3+}, which occupy different lattice sites. The inverse spinel space group consists of 56 atoms, in which 32 are oxygen anions in a close packed cubic structure, and the remainder atoms are metal cations residing on eight of the 64 available tetrahedral sites (A site) and 16 of the 32 available octahedral sites (B sites) [3]. Divalent cations (Ni^{2+}, Zn^{2+}, and Co^{2+}) occupy the octahedral sites, while half of the trivalent cations (Fe^{3+}) occupy the tetrahedral sites (A sites) and the rest occupy the octahedral sites (B sites). The size and valence of the cation species determines the filling of these sites which strongly influence the magnetic and electronic properties[3]. Due to cation disordering of the spinel structure, the lattice parameter (α) is slightly large, α = 8.36Å, which is discussed in later chapters.

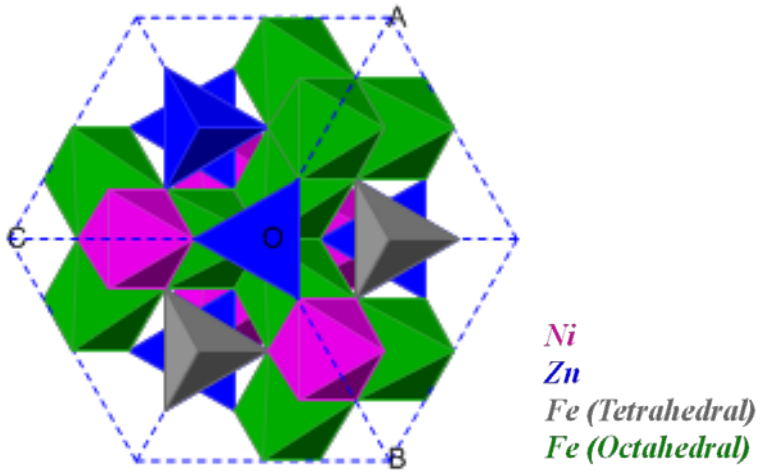

Fig. 2. Inverse spinel ferrite crystal structure.

SOFT FERRITES

In recent studies, high frequency soft magnetic nanoferrites have received a great deal of attention due to their low conductivity properties. For high frequency applications, magnetic insulators are the material choice for their high permeability, low coercivity, and high saturation magnetization. Soft ferrites first became commercially available in 1945, the first introduced was magnetite. Although, its conductivity is relatively high compared to ferrite compositions with fully oxidized iron (Fe^{3+}). The cubic or soft ferrites all have the same general chemical formula, $MO - Fe_2O_3$ where M is a transition metal such as nickel, zinc, manganese, iron, or magnesium. [5]

Soft ferrites are further broken down into two categories according to their frequency range. In the frequency ranges from audio up to 500 MHz, they are classified as ‘non-microwave ferrites,’ and, for frequencies ranging from 100 MHz to 500 GHz, they are classified as ‘microwave ferrites.’ In the case of spin-spray deposition at low

temperatures microwave ferrites are chosen for their frequency range and high permeability properties. [5]

High Frequency.

For high frequency materials, the eddy currency effect is very important to the overall properties [6]. As the frequency rises, the skin depth becomes thinner, in which the alternating magnetic flux can penetrate [6]. In order to diminish these losses small grain sizes are needed. From Snoek's theory in 1948, Snoek suggested there is a compromise between small grains with low losses at high frequencies; and for large grains at low frequencies [6]. Thus, he proposed a limiting value law correlating with the product of the frequency and permeability reaches a limiting value. A way of examining the problem is to plot the complex permeability, μ' and μ", as a function of frequency. From experimental analysis it has been found at lower frequencies the losses are greater and the permeability is higher [4, 7]. To overcome these limitations, a material with a preferred plane, rather than a preferred direction is developed, it is referred to as Ferroxplana (spinel) ferrite which, for these materials, typically operates between 800 MHz and 1.6 GHz [6, 8].

Nickel Zinc Ferrite.

Nickel zinc ferrite is the often chosen due to its high permeability and high frequency capabilities found in literature [9]. As pointed out by Jacob L. Snoek, an ideal ferrite used for high frequency should not have too high of a permeability, have a high

saturation magnetization, contain no ferrous iron, and have a dense structure, which falls within the parameters of nickel zinc ferrite [7]. In order to contain little to no ferrous iron and have a dense structure, the material must form at a low temperature, around 70-100°C [7]. The spin-spray deposition method is designed to meet the low temperature requirements and still maintain uniform thin film deposition in a controlled atmosphere [10].

Nickel zinc spinel ferrite has proven in journal articles to exceed Snoek's limit [9, 11-13]. In 1948 J. L. Snoek first derived the limit for multiple bulk oxides to understand how well the material performed. He developed an equation using the data collected from his experiments on magnetite (Fe_3O_4) for bulk materials in which he described how well this material performs, called Snoek's product, and is described in Eqn. (6).

Magnetite samples were made by reducing pressed bars of hematite (Fe_2O_3) at 1300ºC in a nitrogen atmosphere [7]. There were two maxima unmistakably found for initial permeability; one lies just below the Curie point, the second lies just above the point where the magnetic anisotropy for magnetite changes its character [7]. However, this profile only represents the initial permeability it does not show the frequency, see Fig. 3 [7].

$$Snoek's\ Product\ (GHz) = f(Hz) * (\mu_{DC} - 1) \tag{6}$$

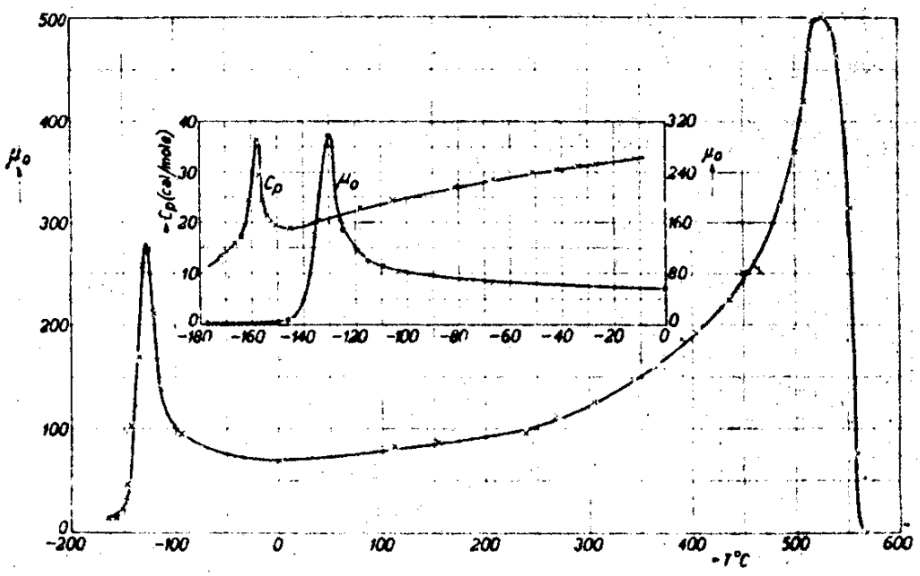

Fig. 3. μ_0 versus Temperature (°C) for magnetite (Fe_3O_4), prepared by the reduction of Fe_2O_3 in nitrogen at 1300 °C [7].

This implies an inverse relationship between *f* and μ_{DC} assuming that Snoek's product is constant for a class and composition of a ferrite material. In general for spinel ferrites, when the peak of the loss curve is at a low frequency the higher the initial permeability, μ_0, will measure. High permeability ferrites could be used as cores for a small frequency range. Figure 4 below shows a typical plot for the complex permeability of bulk polycrystalline Ni-Zn ferrites [4]. Here, the initial real part, μ', and the imaginary part of the complex permeabilities are a function of frequency for different compositions of nickel and zinc. In general μ' at low frequencies tend to be very high. However, its magnitude decreases for ferrites of greater resonance frequency, as indicated by the peak in μ".

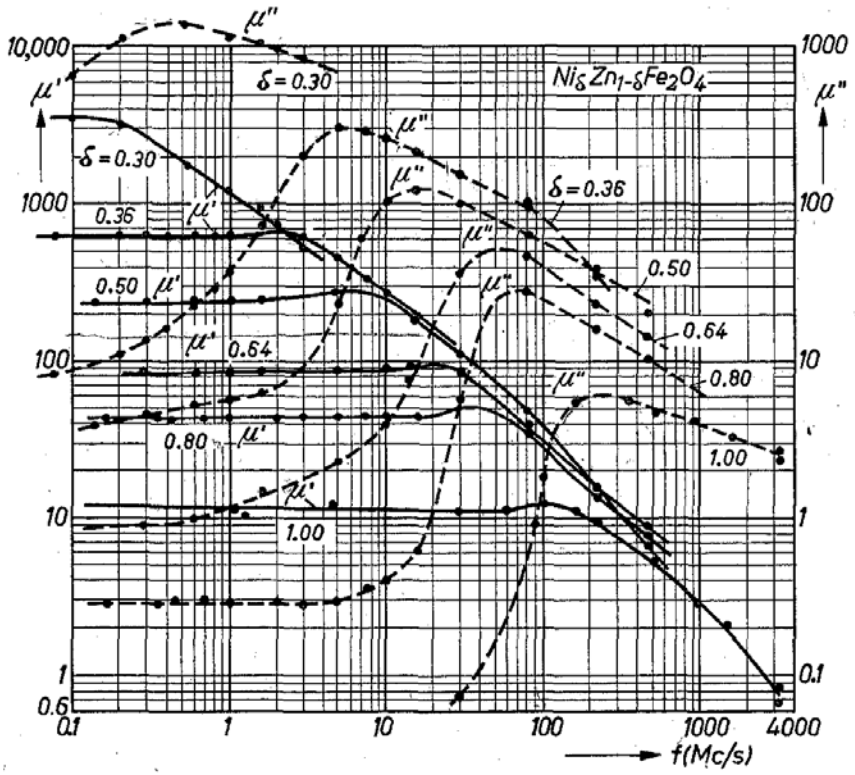

Fig. 4. Frequency dependence of the real and imaginary parts of initial permeability, μ'and μ"respectively for polycrystalline ferrites [4].

In 1969, De Lau found that Ni-Zn-Co ferrite properties could be improved significantly by reducing the grain sizes. That is the Snoek's product could be raised. It greatly affected the frequency just below the ferromagnetic resonance frequency and it further reduced domain wall motion [6]. Moreover, De Lau found that with the addition of small amounts of Co^{2+} and Co^{3+} in iron deficient Ni-Zn ferrite decreases domain wall motion in response to magnetization orientation process and related losses in high frequency magnetic fields of diminutive amplitude [14]. The Co^{2+} ions will preferentially

occupy on the octahedral sites leading to domain wall stabilization. The distribution over the octahedral sites affected the exchange of electrons between Co^{2+} and Co^{3+}, and changed the magnetic domain pattern, associated with reorganizing following the reorganization of the Co^{2+} ions [14].

In Ni-Zn ferrites which do not contain cobalt, a reduction in grain size leads to a decrease in the domain wall permeability and the corresponding losses. In Fig. 5, De Lau shows that by reducing the grain size below 1 μm the high frequency properties of Ni-Zn ferrites can be improved. Dense, polycrystalline samples were fabricated by hot pressing technique.

Spin spray deposition techniques display the same characteristics with the addition of Co^{2+} and Co^{3+} ions. The frequency ranges from 500 MHz to 1 GHz, and the complex permeability, μ', ranges from 20 – 60, as shown in Fig. 6. The vast difference between De Lau Ni-Zn-Co ferrite bulk samples and the spin-spray deposition technique is the grain size. De Lau's grain sizes were on the order of 1 μm in using the hot pressed samples, while the spin-spray deposition technique yield grains as small at 10 nm to 60 nm.

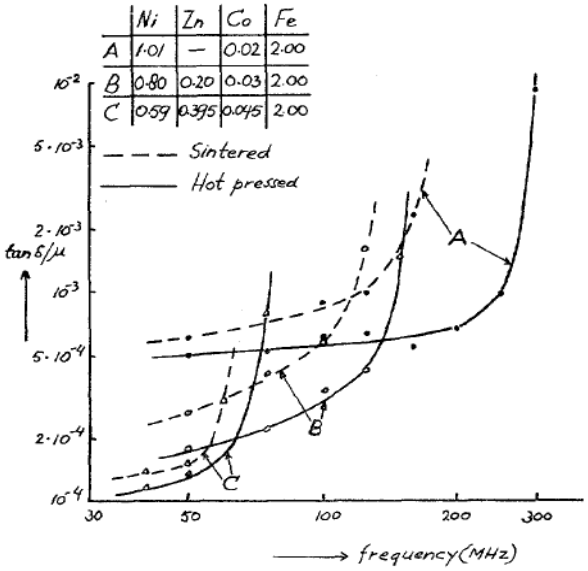

Fig. 5. High frequency properties of bulk Ni-Zn ferrite prepared by continuous hot pressing [14].

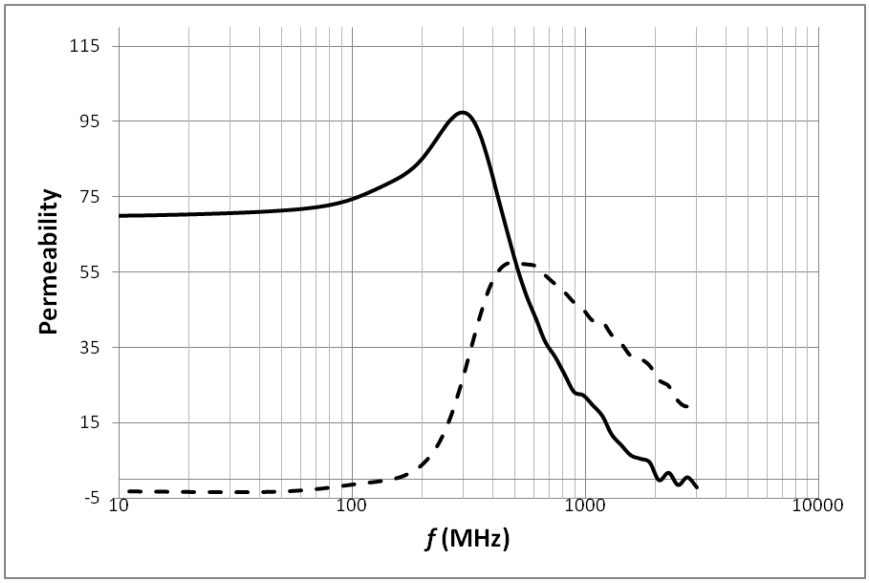

Fig. 6. Permeability spectrum for $Ni_{0.19}Zn_{0.39}Co_{0.05}Fe_{2.38}O_4$.

In 2002, Abe *et al*. was the first group to report depositing a Ni-Zn spinel ferrite thin film with a high permeability and high frequency using a newly developed technique called ferrite plating [15]. This technique exceeded Snoek's limit for bulk materials, which was 18.45 GHz when the resonant frequency is taken at the inflection point in μ', shown in Fig. 7.

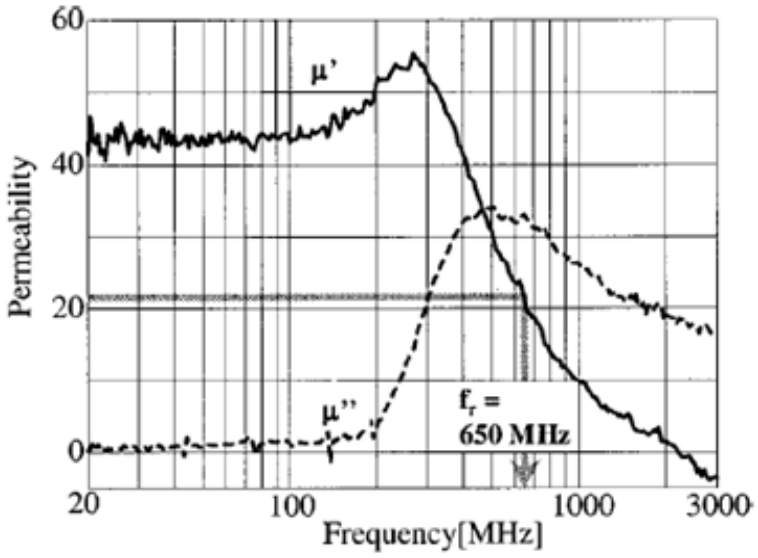

Fig. 7. First documented high permeability, high frequency Ni-Zn ferrite exceeding Snoek's limit [15].

LITERATURE REVIEW

In 1835, Justus Freiherr von Liebig first deposited a thin film of silver using chemical solution deposition (CSD) in the presence of a reducing species, such as formaldehyde. This famous reaction, in the electroless deposition community, is considered to be one of the first examples of a chemical bath deposition. Since, there

have been nearly hundreds of materials deposited by CBD from chalcogenides, oxides and other non-metallic compounds. Early nickel zinc ferrite depositions began using CSD as early as 1983 and electroless deposition techniques discussed in later sections.

The work of Abe & Matsushita et al.

Masanori Abe and Nobuhiro Matsushita were the first research scientists to spin-spray plate magnetite thin films at low temperatures [16]. Abe *et al*. first attempted depositing Ni-Zn ferrites by electrodeposition method published in 1983, seen using the apparatus Fig. 8 [10, 16]. Figure 8 illustrates the reaction vessel and apparatus used in ferrite deposition. The ferrite-plating method promotes the growth and formation of spinel ferrite films. The electroless method deposits films at high deposition rates, 2 μm/min, and only is capable of depositing on metal substrates. Therefore, Abe *et al*. re-engineered the method using ultrasonic energy, and then later a process called spin-spray deposition.

Later they developed a two reactant approach that was enhanced by ultrasonic energy in Fig. 9. The substrate is immersed into an electrolyte solution of in this case with a metal chlorides (Fe^{2+} and M^{2+}), and hydrolyzing the substrate surface. The reaction is accomplished by introducing a reducing agent which releases hydrogen from the surface of the substrate, leaving a negative charge on the surface. Some of the adsorbed $FeOH^{+}$ ions are oxidized to $FeOH^{2+}$ ions which cause ferrite formation. Equation 1 shows the formation of spinel ferrite, or $(M^{2+}, Fe^{2+}, Fe^{3+})_3O_4$.

$$\mathbf{x}FeOH^{2+} + \mathbf{y}FeOH^{+} + zMOH^{(n-1)} + OH^{-}$$

$$\rightarrow (Fe^{3+}, Fe^{2+}, M^{n+})_3O_4 + 4H^{+} \quad (1)$$

Where $(x + y + z = 3)$

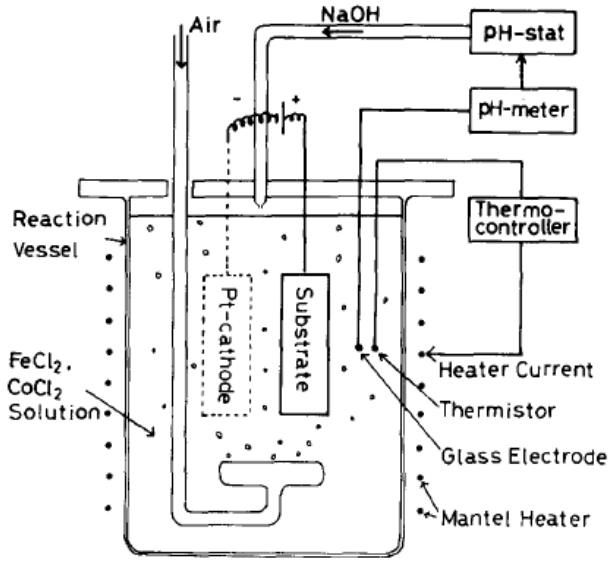

Fig. 8. Electrodeposition method used for ferrite plating by Abe *et al*. [16, 17].

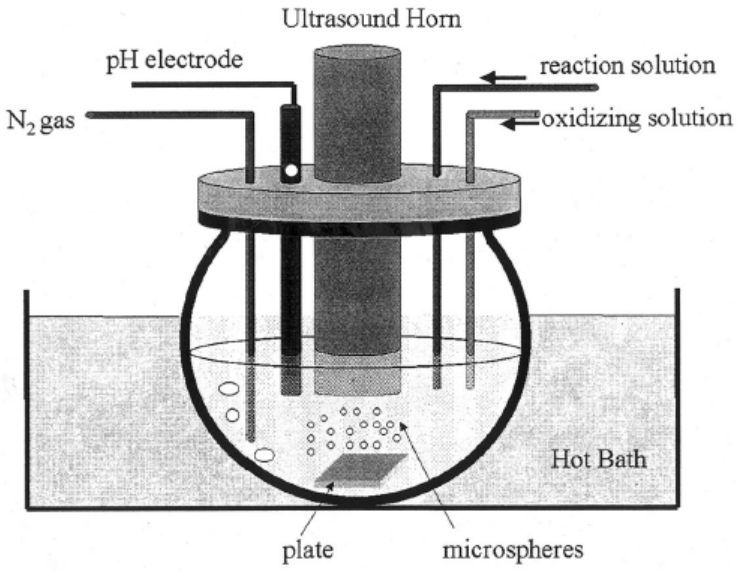

Fig. 9. Ultrasound-enhanced ferrite plating method [17].

Following the electroless plating method, Abe et al. proposed to use ultrasound in order to encapsulate polyacrylate microspheres with ferrite thin film coatings. Figure 9 represents the Ultrasound-enhanced ferrite plating method first published in 1997 [18]. The microspheres, about 4.5 microns in diameter, were dispersed in the reactant solution and exposed to the oxidizing solution, sodium nitrite, which was introduced via an injection port [17]. Ultrasound waves were turned on (19.4 KHz, 600 W) [17, 18]. The solution was kept at a low temperature, 70ºC and at a mildly acidic pH = 6.0 by adding ammonium acetate [17]. The advantage of this method was the round bottom shape of the vessel which prevented sedimentation of the particles around the corners of the flat bottom, and thus producing uniform ferrite encapsulation of the particles [18]. The second advantage was that by buffering the solution to pH = 6.0 the system was more

stable and allowed for finer grain growth [18]. The magnetic properties at this point were not measured until the process was improved [17].

The third method was an improved spin-spray plating process onto a spinning heated platen using alternating aqueous solutions, seen in Fig. 10 [11]. The Ni-Zn-Co ferrite films were deposited onto glass and polyimide substrates by simultaneously spraying the reactant and oxidizing solution onto the substrate from 70-100ºC [16, 19]. The solutions were sprayed at a rate of 40-80 mL/min on an 8" platen, while at a rate of 150 rpm [19]. The reactant solution consisted of iron chloride tetrahydrate ($FeCl_2 \cdot 4H_2O$), nickel chloride hexahydrate ($NiCl_2 \cdot 6H_2O$), cobalt chloride hexahydrate ($CoCl_2 \cdot 6H_2O$) and zinc chloride ($ZnCl_2$). The oxidant is an aqueous solution containing glacial acetic acid (CH_3COOH), sodium nitrite ($NaNO_2$), and ammonium hydroxide (NH_4OH) for pH balance. Abe and Matsushita exhibited exceptional properties for Ni-Zn ferrite and Ni-Zn-Co ferrite films [17, 20]. The high complex permeability, μ, ranges from 20 to 120 at a resonance frequency of 100 MHz to 3.3 GHz [2, 17, 20]. An example is seen in Fig 11, which shows both the film microstructure and the complex permeability.

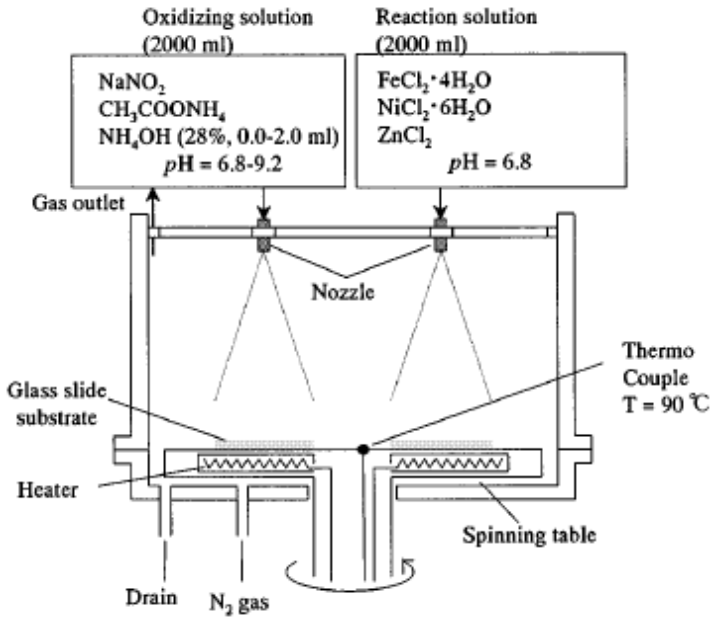

Fig. 10. Spin-spray plating method [11].

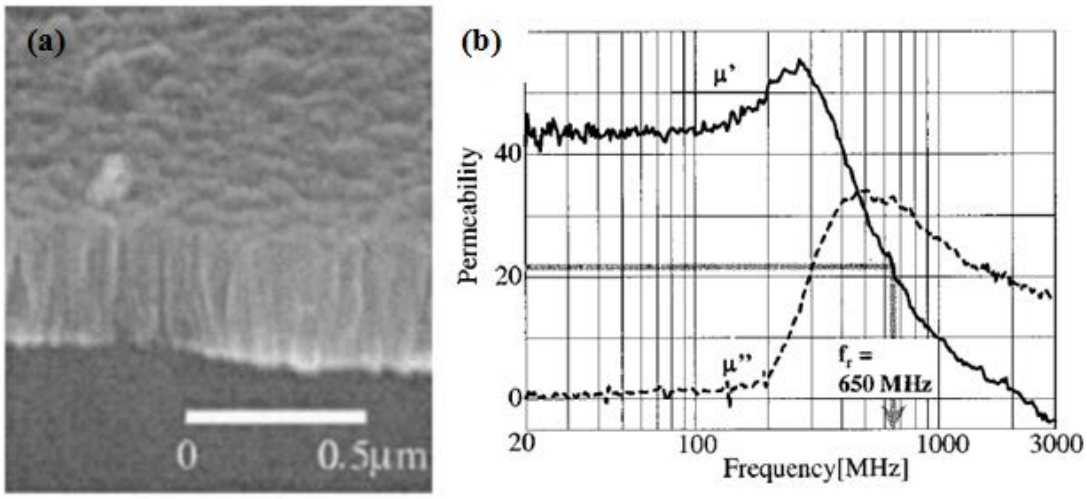

Fig. 11. Spinel thin film ferrite, $Ni_{0.19}Zn_{0.23}Fe_{2.58}O_4$, displaying a (a) columnar structure and its (b) real and imaginary permeability [15].

The saturation magnetization for these ferrites ranges from 170 – 580 emu/cc and the coercivity 30 – 200 Oe depending on the grain size and position (radial or perpendicular) of the sample. The exceptional electrical and magnetic properties have been attributed to columnar structure and crystalline morphology of the thin films.

Presently, Matsushita *et al*. are depositing zinc oxide (ZnO) rod arrays via the spin spray plating process on non-seeded glass substrates [21]. ZnO is a wide band gap semiconductor, which has attractive physical and chemical properties with respect to optical absorption and emission, piezoelectricity, high electrical conductivity, and catalytic activity [21]. The reason for using ZnO as a possible material for these applications is the tunable properties such as morphology, size, surface area, and crystalline orientation [21].

The Work of Lubitz *et al*.

In 1994, P.J. van der Zaag, P. Lubitz, and M. Abe began annealing experiments on Mn-Zn ferrite and Ni-Zn ferrite samples. The material of most interest was Ni-Zn spinel ferrite, because of their magnetic character and high resistivity for microwave inductor or micromagnetic device applications [22, 23]. Until 1994, most reports in literature on ferrite plating have involved structural quality of deposited films and the magnetic parameters, such as saturation magnetization, M_s, and coercivity, H_c. However, most applications require a high initial permeability, μ_i. Hence, Lubitz *et al.* began studying techniques to increase the initial permeability.

Lubitz *et al*. conducted annealing experiments on specimens from the spin-spray method developed by Abe *et al*. in 1993[24]. The films were 0.5 – 2 microns thick with varied nickel and zinc compositions. The samples in the first set of experiments were annealed to 500ºC for 30 minutes[23]. Figure 12 shows the effect annealing has on dielectric loss at 9.5 GHz. The transition observed for the dielectric losses following the annealing experiments is the specimens normalizing to their pre-annealed values, about 0.2, at a relatively low annealing temperature, 325ºC for 30 minutes [23]. This is effect is associated primarily with annealing temperature [23].

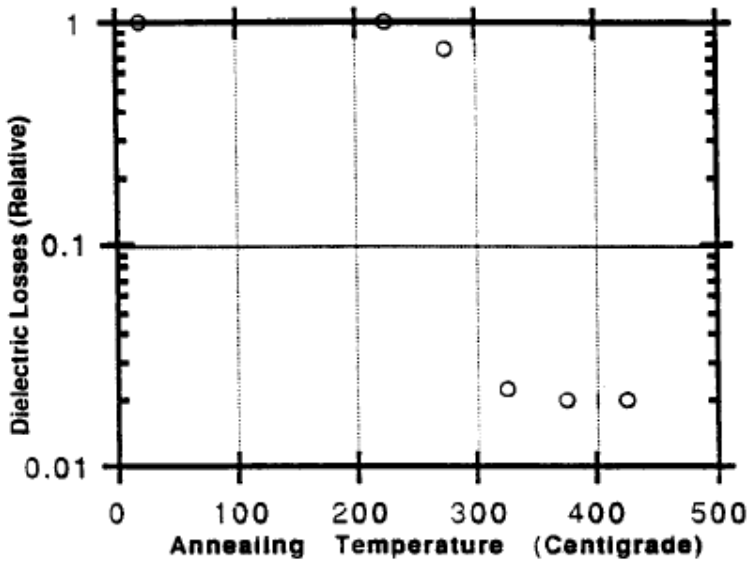

Fig. 12. Annealing effect of a thin film ferrite, composition $Ni_{0.34}Zn_{0.18}Fe_{2.48}O_4$, on (a) dielectric losses at 9.5 GHz [23].

Thus far, most reports in literature on ferrite films deal with the structural quality and magnetic parameters of thin film ferrites[22]. In 1999, Lubitz *et al*. performed experiments in order to increase the initial permeability. He first tested $Ni_{0.17}Zn_{0.38}Fe_{2.45}O_4$ films using the spin-spray ferrite plating method at 80ºC on glass substrates using the procedure outlined by Zhang *et al*. method [24]. Next, the thin film samples were annealed to 500ºC for 30 minutes in air [22]. The initial permeabilities of the as-deposited and the annealed specimens were measured, as shown in Fig. 13. It is found that the initial permeability was strongly dependant on microstructure and thickness [22]. The mean grain size was 0.25 ± 0.01 μm, since the grain size is relatively small compared to the data of bulk Ni-Zn ferrite, the permeability is expected to be low. However, the measured initial permeabilities were comparable to bulk Ni-Zn ferrite and increased when annealed [22]. The high value in permeability has been attributed to the low temperature deposition, limiting the adverse magnetostrictive effects between the substrate and film [22]. Other reasons for the high permeability were the grain size and microstructure. These are record high values for Ni-Zn ferrite films deposited on glass substrates recorded in literature for initial permeability [22].

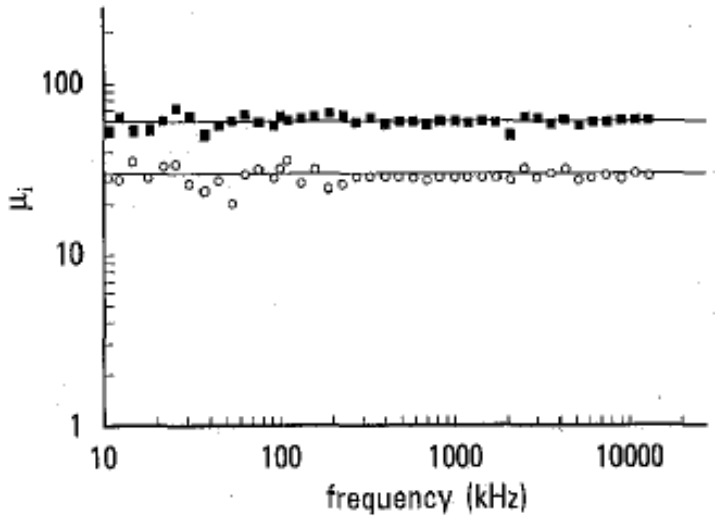

Fig. 13. Initial permeability measured for as-deposited (o) and annealed (▪) $Ni_{0.17}Zn_{0.38}Fe_{2.45}O_4$ films [22].

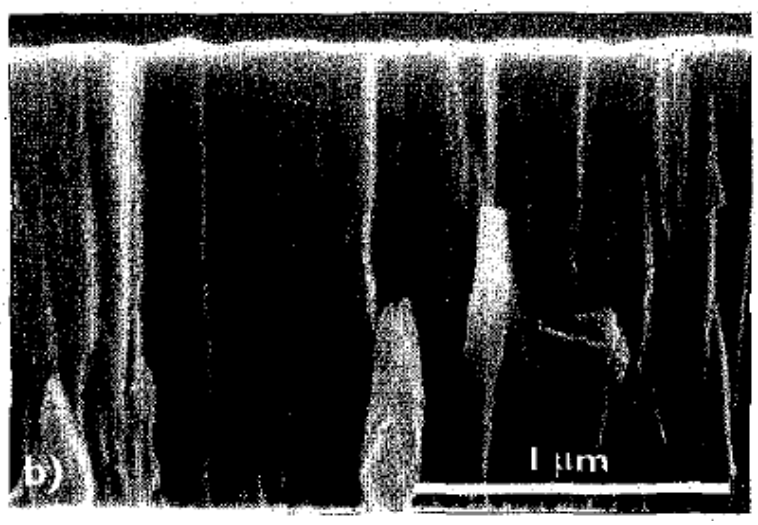

Fig. 14. Columnar structure for $Ni_{0.17}Zn_{0.38}Fe_{2.45}O_4$ film that exhibited as-deposited μ_i = 28 ± 3 and annealed μ_i = 60 ± 5 [22].

The Work of Sun *et al*.

In 1999, Sun et al. wrote a popular publication on thermodynamic-based grain-size limit of polycrystalline materials, specifically for bulk amorphous selenium [25]. He extrapolated data points from an enthalpy equation, shown below in Eqn. (2), which showed a linear relationship between the enthalpy of crystallization, ΔH^{cryst}, and the reciprocal of grain size, 1/d [25].

$$\Delta H^{cryst} = \Delta H^{l-c} + 2\gamma g V_m / d \quad (2)$$

Where γ is the grain-boundary enthalpy, g is the geometry factor, V_m is the molar volume, and d is the average grain size. The purposes of the derivations were to find the lower limit of polycrystalline materials. The lower limit grain-size limit (GSL) for polycrystalline selenium was established to be 4.0 nm [25].

In 2008, Sun *et al*. published a paper on spin-spray deposited multiferroic composites with strong surface adhesion. These materials have two constituent phases of ferro-ferrimagnetic and ferroelectric phases, and possible applications in multifunctional devices. Typical ferroelectric materials, such as lead zirconate titanate (PZT), are good suppliers of OH- groups on the surface, which assists in the ferrite film formation through spin-spray deposition [26]. $Ni_{0.23}Fe_{2.77}O_4$ (NFO) / Pb (Zr,Ti)O_3 is a multiferroic composite obtained by spin spray depositing NFO on a PZT substrate at 90º [26]. These films displayed a strong interface adhesion and excellent wetting between NFO and PZT

as observed using high resolution transmission electron microscopy (HRTEM), seen in Fig. 15. These films have also displayed strong magnetoelectric coupling (ME coupling).

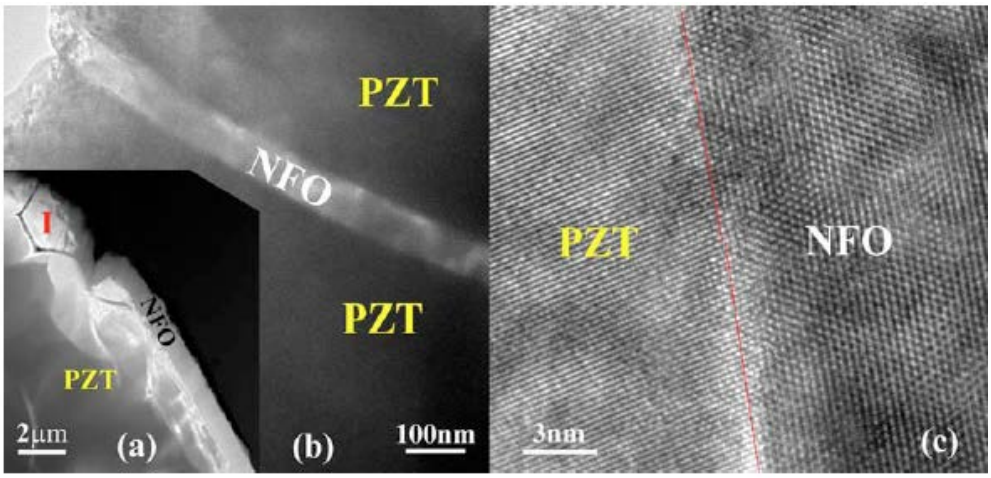

Fig. 15. Cross-sectional image of NFO/PZT (a) HSTEM of Ni-Ferrite growing in PZT crack (b) and HRTEM image ferrite and (C) PZT interface [26].

FERRITE PROCESSING METHODS

There are many different processing methods for spinel ferrites, that can be categorized as conventional and non-conventional. Spin-spray plating is a non-conventional processing type, this section will cover most non-conventional processing methods. Other such methods are described below.

Coprecipitation.

Coprecipitation is simple in that a solute precipitates out of solution from a liquid carrier that facilitates the containing and reaction of reactants, that bind together [6]. It is not used in commercial applications, or on large scales heavily because of output percentage [6]. The precipitates can take the form of hydroxides, oxalates, or carbonates to later be thermally decomposed to the comparable oxide [6]. The advantages of use the coprecipitation method is greater homogeneity, greater reactivity, high purity, fine, particle size, and the calcining step is eliminated [6].

Sol-Gel Synthesis.

Sol-gel synthesis is a wet-chemical technique in which small colloidal particles are suspended in a solution (*sol*), usually by hydrolysis [6, 27]. The *sol* acts as a precursor for an integrated network (*gel*) of particles[6, 27]. Typical precursors are metal salts, such as iron chloride tetrahydrate [6, 27]. After they link together they form a *gel*, or ceramic particles, and further processing is needed to obtain the ceramic particles, such as centrifuging or burning off the precursor [6].

Chemical Vapor Deposition.

Chemical vapor deposition, or CVD, is a chemical process in which the substrate is exposed to volatile precursors that thermally react and decompose on the substrate surface developing solid thin films [6, 28]. The advantages of using CVD is superior conformality, high throughput, high deposition rate, and cleanliness (depositing only

films) [6, 28]. CVD processing is also a scalable process which is commonly used in industry, however it is very expensive compared to other techniques [6, 28].

Chapter 2

EXPERIMENTAL METHODOLOGY

SPIN-DISC REACTOR

Spinel ferrite thin films are produced using aqueous solutions for a thin film deposition method known as spin-spray plating, a.k.a. ferrite plating method as described by Matsushita *et al.* [29]. This is a scalable, low temperature (70-100ºC) process capable of adjusting the composition, rotation rate, flow rates, temperature, different types of substrates, including polymers (i.e. polyether ether ketone, glass, polyimide film, and single crystalline substrates). The spin-spray process consists of many steps shown in the flow diagram on the next page.

The spin disc reactor (SDR) consists of a rotating platen which is contained in a stainless steel chamber. The platen has low temperature heating capabilities up to 300ºC. Inside the chamber there is a polytetrafluoroethylene (PTFE) seal protecting the cast iron shaft, rotating the platen, from corroding. There are three outlets in the chamber; two are for the waste from the reaction solutions and the other is to circulate nitrogen through the chamber. The chamber cover is made from poly methyl methacrylate with holes drilled through for the nebulizer inputs and nitrogen purge. Figure 16 represents a flow chart of the spin-spray process, including characterization and post-processing.

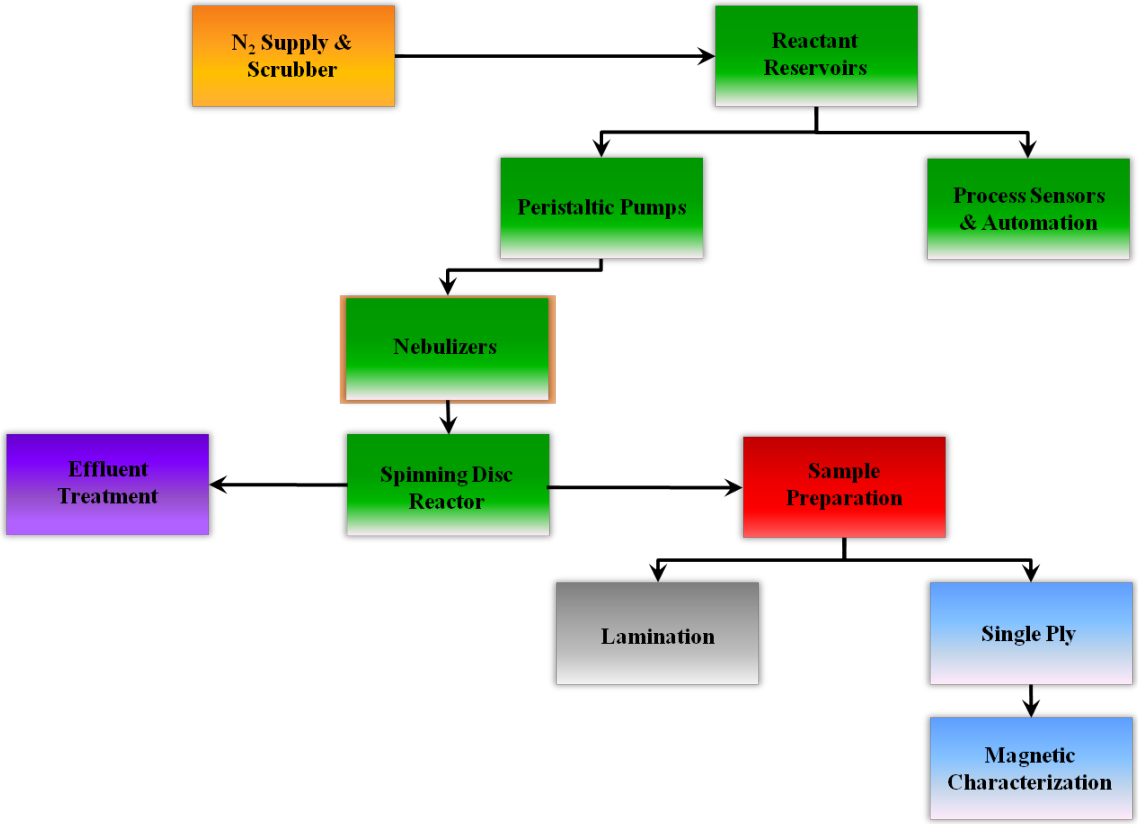

Fig. 16. Flow chart for spin-spray process [30].

Two peristaltic pumps (Gilson Minipuls 3, Middleton, WI) control the flow rate of the atomizing nebulizers from the large liquid reaction vessels. The nitrogen that supplies the nebulizers is used as a purge into the containment chamber and fed through a NO_x scrubber to rid the nitrogen of contaminants. As seen in Figs. 17 and 18, SDR 3.0 is automated using Signal Express from National Instruments. It records the platen rotation rate, pH, average power output, temperature of platen, and temperature of the chamber are recorded in real time during the experiment.

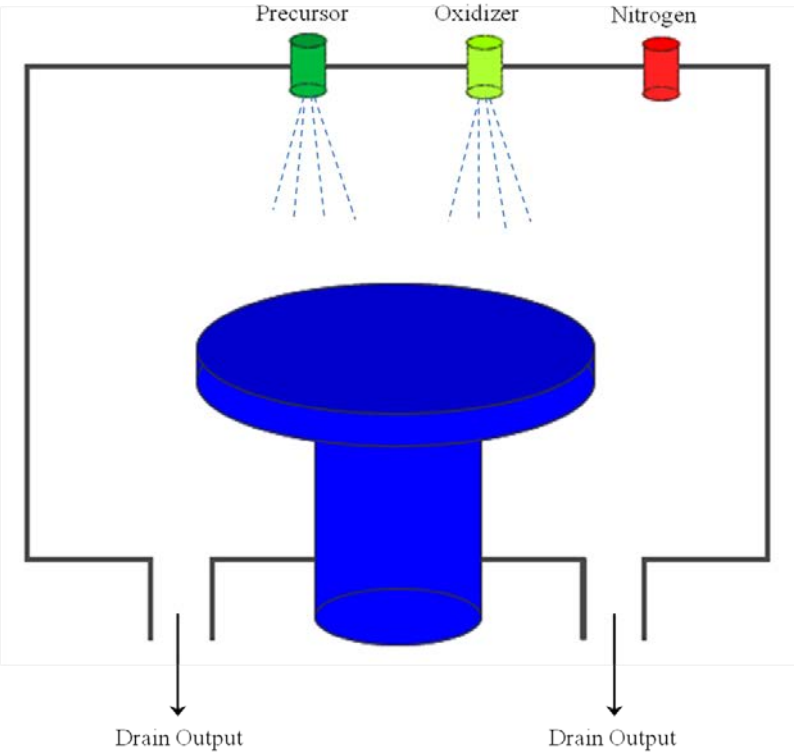

Fig. 17. SDR used for spin-spray deposition.

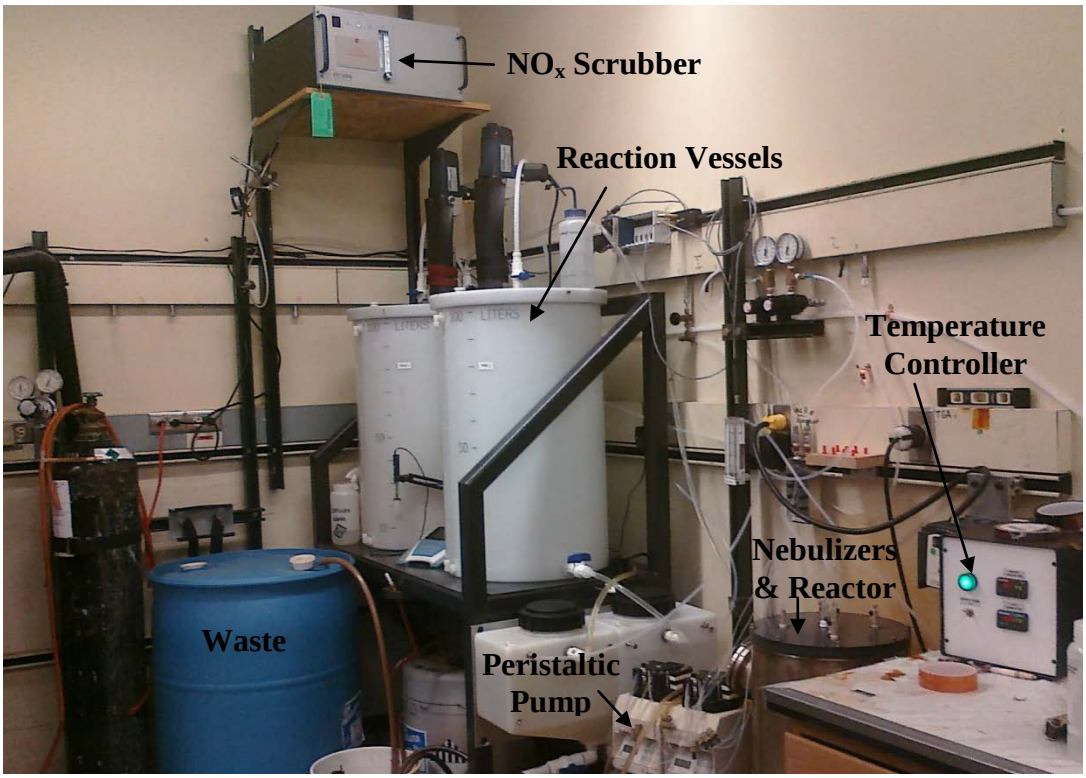

Fig. 18. Image of SDR 3.0 set-up with large containment vessels.

After the equipment is set-up, the platen is thoroughly cleaned with deionized water and acetone. The substrate is positioned on the platen and cleaned with deionized water and acetone, as well. Since this is a low temperature process many different substrates can be used, such as polyimide film, glass, silicon wafers, thermoplastic film and mica. All of these substrates have been used successfully; however glass (quartz) and thermoplastic films are usually used in order to test the permeability and anneal samples.

Understanding the precise parameters for each experiment is crucial for controlling film properties. Using the spin-spray deposition method the polymer substrates are attached to the heated platen (70-100ºC) using polyimide tape. The platen

rotates between 90 - 300 rpm while the reactant and oxidant alternately spray the substrate at a flow rate of 30 - 100 mL/min depending on the experimental conditions. Introducing nitrogen into the system is important on many levels. The nitrogen prevents the aqueous solutions from oxidizing, atomizes the liquid solutions, prevents the shaft from corroding, and assists in forcing the liquids off the platen. The spinel ferrite layer then builds up via either the sequential reaction theory or the μ-droplet collision theory depending on how the reactor is set-up.

The reaction vessels are filled with two different solutions, a metal chloride and an oxidizing solution. The precursor (metal chloride) solution consists of iron chloride tetrahydrate, nickel chloride hexahydrate, zinc chloride, and cobalt chloride hexahydrate. The oxidizing solution is a mixture of sodium nitrite ($NaNO_2$), which acts as the oxidant, glacial acetic acid (CH_3COONH_4) and ammonium hydroxide (NaOH), which buffers the solution ranging from 7-11.

It is also very important to use nanopure deionized and deaired water (18.2 MΩ) during the fabrication process, otherwise the ferrite oxidizes into hydrated iron (III) oxide, because of the molecular O_2 otherwise which is normally present when is exposed to air. When the deposition is completed, distilled water is pumped through the entire system, washing the vessel, tubing, nebulizers and thin films for at least 20 minutes. After the films are washed and cooled down the top is taken off and the nitrogen is blown carefully on the films to dry them off.

REACTION CHEMISTRY AND METHODOLOGIES

This section discusses the aqueous chemistry of the spin-spray deposition method used by the sequential reaction approach operating under the microdroplet regime parameters.

Solubility.

Figure 19 shows the solubility of nickel, zinc, and iron oxide in water at 25°C. The plot below has been produced at room temperature using FactSage®, which is a software program with a fully integrated database used for computing thermodynamic calculations. The effective pH is 6.0 for each experiment but can range from 4.0 – 8.0. For each of the curves, NaOH is used as a base to modify the pH; and for each of the reactants metal chlorides are inputted into the calculations with the correct stoichiometry. Note that the database used does not have data for $Ni(OH)_2^0$ or for $Zn(OH)_2^0$. Due to the absence of $Ni(OH)_2^0$ in the database the NiO curve begins to curve upwards above a pH of 10.75 instead of leveling out [31]. In the ZnO curve, at an effective pH above 8.5, $Zn(NH)_4$ complexes can become present due to the aqueous chemistry in the oxidant, and the solid phase deposition rate decreases [21]. For iron oxide the curve is constant between pH's 5.6 and 7.0, and then steadily decreases, seen in Fig. 19.

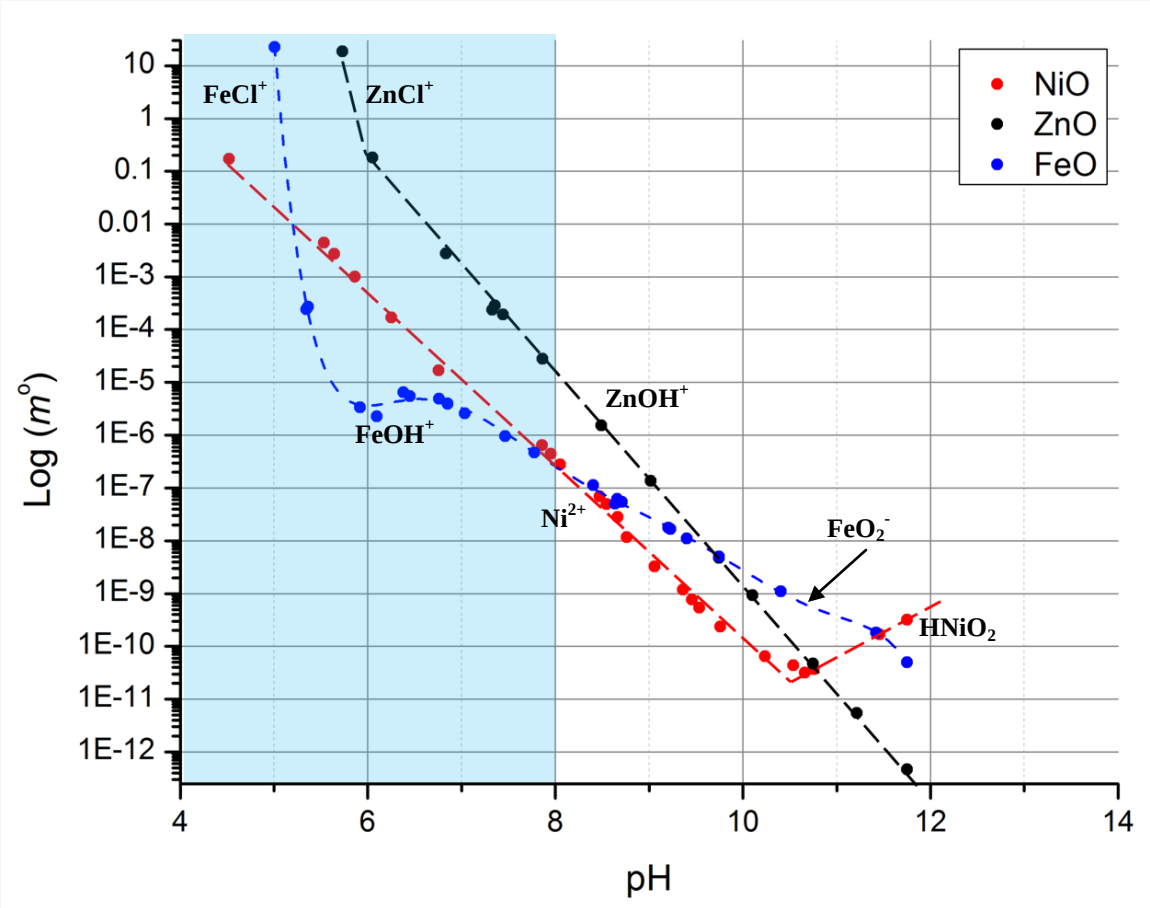

Fig. 19. Solubility data created in FactSage® for (a) NiO, (b) ZnO, and (c) FeO at room temperature. Shading marks the range of pH used in this study.

Since the spin-spray depositions are performed at 90°C the K_{sp} values were calculated using FactSage®. The nickel and zinc oxide slopes are comparative to that in literature. However, the iron oxide slope varies from the literature slightly, most likely due to the precursor, iron chloride, see Fig. 20 [32].

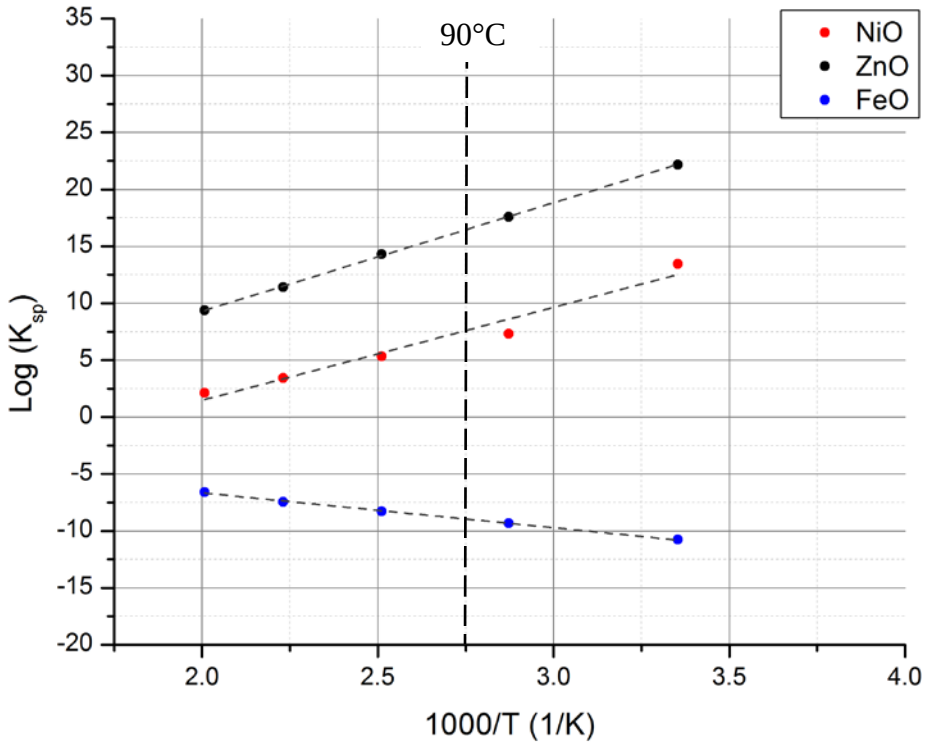

Fig. 20. The effect of temperature on the solubility of (a) NiO, (b) ZnO, and (c) FeO.

Sequential Reaction Theory.

There are two different modes of deposition, namely, by a continuous liquid layer, also known as the sequential reaction theory, and the microdroplet (µ-droplet) regime. The sequential reaction theory is used by Abe and Matsushita *et al*. shown in Fig. 22 to explain their results. It implies that the flow rate of reactants to is sufficiantly high enough that a continuous liquid film forms on the spinning platen. Reactants diffuse through the layer and deposit onto the ferrite at the solid surface. In Fig. 22 the spinning spray platen has an oxidant and reactant nozzle directly above the substrate in close

proximity. Ferrite layers grow via the squential exposure of the chloride and oxidant reactants. The liquid by products is then flung off due to continuous force.

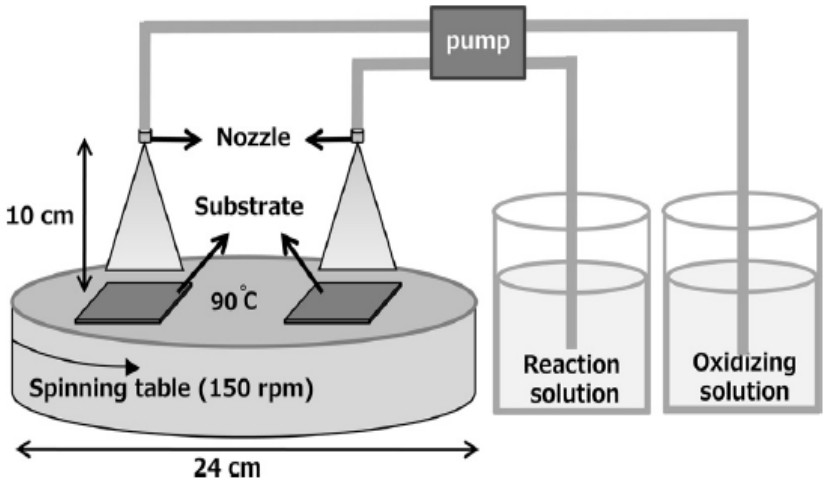

Fig. 22. Abe and Matsushita *et al*. ferrite plating set-up for the continuous layering method [33].

The surface of the substrate is terminated with OH^- groups after exposure to the oxidant, then iron (Fe^{2+}) and metal chlorides (M^{2+} = Ni^{2+}, Zn^{2+}, and Co^{2+}) are absorbed, while releasing the H^+ ions [34]. Exposure to the oxidizing agent again changes the surface species to OH groups. This process is cyclically repeated, thus building up the ferrite films layer-by-layer [34].

There are four basic processes that occur during the sequential reaction theory, shown in Fig. 23. First, a continuous layer of metal ions, such as M^{2+} and Fe^{2+}, coat the substrate surface which adsorb onto the surface [17]. It is assumed that the substrate

surface contains OH^- groups for the metals ions to adsorb onto. Second, the oxidant layer is sprayed onto the surface, in a continuous layer, and the Fe^{2+} ions are oxidized to Fe^{3+} ions. Next, the metal ions are adsorbed onto the surface, forming the spinel ferrite layers, and H^+ ions are dissociated and released [17]. Finally, this process is repeated to form multiple spinel ferrite layers. Using magnetite as an example, the oxidation-reduction reaction of this process is shown in Eqn. (3) [17],

$$3Fe^{2+} + 4H_2O \rightarrow Fe_3O_4 + 8H^+ + 2e^- \quad (3)$$

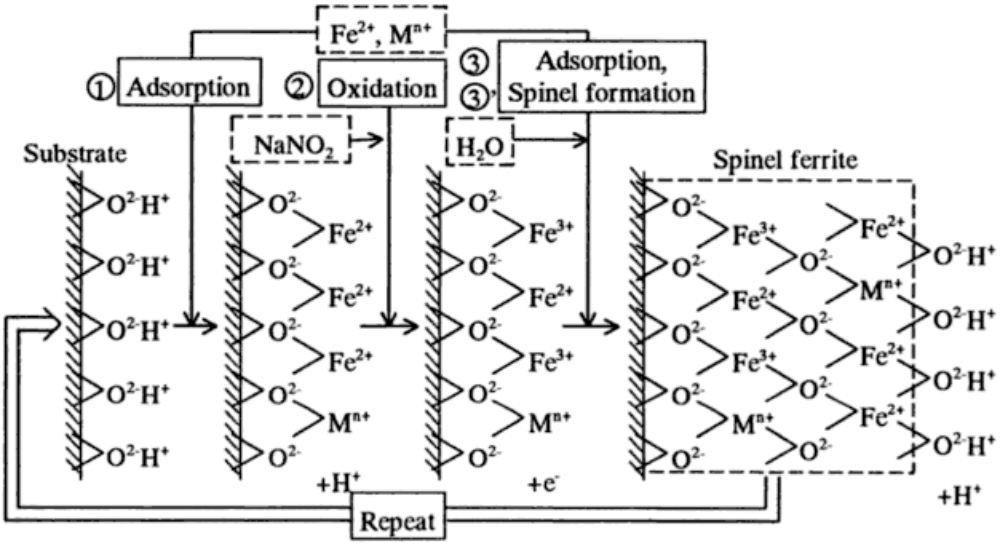

Fig. 23. Principle theory of ferrite plating method using $Fe^{2+} \rightarrow Fe^{3+}$ oxidation according to Abe and Matsushita [35].

µ-droplet Regime.

A second method is the µ-droplet theory. It is based on the same concept as the sequential reaction theory except instead of a continuous liquid layer, there are micron-sized droplets that form four jet streams of droplets. After performing multiple literature research, experiments and simulations, it has been concluded the µ-droplet regime uses lower flow rates than the continuous flow regime and obtains higher growth rates. This is caused by the oxidizers ability to get to the reaction surface faster, see schematic in Fig. 24.

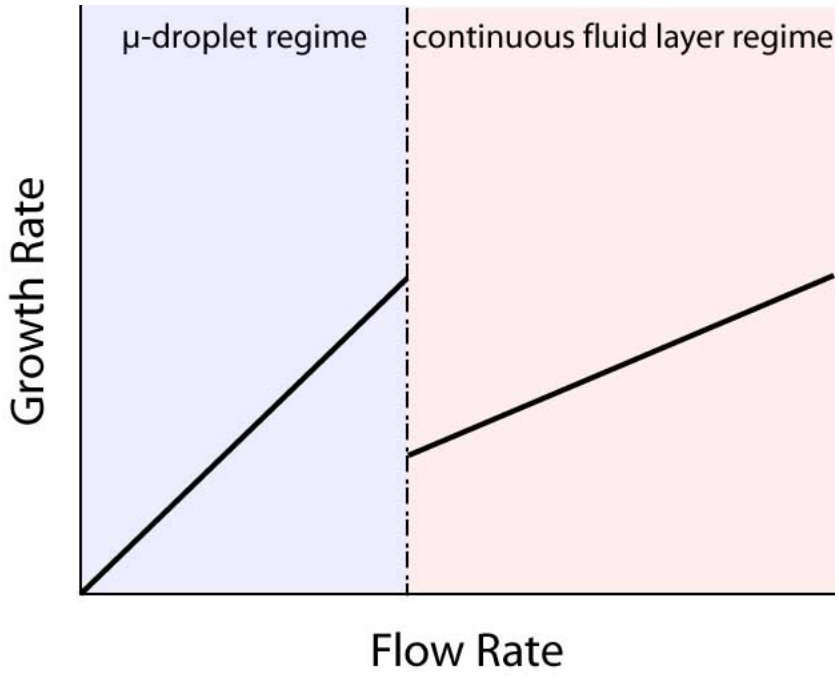

Fig. 24. Schematic illustration of growth rate effects between the continuous fluid layer regime and the µ-droplet regime [36].

In the μ-droplet theory the droplets reach the surface they react and spin off the platen, Fig. 25 shows a simulation of the jet stream of droplets. The droplets are on the order of 50 microns, as calculated using computational fluid dynamics (CFD) by Dr. Heath Lorzel [37]. CFD utilizes numerical methods and algorithms to solve and analyze problems that involve fluid flow, in this case the spin disc reactor (SDR). Figure 25 represents a simulation of the μ-droplet theory using the correct dimensions of the reactor. The first image represents atomized liquid when the nebulizers are turned on at 55 psi. Fig. 26 and 27 shows a schematic of the reaction between the precursor and oxidizer μ-droplets which form the spinel ferrite. When the reaction between the precursor and oxidant occur the ferrite deposits on the substrate and the excess spins off the platen and drains out into the waste.

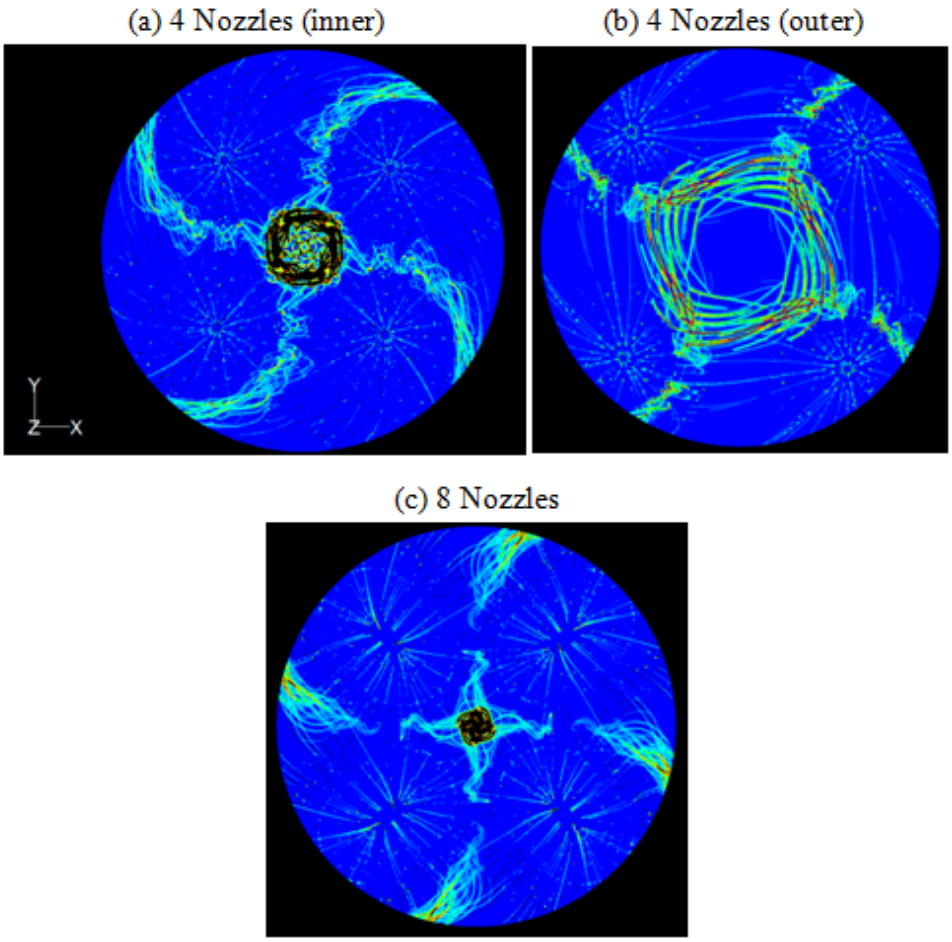

Fig. 25. Simulations of the jet stream using (a) 4- inner nozzles (b) 4- outer nozzles, and the best coverage of the platen using all (c) 8 nozzles [38].

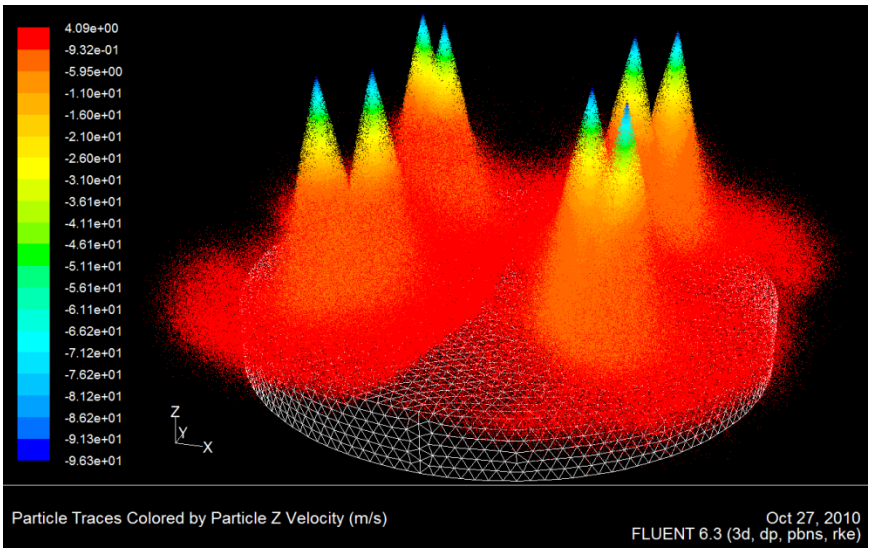

Fig. 26. Computational Fluid Dynamics (CFD) simulations from FLUENT of the µ-droplet regime with nebulizers turned on [37].

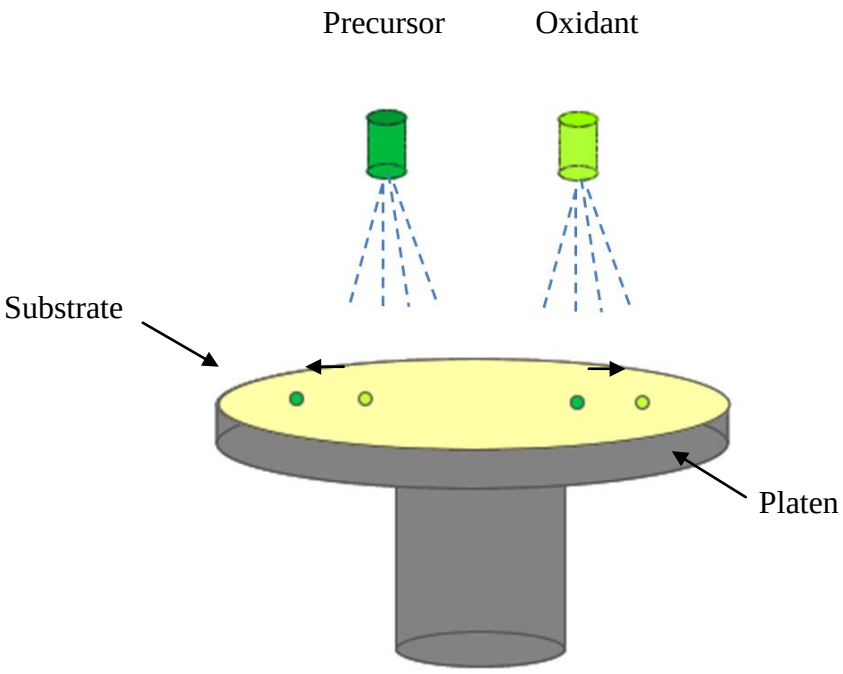

Fig. 27. Schematic of µ-droplet collision theory.

Aqueous Chemistry.

For both methods the aqueous solutions are referred to as the reactant (or precursor), containing metal chlorides, and the oxidant which supplies the oxygen atoms to the chemical reaction. The reactant contains iron chloride tetrahydrate ($FeCl_2 \cdot 4H_2O$), nickel chloride hexahydrate ($NiCl_2 \cdot 6H_2O$), and zinc chloride ($ZnCl_2$) for Ni-Zn spinel ferrites, with the addition of cobalt chloride tetrahydrate ($CoCl_2 \cdot 6H_2O$) for Ni-Zn-Co spinel ferrites. There are two oxidants used in these experiments, the first is a simple aqueous solution made up of glacial acetic acid (CH_3COOH), sodium nitrite ($NaNO_2$) and aqueous ammonia hydroxide (NH_4OH). The second is used to balance pH with ammonium carbonate [$(NH_4)_2CO_3$], sodium acetate (CH_3COONa), sodium nitrite ($NaNO_2$), and sodium hydroxide (NaOH). The pH ranges from 7.5 to 9.5 with the optimal pH above 7.5.

The pH is one of the most important parameters using this deposition method. It determines the type, microstructure, particle size, and concentration of the spinel ferrite. At higher pH's (pH > 9.0) the microstructure is not columnar, while if the pH is lower the structure is columnar, but more or less the spin-sprayed spinel morphology consists of nanocrystalline substructure. If the pH is higher than 9.0 than the morphology changes from uniform columnar network to a non-columnar morphology with micro-cracks and pores, see Fig. 28 below. The Snoek's product is highest around an oxidant pH of 8.0 (pH_{EFF} = 6.0) for the μ-droplet regime, and around a pH of 7.0 for the continuous liquid layer regime, shaded in blue.

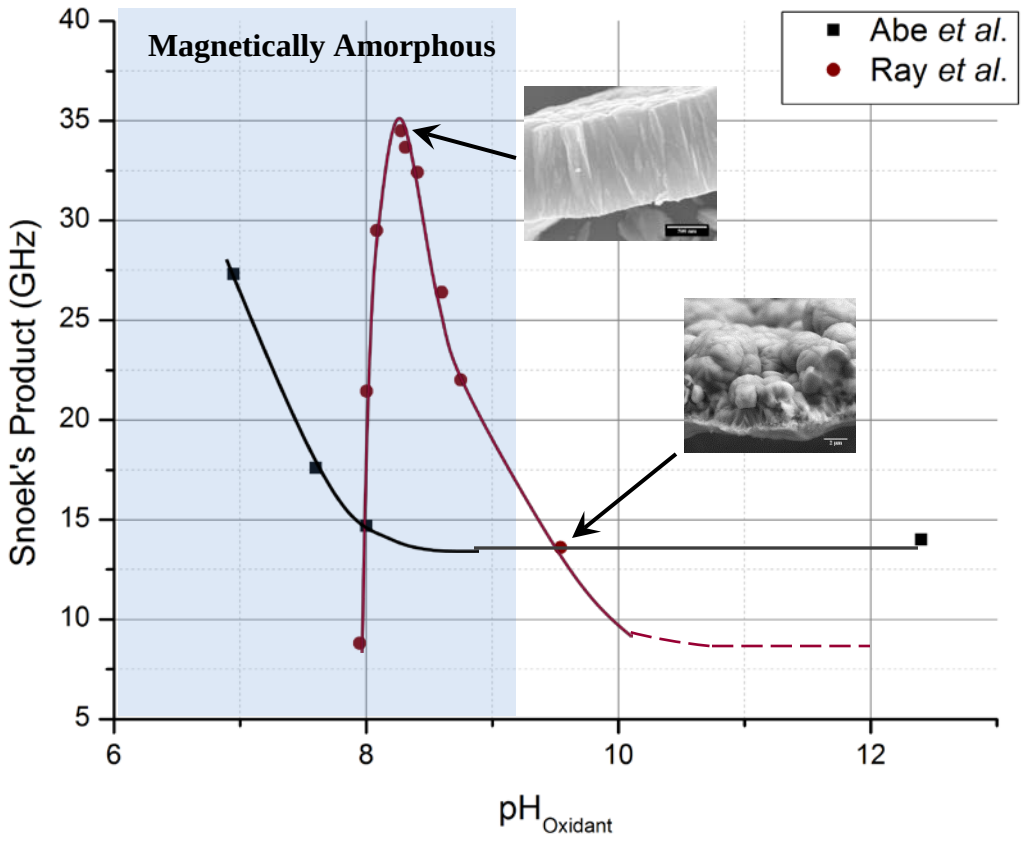

Fig. 28. The effect of oxidant pH on Snoek's product (GHz), taking only the isotropic data from Matsushita *et al*. [13], [34].

Sessile Droplet Experiment.

In order to obtain the best substrate for the spin-spray depositions, a sessile droplet experiment was produced. A nebulizer was attached to a Zeiss Optical microscope and placed at correct distance above the plane (about six inches). Various substrates were placed perpendicular to the ocular lens, as they would be placed on the platen. The substrates used in this experiment were glass, polyimide, polyether ether

ketone (PEEK), and a thin film Ni-Zn-Co ferrite. The images and contact angles of the micro-droplets are shown in Fig. 29.

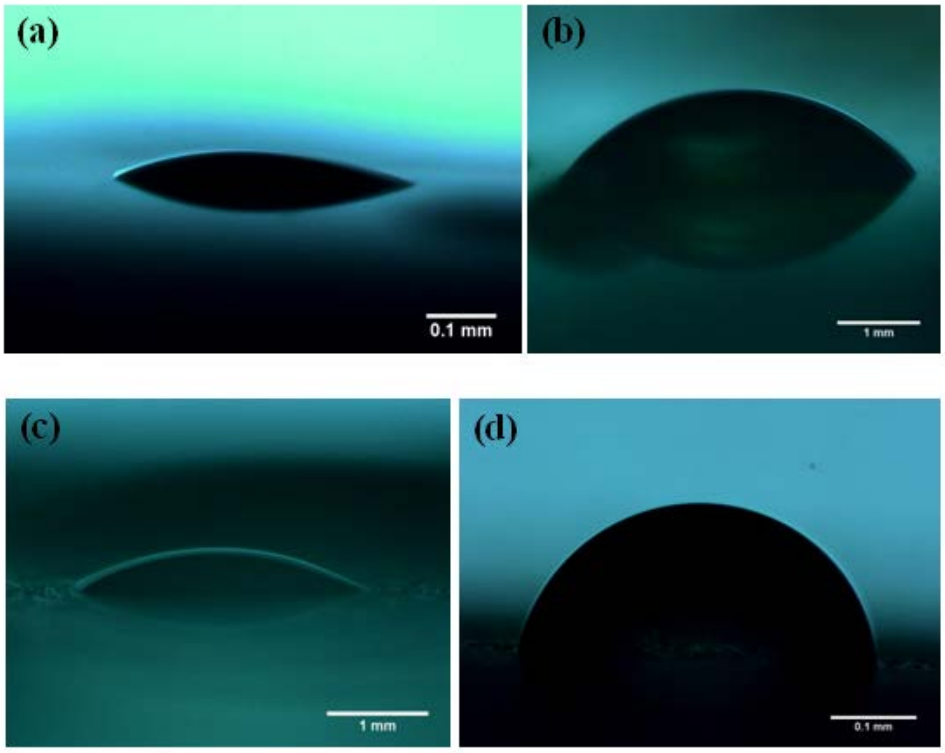

Fig. 29. Sessile droplets on (a) glass (θ = 164.8°) (b) polyimide (θ = 124.9°) (c) PEEK (θ = 160.1°) and (d) $Ni_{0.19}Zn_{0.30}Co_{0.05}Fe_{2.46}$ (θ = 95.6°)

According to the experiments, the glass and PEEK substrates had the best wetting angles, which was also proved in the actual depositions. Finding the contact angle of the substrates greatly improved the spin-spray deposition process. A more uniform, and less flakey material was formed after changing the substrate from polyimide to PEEK (or glass). After a full layer of ferrite deposits onto the substrate, the ferrite contact angle

dominates. As seen above in Fig. 29 when the droplets reach the spinel ferrite surface the wetting angle decreases and less of the precursor reacts.

ELECTRON MICROSCOPY

Scanning Electron Microscopy.

To analyze the grain sizes, morphology and microstructures electron microscopy was used, specifically a Hitachi S7800 Scanning Electron Microscope (SEM).

In a typical cold field emission electron gun SEM (FEG) the electron beam emits electrons from an electric field, which emits electrons from an electron gun. A FEG-SEM usually has a tungsten filament cathode, the SEM is illustrated in Fig. 30. The electron beam, ranging from 0.2 keV – 40 keV, is focused by one to two condenser lenses and passes through a pair of scanning coils in the electron column to deflect the beam in the x and y axes in order to scan in raster mode. When the primary beam interacts with the specimen, the electron immediately loses energy by randomly scattering and absorbing within the interaction volume, extendeing from 100 nm to 5 microns depending on the specimen density and atomic number. The energy exchange between the specimen and electron beam results in elastic scattering and emission of electromagnetic radiation and secondary electrons by inelastic scattering, both in which can be detected.

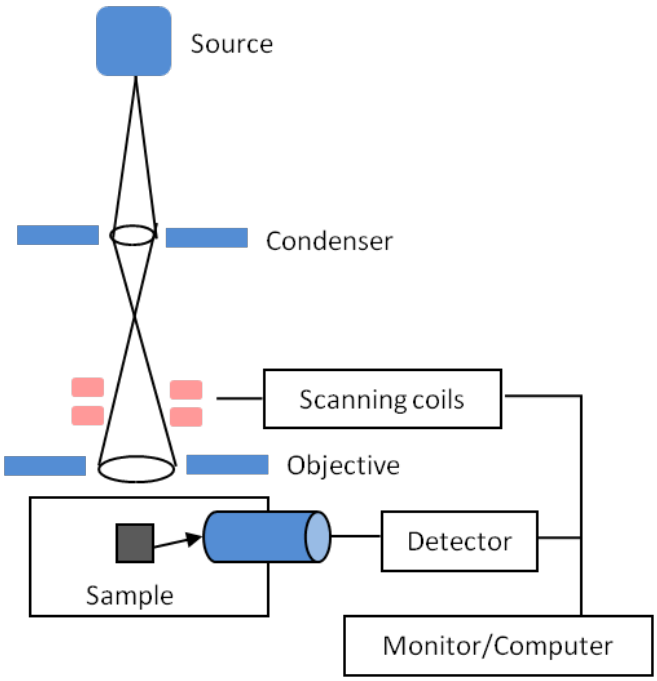

Fig. 30. SEM path diagram.

SEM measures the thicknesses and images the microstructure and morphology of each ferrite deposition. The Hitachi S7800 measures the sample surface using a high energy beam of electrons. This particular instrument uses a cold field emission electron gun (FEG), and contains a five axis motorized specimen stage. The resolution of the SEM is 5 nm, with an equipped Energy-dispersive X-ray Spectroscopy (EDS) detector for basic elemental detection. Since EDS is not sensitive enough to analyze the concentration of cobalt in the Ni-Zn-Co ferrite system, Particle Induced X-ray Emission (PIXE) is used, which is 100 times more sensitive than EDS.

Transmission Electron Microscopy.

Transmission electron microscopy (TEM) analysis was performed using a Phillips CM200 microscope by Desai Zhang and Lin Zhou. The instrument used is very versatile which has an acceleration voltage of up to 200 kV, a point resolution of 0.19 nm, and a 0.14 nm line resolution. This particular instrument uses a Schottky Field Emission source, which is made by coating a tungsten tip in zirconium oxide. The computer controlled eucentric goniometer can tilt ±45º along the A-axis and ±30º along the B-axis, making it ideal for diffraction research. Furthermore, it can also be used for imaging magnetic materials at nanometer resolutions, and electron holography of electric and magnetic fields.

Given a sufficient amount of current the source begins to emit electrons thermionically into a vacuum, shown in the schematic in Fig. 31. Once extracted the upper lens permitting for the formation of the electron probe to size and location for later interaction with the sample. Two physical effects manipulate the electron beam. The first is the interaction of electrons with a magnetic field, allowing electromagnetic to manipulate the electron beam. The second is and electrostatic field, which can deflect the electrons at a constant angle. The coupling of these two deflections is extremely important in TEM especially STEM for beam shifting, it is essential for control over the beam path. Optical configuration can also be rapidly changed by enabling and disabling lenses, which allow for beam convergence. [39]

The sample preparation for TEM begins with cutting the sample and gluing it onto a silicon wafer. Next the sample is polished on a polishing wheel, and then dimpled. Finally the sample is ion milled until it is electron transparent and can be imaged on the TEM.

See Chapter 3 for a more in depth analysis of TEM and Holography imaging.

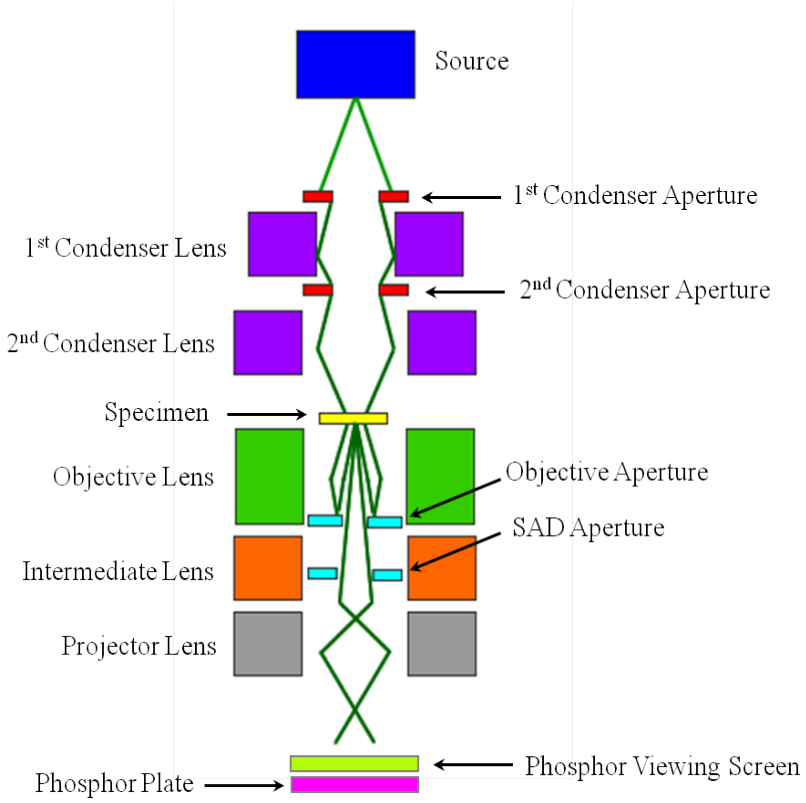

Fig. 31. TEM electron path diagram.

X-RAY DIFFRACTION

X-ray Diffraction (XRD) was performed on the D5000 diffractometer. Powder diffraction uses x-rays on powder, micro- or nanocrystalline samples for structural characterization on materials. Ideally, each crystalline sample will be equally oriented. The orientation average causes the three dimensional reciprocal space to be projected into a single dimension. To eliminate texturing effects and achieve true randomness, it may be necessary to rotate the sample.

When the scattered radiation is collected, the rotational averaging leads to smooth diffraction rings around the beam axis [40]. The angle between the beam axis and the ring is called the scattering angle (denoted as 2θ). According to Bragg's law, Eqn. 7, each ring corresponds to a particular reciprocal lattice [40].

$$n\lambda = 2d \sin\theta \tag{7}$$

Though, Laue was credited with discovering diffraction, Bragg constructed the equation which predicted when diffraction took place, it is a widely known equation in crystallography [40]. Where λ, is the wavelength of radiation, 1.54Å for copper, d is the inter-planar spacing and θ is the angle between the incident ray and relevant crystal plane. Fig. 32, schematically represents an x-ray diffracting from part of a single crystal.

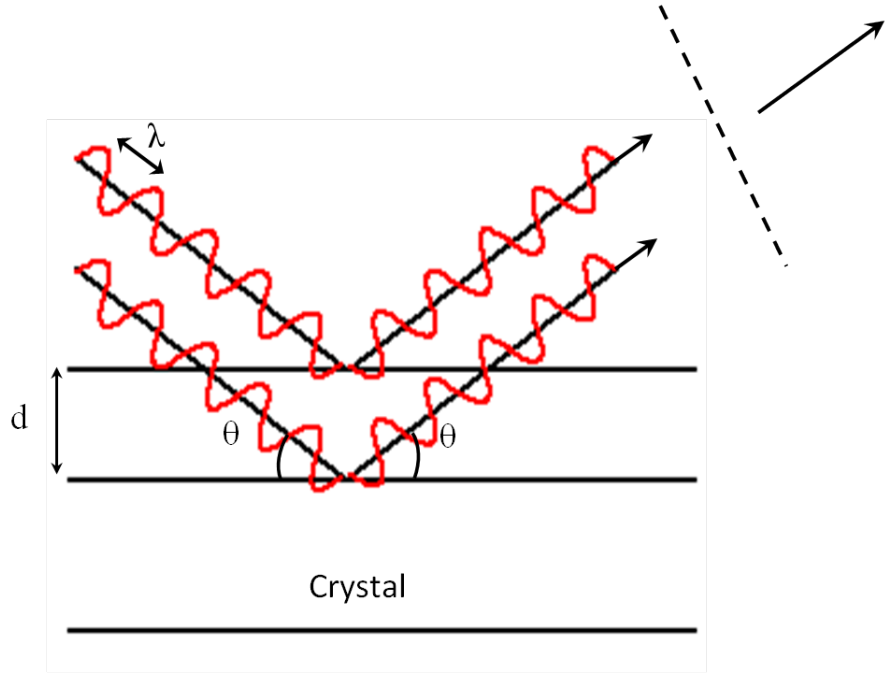

Fig. 32. Schematic of Bragg's Law.

PARTICLE INDUCED X-RAY EMISSION

Particle induced x-ray emission (PIXE) is a non-destructive elemental analysis technique for measuring material composition. Helium ions bombard the inner shell of electrons, 1-3 MeV energy, and the outer shell electrons relax and emit characteristic x-rays, seen in Fig. 33. The spectrum is deconvoluted with a software program called Gupix. The analysis output can be seen in Fig. 34, for where typical compositions for spinel ferrite thin films in this study are $Ni_xZn_y\ Co_{0.05}Fe_{2.95-x-y}O_4$, where x = 0.1-0.5 and y = 0.2-0.3.

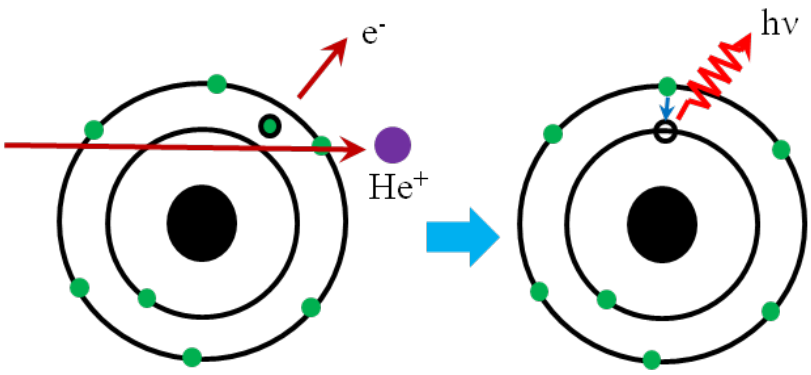

Fig. 33. Representation of particle induced x-ray emission (PIXE)

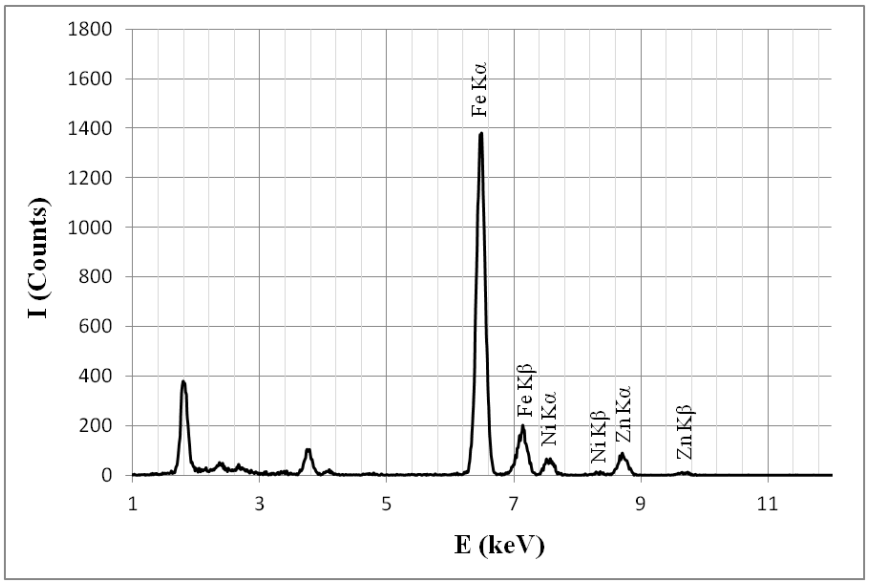

Fig. 34. Typical PIXE spectrum for $Ni_{0.19}Zn_{0.39}Co_{0.05}Fe_{2.38}O_4$.

MAGNETIC PROPERTIES

AC Magnetic Properties.

For ferrimagnetic spinels and hexagonal ferrimagnetic oxides having the preferred direction of magnetization on the z-axis, where $H_{\varphi}^{A} = H_{\theta}^{A} = H^{A}$ [4]. The rotational permeability is then isotropic, and reduces to Eqn. (8) [4].

$$\frac{(\mu_0 - 1)}{4\pi} = \left(\frac{2}{3}\right)\frac{M_S}{H^A} \tag{8}$$

Where H^A is the field, M_s is the magnetization saturation, and μ_0 is the initial permeability. The initial permeability can be calculated for rotations according to Eqn. (8) using the crystal anisotropy and magnetic saturation data [4]. Some of the more obvious properties that effect this measurement are size and distribution of pores as well as average crystallite size [4]. Smit and Wijn have shown with $Ni_{0.5}Zn_{0.5}Fe_2O_4$ there is an substantial increase in permeability with an increase in density of material, which was done through sintering, see Fig. 35 [4].

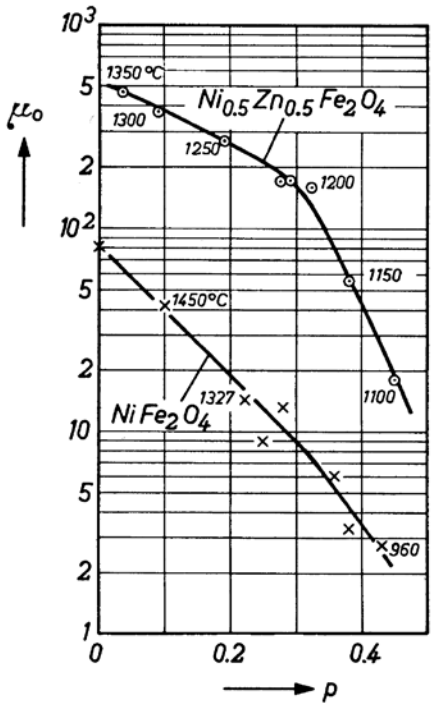

Fig. 35. The effect of porosity on initial permeability for $Ni_{0.5}Zn_{0.5}Fe_2O_4$ and $Ni\,Fe_2O_4$ spinel ferrites.

The AC permeability is measured by Dr. Sergio Clavijo and Tom Sebastian using a Microstrip permeameter. Assessing the permeability of the ferrite accurately is essential to finding to the quality of the material. The permeameter used by our group has been designed and modified to fit the spin-spray deposited film. The idea behind the Microstrip permeameter is to place a layer of the permeable material against the shortened end of the strip, which is shown in Fig. 36.

Fig. 36. Microstrip Permeameter designed to fit thin film ferrite samples.

The geometry of field structure in the microstrip permeameter is shown below in Fig. 37. There are many advantages of choosing the microstrip transmission line, which are as follows:

(1) The electric field has minimal interaction with the ferrite sample and the magnetic field is approximately constant due to the geometry.

(2) There is no electromagnetic limit for the low frequency measurement.

(3) The high frequency measurement is only limited by the onset of radiation from design.

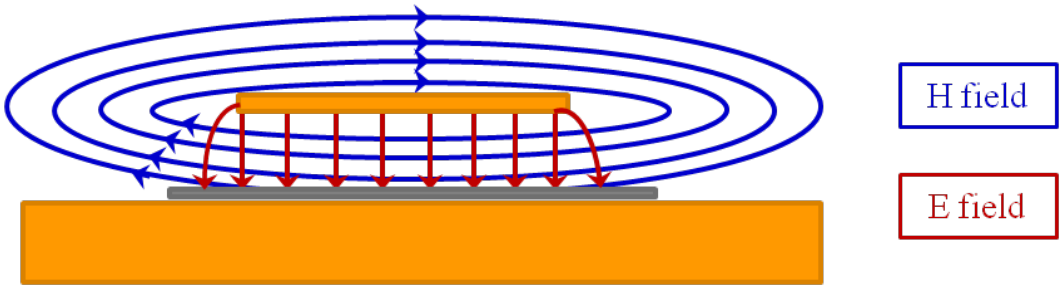

Fig. 37. Geometry of the field structure in microstrip permeameter.

The largest problem with any permeability measurement device is its sensitivity to film thickness. Typically the films are around 1 μm thick and the spacing between the microstrip and ground is 1 mm, so the anticipated μ_{eff} is in the 1.0X range. Assuming the length of the microstrip is electrically small, t_1, and the permittivity has been separately determined, where the input impedance immediately yields the effective permeability of the region where the material under test Z_{in}, in Eqn. (9) and Eqn. (10) [41].

$$Z_{in} = \sqrt{\frac{\mu_{eff}}{\varepsilon_r}}\eta_0 \tan\left(\sqrt{\mu_{eff}\varepsilon_r}k_0 t_1\right) \tag{9}$$

Where k_0 is the free space wave number, and η_0 is the characteristic impedance of the transmission line [41].

$$Z_{in} \xrightarrow{t_1\ small} j\omega\mu_0\mu_{eff}t_1 = j\omega L_P \tag{10}$$

Where L_p is the permeance (μ*t, units Henry) of the region, $L_P = \mu_0\mu_{eff}t_1$.

The next step is to extract the permeability relating μ_{eff} and μ_{film} using the morphology function [42]. In this specific permeameter the morphology function has been derived from a four pole sum of Debye functions, seen in Eqn. (11) [41]. The morphology function links the sample geometry to the permeability in the actual test [41].

$$\mu_{eff} = 1 + \frac{\alpha_0}{1+\frac{jv}{\beta_0}} + \frac{\alpha_1}{1+\frac{jv}{\beta_1}} + \frac{\alpha_2}{1+\frac{jv}{\beta_2}} - \frac{j\alpha_3}{v} \quad (11)$$

Where α and β are constants, and *v* is used to determine μ_{film}.

Eqn. (11) can now be inverted to a fourth order polynomial which can determine *v*, shown in Eqn. (12) [41]. The permeability can now be extracted from this equation.

$$v = \frac{j}{\mu_{film}-1} = \frac{j}{\chi_{film}} \quad (12)$$

DC Magnetic Properties.

Large magnetic permeabilities and low losses are important features in determining the usefulness of spinel ferrite thin films. Magnetostatic and low frequency behaviors are characterized by a magnetometer (MPMS® SQUID VSM, Quantum Design, San Diego, CA), which uses a direct current to measure the magnetic hysteresis loop for any given material. The magnetometer used in these experiments is a vibrating sample magnetometer with a superconducting quantum interface device. The initial permeability, saturation magnetization, remanent magnetization, and coercive field can all be obtained from the hysteresis loops. An example of thin film magnetite (Fe_3O_4, purple curve) and thin film Ni-Zn ferrite ($Ni_xZn_yFe_{3-x-y}O_4$, red curve) is shown in Fig. 38.

For the $Ni_xZn_yFe_{3-x-y}O_4$ curve, a comparably large permeability, remanent magnetization (129 emu/cc), and saturation magnetization (187 emu/cc), with a small coercive field (28 Oe) and energy loss per cycle is seen.

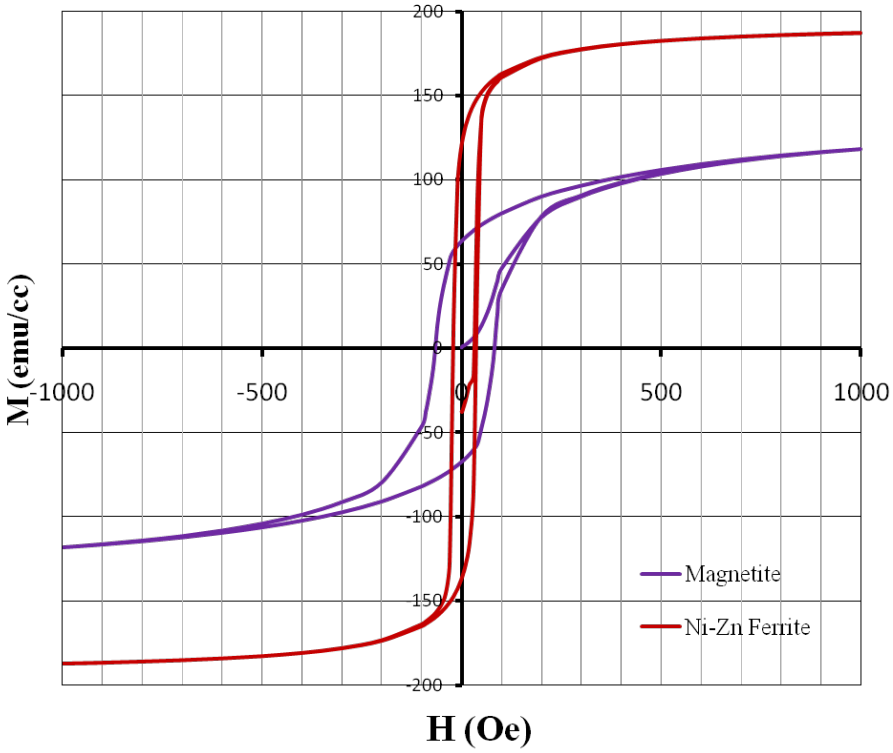

Fig. 38. Hysteresis loops for magnetite (purple) and Ni-Zn ferrite (red) at 300K.

When the field is increased indefinitely until reaching saturation, designated M_s, the magnetic dipoles within the material are aligned in the direction of the magnetic field, H (Oe) [5]. The saturation magnetization is only dependent on only the magnetic moments, ***m***, and number of atoms per unit volume, *n* [5].

$$M_s = n\boldsymbol{m} \tag{13}$$

From Eqn. (13) it is noted the magnetization saturation is only dependent on the materials present in the sample, and hence not structure sensitive [5].

When the applied field is reduced to zero after magnetizing the magnetic sample the remaining magnetic induction is called the remanent induction, B_R, and the remaining magnetization is called the remanent magnetization, M_R, Eqn. (14) [5]. The remanent magnetization is an independent parameter and is most important in permanent magnet applications, since permanent magnets are used in an open circuit configuration [5].

$$B_R = \mu_0 M_R \tag{14}$$

Chapter 3

SYSTEMATICS OF SPIN-SPRAY DEPOSITION

The purpose of this chapter is to report on best experimental designs and the parametric trends observed. Multiple trends were found that assist in explaining the magnetic and electrical properties of the Ni-Zn-Co ferrite thin films deposited.

For bulk spinel ferrites prepared by traditional ceramic processing methods, the raw materials are typically prepared by weighing and blending the constituent oxides as powders, calcining from 900 – 1100°C and then ball milling the calcined material afterward. In order to control the particle packing in conventional ferrites, slurry is made with a binder and then sprayed into pressable powders for use in a die press. The final step is sintering at high temperatures, in order to burn of the binder and residuals [6]. One of the largest considerations for industry is the cost, quality, and reproducibility of the product [6]. During conventional processing, iron oxide is one of the largest cost concerns, especially if it is needed in the purest form. There are four main sources; natural iron ore, hydrochloric acid regeneration, decomposition from copperas, and the most expensive oxidation of carbonyl iron [6].

Since conventional ferrites have been extensively researched, and scaled up to the industrial level, non-conventional ferrite techniques have recently been a focus point. In this chapter the spin-spray process is analyzed specifically for data trends. The data trend analysis will eventually assist in the expansion of the reactor to an industrial scale.

CRYSTALLITE SIZE ANALYSIS

X-Ray Diffraction (XRD) in this research is mainly used for phase identification and grain size analysis. Both powders and thin films were use on the D5000 for analysis. Grain are not always orientated randomly, in the case of textured films the x-ray intensifies a preferred film plane, (*hhh*). After rigorous analysis of $Ni_{0.24}Fe_{2.76}O_4$, $ZnFe_2O_4$, and $(Ni, Zn)_xFe_{3-x}O_4$, the thin film spinel ferrite deposited using spin-spray deposition methods was found to have preferred orientation around the high density packed basal plane, *i.e.* (*hhh*), and the (*0hh*) plane. In the case of $Zn_{0.57}Fe_{2.43}O_4$, in Fig. 39, the preferred orientation is in the (222) direction. Figure 40 shows the preferred orientation of $Ni_{0.24}Fe_{2.76}O_4$ in the (022) direction. For Ni-Zn-Co spinel ferrites, Fig. 41 shows the slight preferred orientation of a typical $Ni_{0.18}Zn_{0.23}Co_{0.05}Fe_{2.54}O_4$ film about the (022) direction.

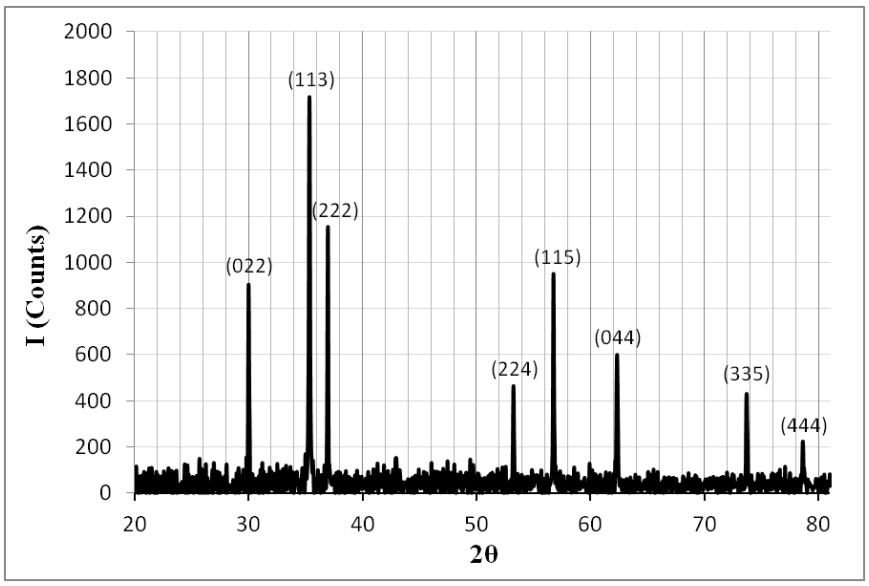

Fig. 39. $Zn_{0.57}Fe_{2.43}O_4$ diffraction pattern showing preferential orientation about the basal plane.

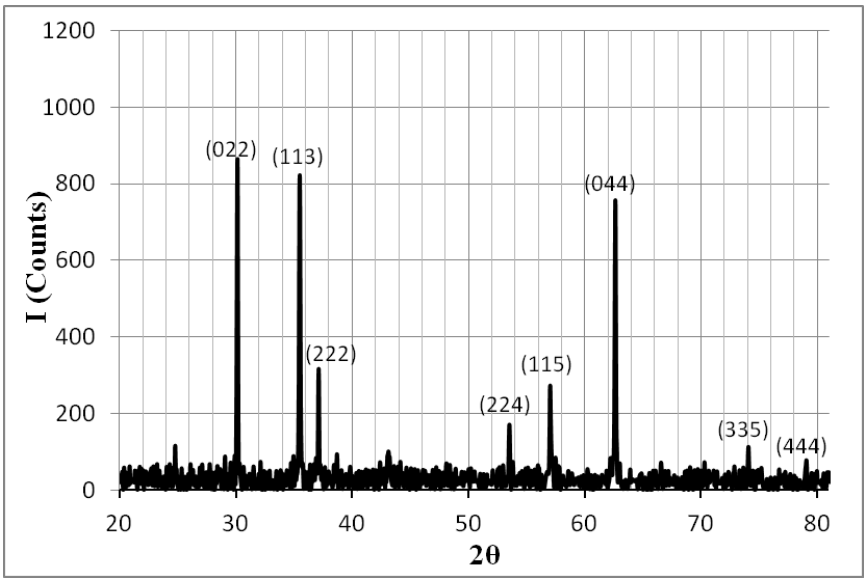

Fig. 40. $Ni_{0.24}Fe_{2.76}O_4$ diffraction pattern showing preferential orientation about the basal plane.

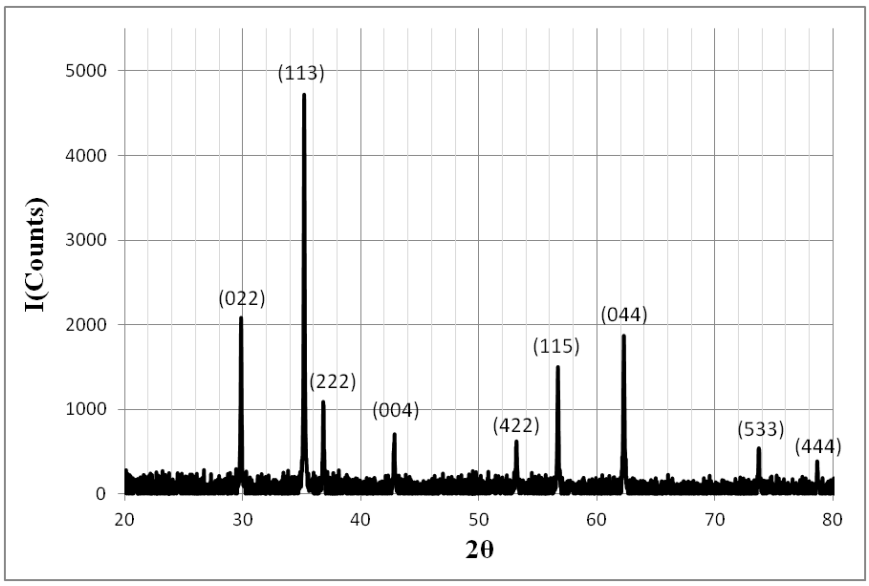

Fig. 41. $Ni_{0.18}Zn_{0.23}Co_{0.05}Fe_{2.54}O_4$ diffraction pattern showing preferential orientation about the basal plane.

The grain sizes for Ni-Zn-Co and Mn-Zn ferrite films were analyzed using the same D5000 diffractometer. The diffraction patterns from the D5000 were analyzed for the crystallite size using MDI Jade Software and the Scherrer equation was used to confirm the results, see Eqn. (15) below.

$$t = \frac{0.9(\lambda)}{Bcos(\theta)} \tag{15}$$

where B is the line broadening at half the maximum intensity in radians, θ is the Bragg angle, λ is the wavelength of the radiation peak to peak, for copper 1.5406 nm, and t is the thickness of grains in units of nanometers (nm).

When the diffraction patterns were analyzed the background was subtracted and striped of the Kα2 peak using MDI Jade 9.0 software. Next the data was configured to a

text file and uploaded into Microsoft Excel and where the Scherrer equation was applied. The values calculated ranged from 55.27 nm ± 11.28 nm. The diffraction pattern along with the sample's grain size was calculated using Eqn. (15) are shown below in Figs. 42 - 43 for two different samples.

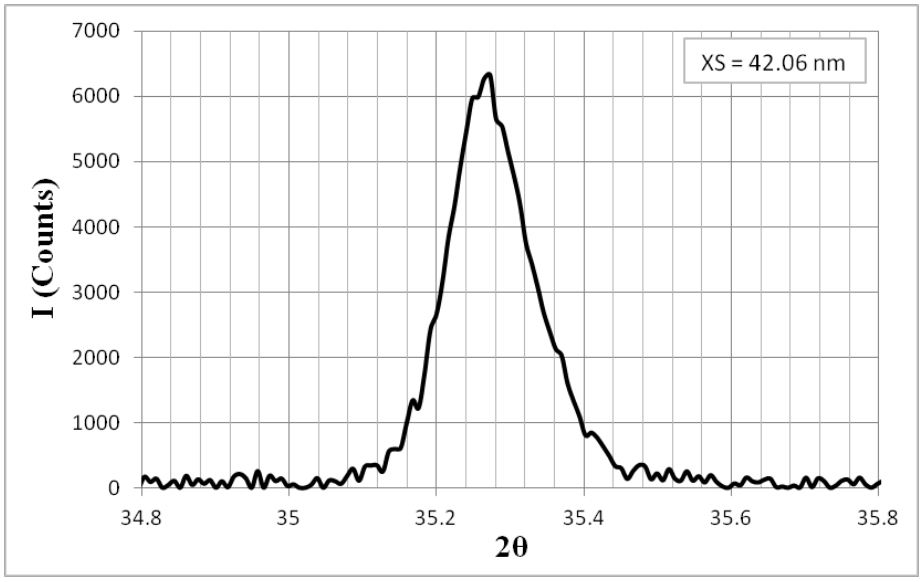

Fig. 42. $Mn_{0.03}Zn_{0.68}Fe_{2.29}O_4$ unannealed with crystallite size (ie. XS) of 42.06 nm calculated from fit centered at 35.26º 2θ.

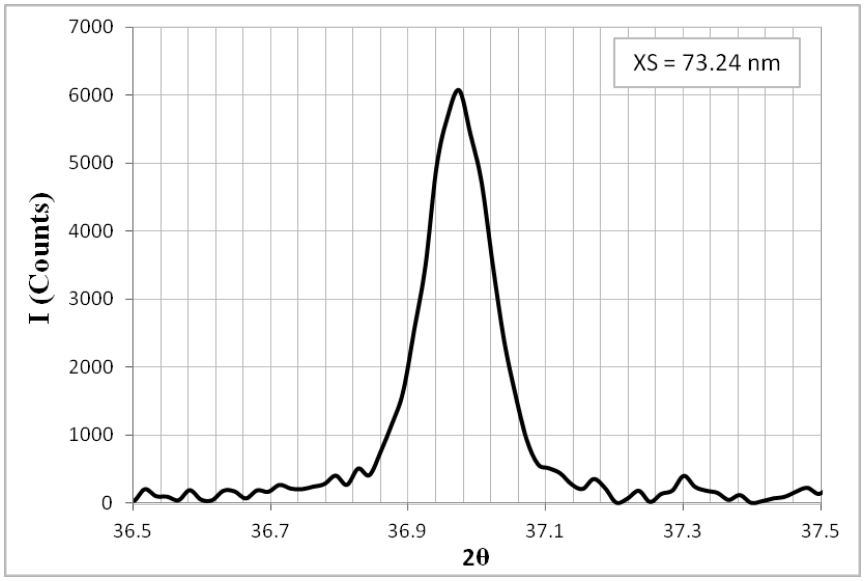

Fig. 43. $Mn_{0.01}Zn_{0.35}Fe_{2.64}O_4$ unannealed with crystallite size of 73.24 nm calculated from fit at 36.97º 2θ.

Scherrer calculations estimate the average grain size assuming a random grain orientation across the sample. It also does not account for the integral breadth, the skewness, or background of the peak [43]. However, as seen in Fig. 39-41 there is a slight preferential orientation in these thin film samples. The Jade software program fits a peak profile using a shape functions such as the Pearson VII or Pseudo-Voigt function. Table I shows the crystallite size calculated for unannealed $Mn_{0.01}Zn_{0.35}Fe_{2.64}O_4$ using the Scherrer equation and the Pearson VII function which is used to control the skewness. The Pearson VII was popular during the 1980s-1990s for describing the peak shape from conventional powder diffraction pattern [43]. The Pearson VII function is basically a Lorentzian function raised to the m power, seen in Eqn. (16) [43].

$$I(2\theta) = I_{max} \frac{w^{2m}}{\left[w^2+(2^{1/m}-1)(2\theta-2\theta_0)^2\right]^m} \quad (16)$$

Where *m* represents the peak shape, I_{max} is the peak intensity, $2\theta_0$ is the 2θ position of the peak maximum, and *w* is the peak width. When $m \rightarrow 1$ the function becomes a Lorentzian function, and approaches a Guassian function when $m \rightarrow \infty$, or when $m > 10$ [43].

Table I. Unannealed $Mn_{0.01}Zn_{0.35}Fe_{2.64}O_4$ crystallite size calculated using MDI Jade 9 and the Pearson VII equation [43].

Pearson VII Equation for $Mn_{0.01}Zn_{0.35}Fe_{2.64}O_4$					
2θ	**d (Å)**	**Height**	**Area**	**FWHM**	**XS (nm)**
35.597	2.52	172	5975	0.531	*17*
37.237	2.4127	479	16130	0.476	*19*
39.46	2.2817	177	2320	0.192	*67*
40.993	2.1999	104	2843	0.403	*24*

Table II shows very similar crystallite sizes using the Pseudo-Voigt equation which uses a line profile resulting from the convolution of two broadening mechanisms. The major difference is the Pearson VII function allows for a continuous variation of the shape parameter from pure Lorentzian to pure Gaussian [43]. The Pseudo-Vogt function applies a variable proportion of pure Lorentzian to pure Gaussian by parameter η, seen in Eqn. (17) [43].

$$I(2\theta) = I_{hkl}[\eta \boldsymbol{L}(2\theta - 2\theta_0) + (1-\eta)\boldsymbol{G}(2\theta - 2\theta_0)] \quad (17)$$

Where I_{hkl} is the intensity of the peak, $\boldsymbol{L}(2\theta - 2\theta_0)$ and $\boldsymbol{G}(2\theta - 2\theta_0)$ are normalized Lorentzian and Gaussian functions respectively, and η is the Lorentzian fraction [43].

The combination function can be tailored to a specific peak shape, when η parameter varies from 0 being pure Lorentzian to 1, pure Gaussian [43].

Table II. Unannealed $Mn_{0.01}Zn_{0.35}Fe_{2.64}O_4$ crystallite size calculated using MDI Jade 9 and the Psuedo-Voigt function [43].

Pseudo-Voigt Equation for $Mn_{0.01}Zn_{0.35}Fe_{2.64}O_4$					
2θ	**d (Å)**	**Height**	**Area**	**FWHM**	**XS (nm)**
29.886	3.575	152	2972	0.237	*46*
29.031	3.0733	601	15807	0.386	*24*
30.401	2.9379	159	3710	0.359	*27*
35.751	2.5095	546	16997	0.444	*21*

SYSTEMATICS OF REACTOR

Deposition Trends.

After collecting the electrical and magnetic data from several different experiments using the spin-spray deposition method, results were analyzed to uncover systematic data trends. The first step in this analysis is to list the input and output parameters of the spin spray process, shown in Table III. The input parameters for each of the experiments were held constant except time and pH_{EFF}. The output parameters then are analyzed against the input parameters and eachother to find trends in the data.

Table III. The input parameters for the spin spray process and measured output parameters.

Input Parameters	**Output Parameters**
Reactants	Thickness
Oxidants	Grain Size
pH	R_{Dep}
RPM	Quality
T_{Set}	μ'
Nebulizer Flow Rate	Frequency
Nebulizer Configuration	Snoek's Product
$V_{Solutions}$	M_S
N_2 Pressure	M_R
Time	H_C
Substrate	Cation Fractions

There is a distinct trend in the data of an increase in iron in the film with decreasing nickel and zinc as the deposition rate increases. This suggests that iron deposits and reacts more rapidly than nickel and zinc. Fig. 44-46 shows the deposition rates (nm/min) against the cation fraction in the film of each constituent. In Matsushita *et al*. it is reported to increase the deposition rate and still maintain the desired properties the oxidant is replaced with potassium acetate ($KOCOCH_3$) and potassium hydroxide (KOH), instead of using ammonium acetate (NH_4COCH_3), and ammonia (NH_4OH) [13]. Due to the buffer change in these experiments the composition of the films changed, and hence the magnetic properties [13]. The Snoek's product in these samples still exceeds the bulk, which makes $KOCOCH_3$ a viable solution for increasing the deposition rate, shown in Fig. 47.

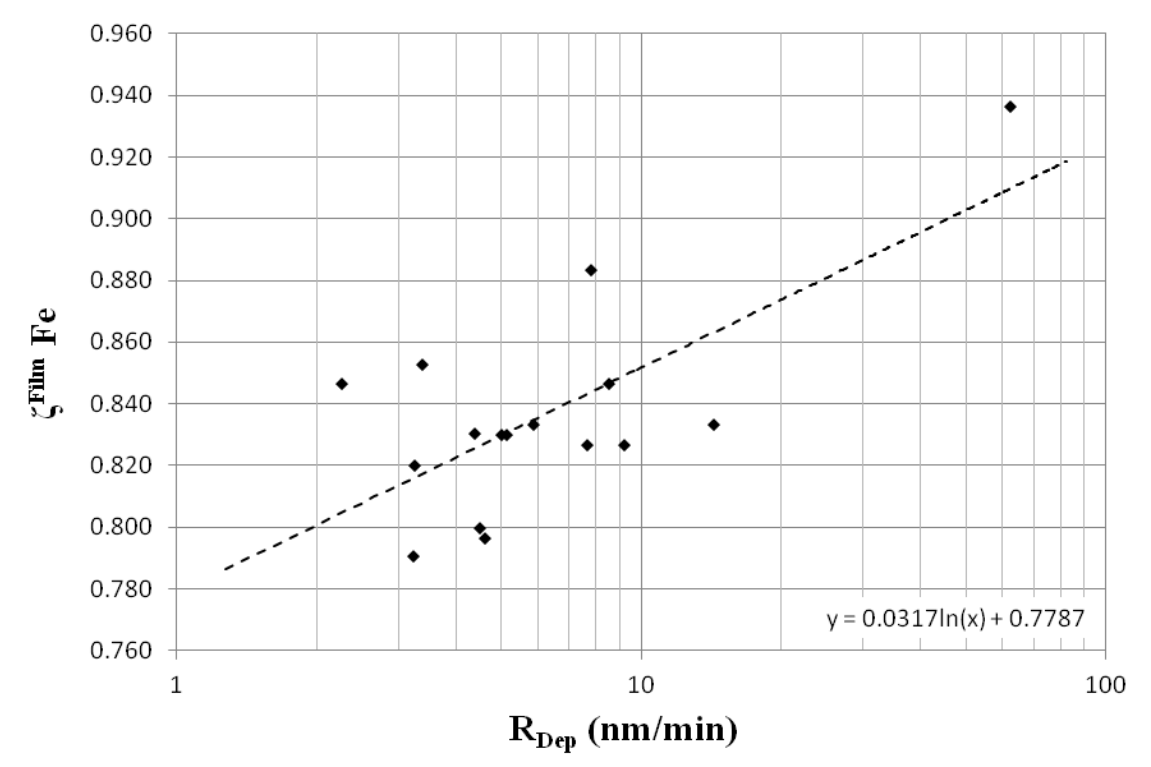

Fig. 44. An increase in deposition rate generally yields a higher cation fraction of iron in the film.

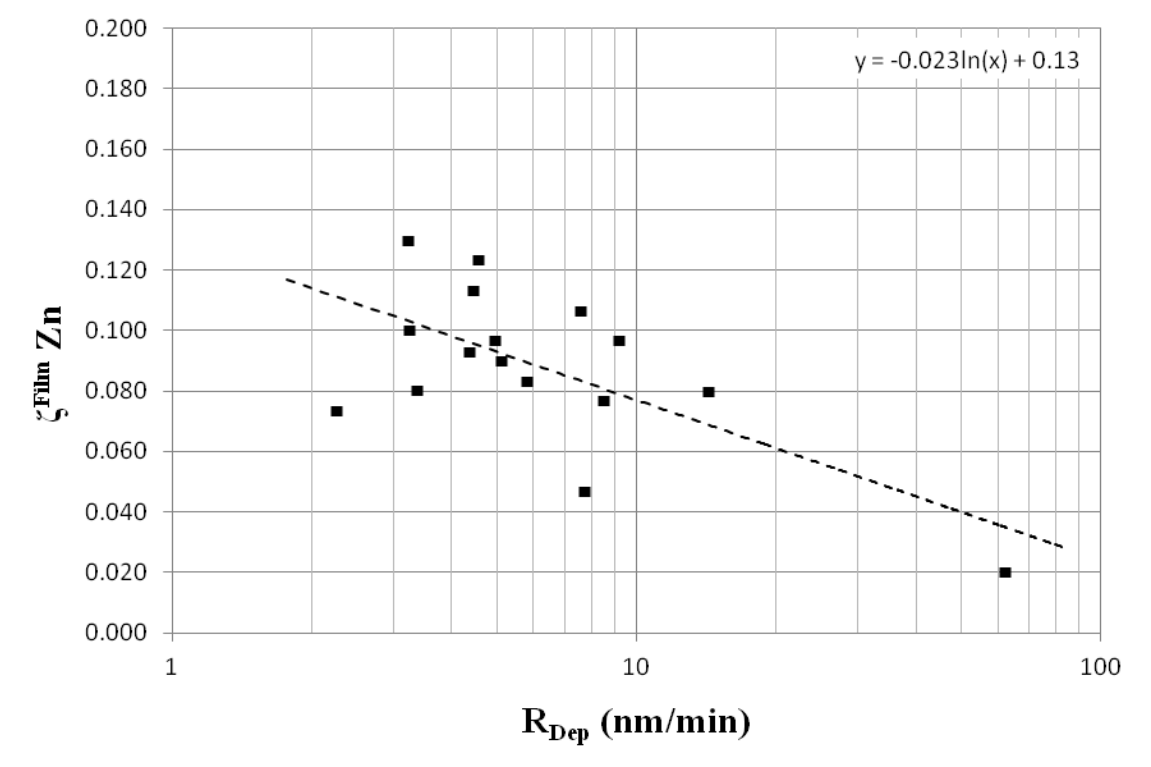

Fig. 45. An increase in deposition rate yields a decrease in cation fraction of zinc in the film.

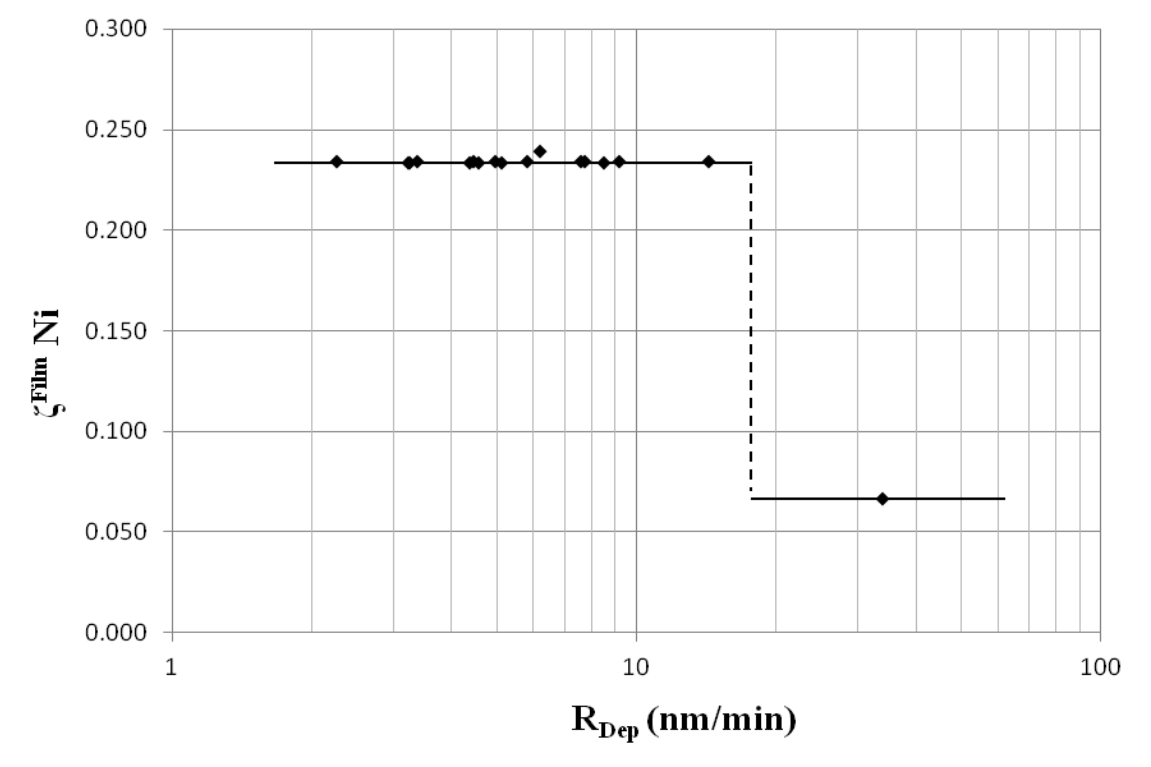

Fig. 46. An increase in deposition rate yields a step change decrease in cation fraction of nickel in the film after a deposition rate of 14.0 nm/min.

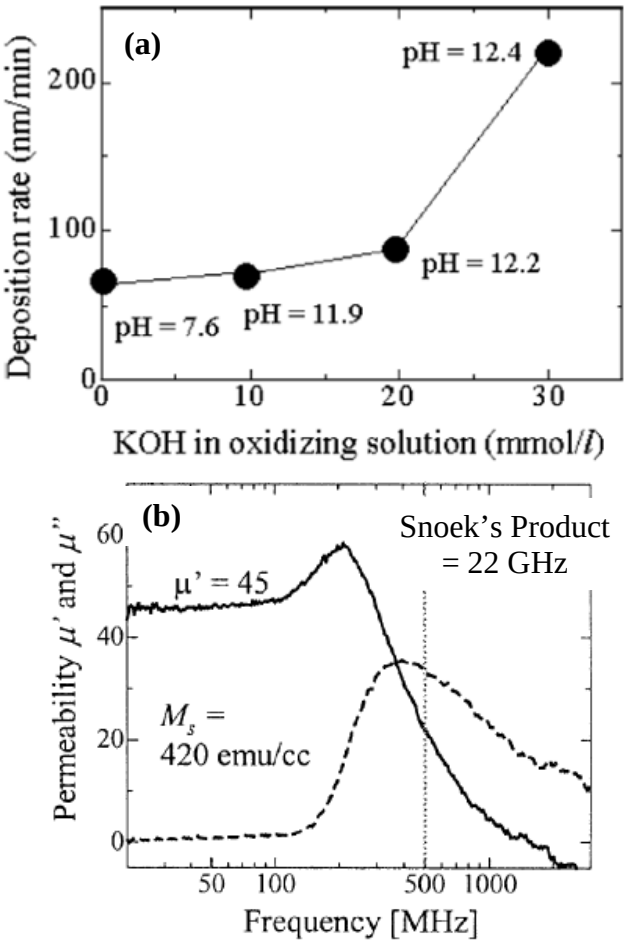

Fig. 47. (a) Represents the effect of concentration of the substituted buffer KOH on the deposition rate, and (b) is the complex permeability spectra of $Ni_{0.23}Zn_{0.15}Fe_2O_4$ using the substituted buffer, potassium acetate [13].

The next data set collected was the deposition rate of each film and the corresponding Snoek's product. A higher deposition rate leads to significantly reduced Snoek's product, as seen in Fig. 48. This may be a result of an increase in porosity, crack formation, and also crystallite size [4]. Since there are two deposition regimes, as described in chapter 2, there are different deposition rates that yield the highest quality

film. The μ-droplet regime performs the best at deposition rates below 30 nm/min. Abe *et al*. was able to deposit high quality films in the continuous liquid layer regime up to 73 nm/min by changing their oxidizing solution [13]. The reason for changing the oxidant was to avoid using ammonium complexes (NH_4) and increase the growth rate of the ferrite films [13]. To obtain a high deposition rate Abe *et al*. buffered their oxidizing solution with potassium acetate ($KOCOH_3$) and potassium hydroxide (KOH) as the pH buffer and adjuster, respectively [13]. Although, the pH buffer was changed the microstructure and Snoek's product remained the same [13].

Since the pH and deposition rate depend on eachother, the pH of the oxidant and the pH of the metal chlorides are closely examined for trends. There was a definite effect of oxidant pH on the Snoek's product, plotted in Fig. 49. The highest Snoek's product, 34.5 GHz, occurred at a pH of 8.277; the film was high quality, with uniform coverage and a concentration of $Ni_{0.19}Zn_{0.39}Co_{0.05}Fe_{2.38}O_4$. After plotting Snoek's product against the reactant pH no useful trend could be found, see Fig. 50.

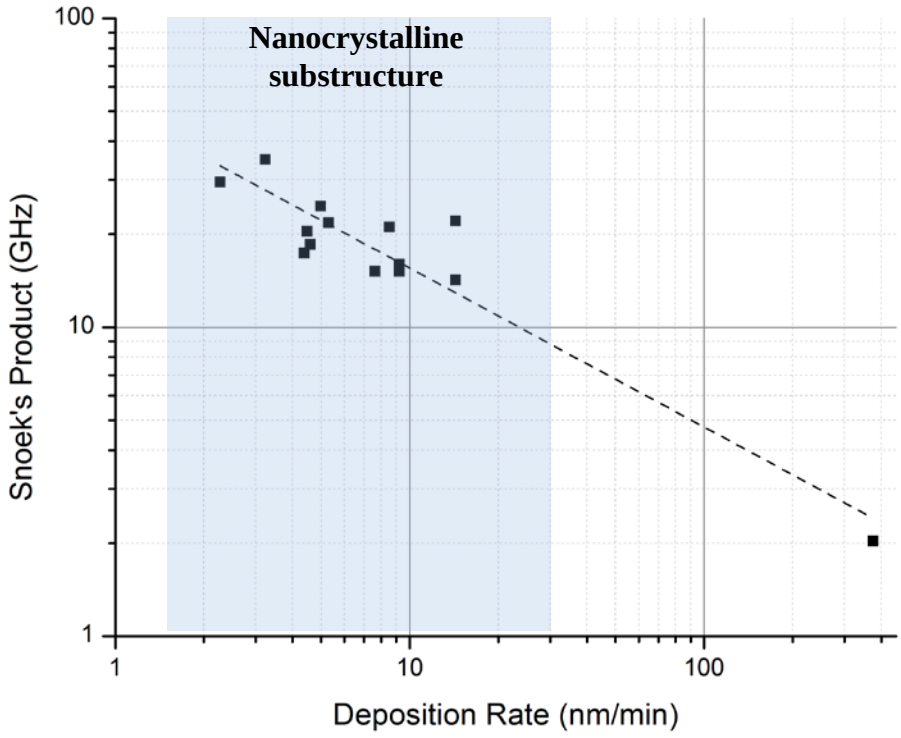

Fig. 48. Snoek's product as a function of deposition rate in the μ-droplet regime.

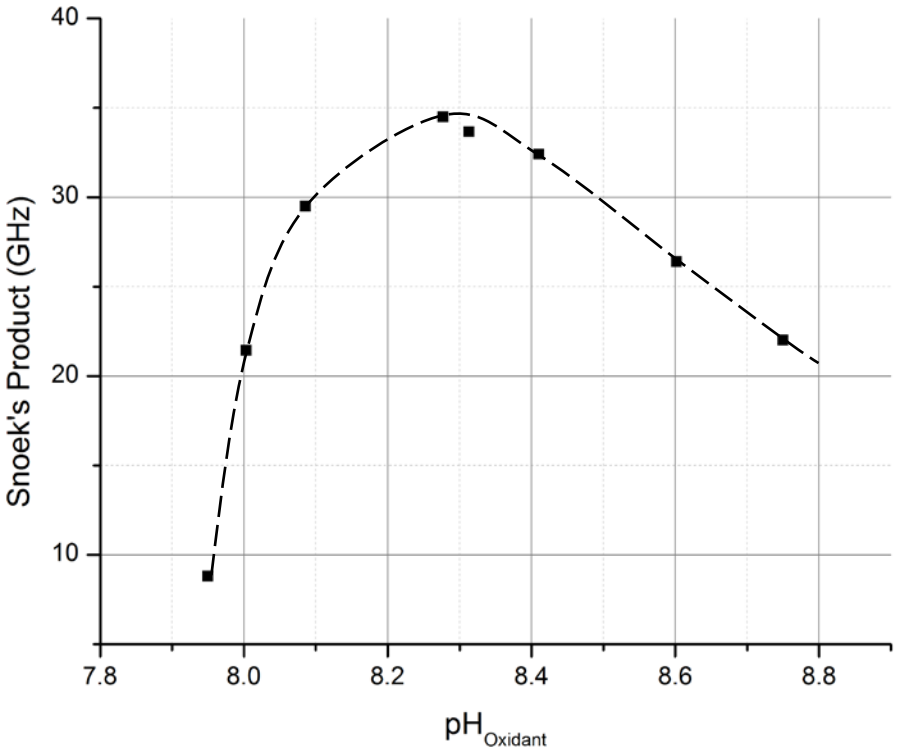

Fig. 49. Effect of Snoek's product over an increase in oxidant pH, with the highest value around 8.28 ($Ni_{0.19}Zn_{0.39}Co_{0.05}Fe_{2.38}O_4$) plotted for limited pH ranges.

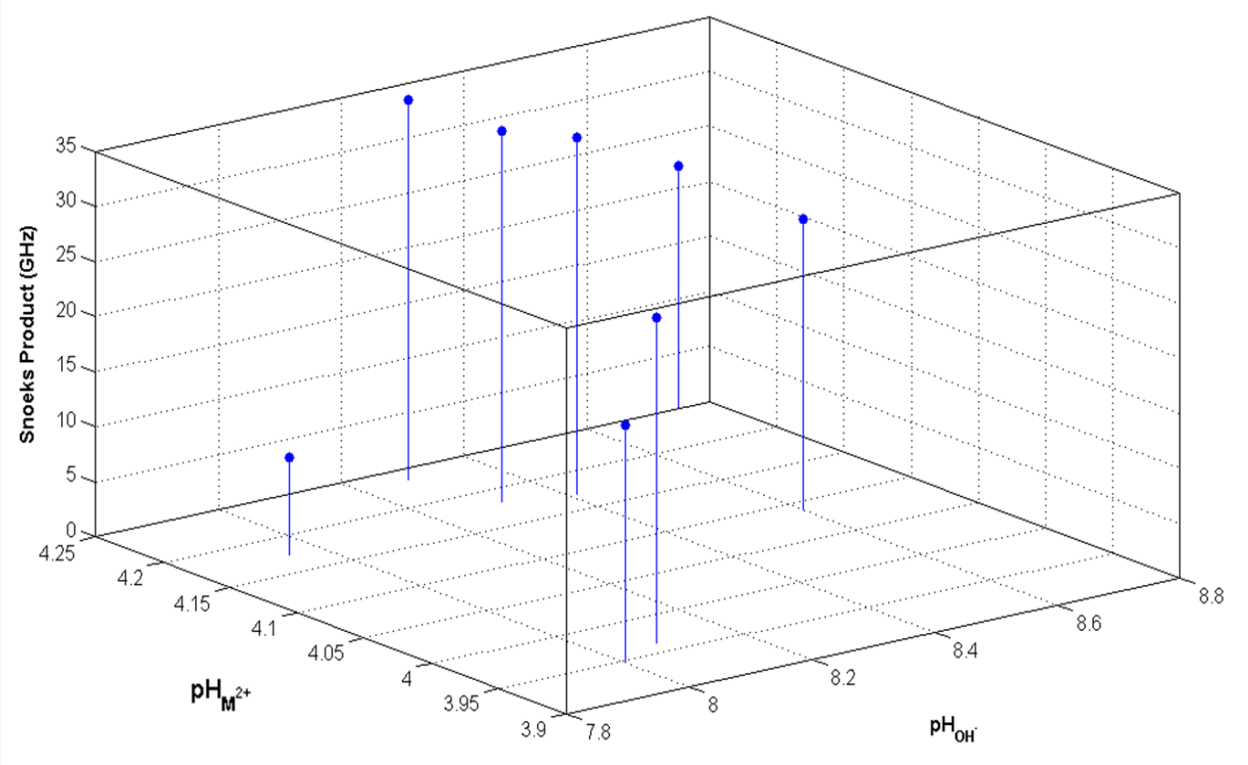

Fig. 50. The effect of oxidant and metal chloride pH on the Snoek's Product.

Comparing the results of films grown in the μ-droplet regime to those grown in the continuous liquid layer regime, as studied by Abe *et al*., a completely different trend line was observed [11, 13]. However, both regimes suggest that film morphologies change dramatically for oxidant pH of greater than 9.0 the film morphology changing from nanocrystalline columnar substructure to non-columnar. Coincidently, the Snoek's product significantly decreases, as well [11, 13]. Both trends have been plotted in Fig. 51, where the shaded region represents the columnar region for both the μ-droplet regime and the continuous liquid layer regime [11, 13]. Note the data used from Abe *et al*. came only from isotropic films to keep the data consistent.

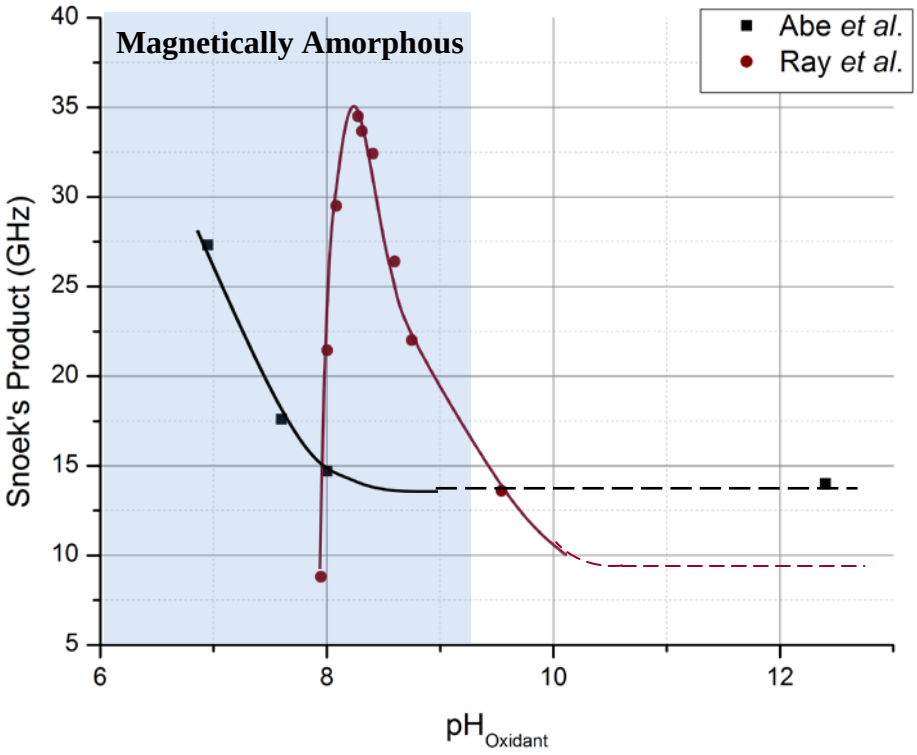

Fig.51. Snoek's product as a function of oxidant pH for the μ-droplet Collision Theory and the Sequential Reaction Theory [11, 13].

Macroscopic magnetic properties of materials are a consequence of magnetic moments associated with individual electrons [44]. Each electron has a magnetic moment associated with orbital and spinning motion [44]. The most fundamental magnetic moment is the Bohr magneton, μ_B, with a magnitude of 9.27E-24 A-m^2 [44]. For each electron in an atom, the spin magnetic moment is $\pm m_1\mu_B$, where m_1 is the magnetic quantum number of the electron [44]. The Bohr magneton of a spinel ferrite can give a good estimate of the spin contribution, which relates to the permeability, because that is

what is effectively being measure [45]. The spin of an electron is a universal property in all materials, states, and temperatures [45]. If the atom has a completely filled electron shell or subshells there is a total cancellation of both orbital and spin moments [44]. For an example, magnetite is an inverse spinel with a calculated Bohr magneton of 4 μ_B. Compared to the normal spinel zinc ferrite, with a Bohr magneton of 0 $\mu_{B,}$ magnetite is much more permeable. In the case of zinc ferrite, shown in Table IV below, the zinc cations force the iron cations onto the octahedral sites which cancel out the magnetic moment.

The permeability of the various ferrites has been measured using the microstrip permeameter. According to the calculated Bohr magneton the Ni-Zn-Co ferrite, it should have a higher magnetic moment than the simpler ferrite (Fe_3O_4, $NiFe_2O_4$, $ZnFe_2O_4$), which has been proven in Fig. 52. Figure 52 compares a Ni-Zn ferrite, composition $Ni_{0.21}Zn_{0.29}Fe_{2.50}O_4$, and a Ni-Zn-Co ferrite, with the composition $Ni_{0.19}Zn_{0.39}Co_{0.05}Fe_{2.38}O_4$. The addition of 2% cobalt increases the frequency while maintaining a high permeability consequently the Snoek's product from 17.70 GHz to 34.95 GHz.

Table IV. Calculated magnetic moments of common spinels [3].

Material	Spinel Type	Tetrahedral Sites	Octahedral Sites	$\mu_{B\ calc}$
Fe_3O_4	Inverse	Fe^{3+} ↓5 μ_B	Fe^{2+} ↑4 μ_B Fe^{3+} ↑5 μ_B	4 μ_B
$NiFe_2O_4$	Inverse	Fe^{3+} ↓5 μ_B	Ni^{2+} ↑2 μ_B Fe^{3+} ↑5 μ_B	2 μ_B
$ZnFe_2O_4$	Normal	Zn^{2+} ↑0 μ_B	Fe^{3+} ↑5 μ_B Fe^{3+} ↓5μ_B	0 μ_B
$Ni_{0.5}Zn_{0.5}Fe_2O_4$	Mixed	Zn^{2+} ↓0 μ_B*(0.5) Fe^{2+} ↓4 μ_B*(0.5)	Ni^{2+} ↑2 μ_B*(0.5) Fe^{2+} ↑4 μ_B*(0.5) Fe^{3+} ↑5 μ_B	6 μ_B
$Ni_{0.21}Zn_{0.29}Fe_{2.5}O_4$	Mixed	Zn^{2+} ↓0 μ_B*(0.29) Fe^{3+} ↓5 μ_B*(0.5)	Ni^{2+} ↑2 μ_B*(0.21) Fe^{2+} ↑4 μ_B Fe^{3+} ↑5 μ_B	6.92 μ_B
$Ni_{0.19}Zn_{0.39}Co_{0.05}Fe_{2.38}O_4$	Mixed	Zn^{2+} ↓0 μ_B*(0.39) Fe^{3+} ↓5 μ_B*(0.38)	Ni^{2+} ↑2 μ_B*(0.19) Co^{2+} ↑3 μ_B*(0.05) Fe^{2+} ↑4 μ_B Fe^{3+} ↑5 μ_B	7.38 μ_B

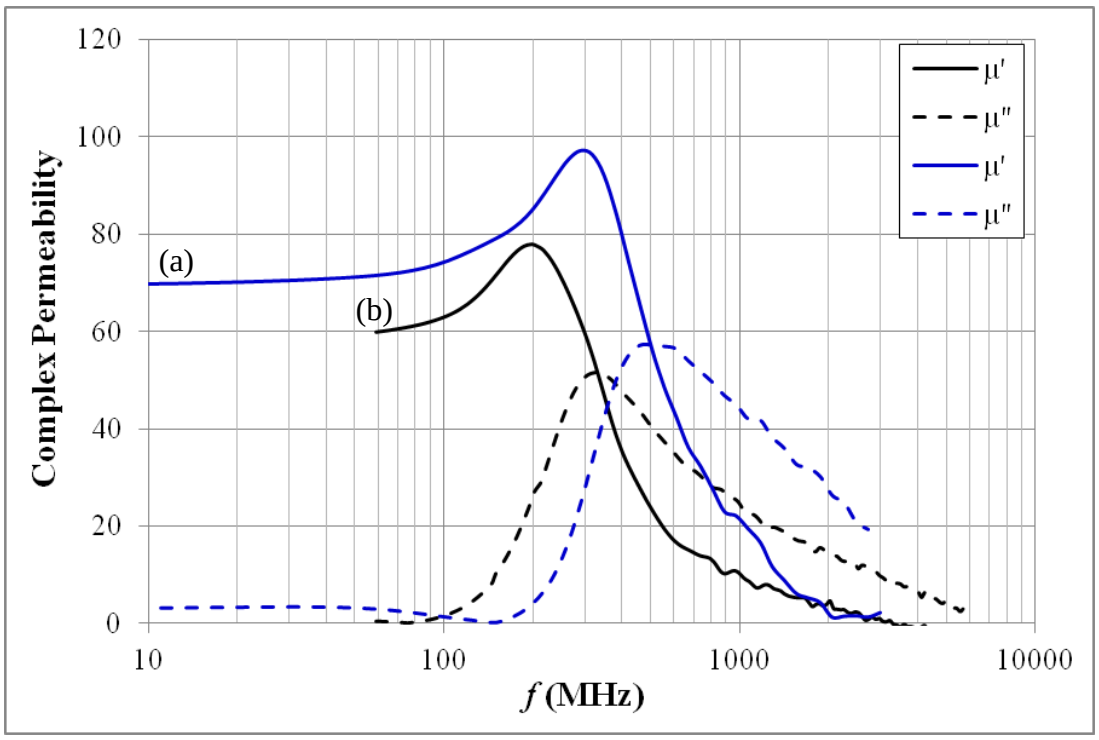

Fig. 52. Complex permeability spectra of (a) $Ni_{0.19}Zn_{0.39}Co_{0.05}Fe_{2.38}O_4$ in blue, and (b) $Ni_{0.21}Zn_{0.29}Fe_{2.50}O_4$ in black.

In Fig. 53, Abe and Matsushita *et al*. demonstrate ferrite films deviated from Snoek's product, as well, however not because of the same phenomenon. The Ni-Zn-Co spinel ferrites in Matsushita's research show a 2D spin dynamic phase shown with arrows in Fig. 53 [29]. The 2D spin dynamic phase is a heuristic theory and can be seen in other ferrite nanoparticles. It is suggested by Abe *et al.* that by adding 2% cobalt into the spin-spray process it creates in-plane anisotropy, which enhances the properties of the films [9]. Due to this phenomenon a so-called "2D spin dynamic" phase is created [9]. This phase is only seen when applying an external magnetic field, that aligns the domains in one direction, thus making the film directionally dependent.

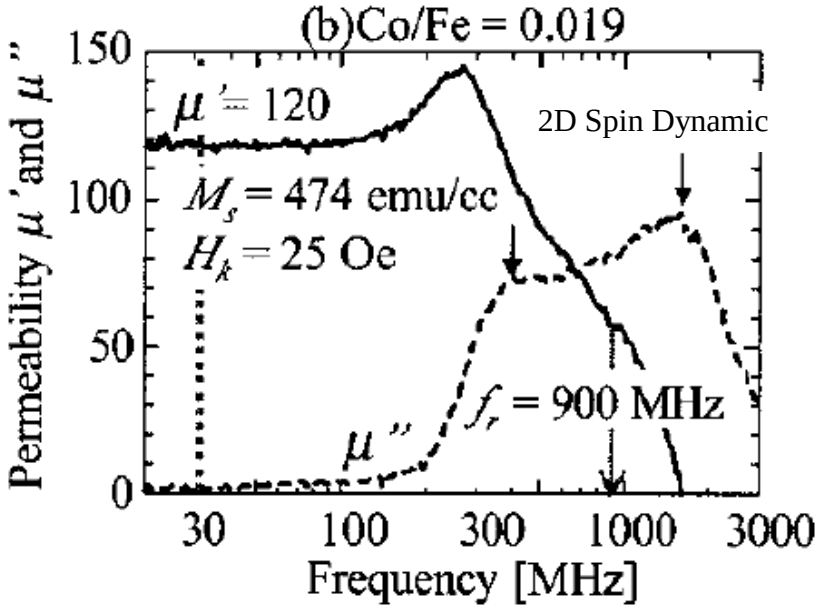

Fig. 53. 2D spin dynamic phase measure by Abe and Matsushita *et al.* [29].

Bulk Ni-Zn ferrites have very high permeabilities and low resonance frequencies. The Snoek's product ranges from 1.44 GHz to 3.95 GHz which are quite low compared to the thin film ferrites deposited using the spin-spray deposition method, which range from 2.03 GHz to 34.95 GHz depending on the deposition rate. In this particular research, Snoek's law is exceeded, most likely due to having multi-grain domains (MGD), which will be discussed later in chapter 4. The data from our experiments have been collected and combined to develop a ternary composition map of Snoek's product as a function of cation composition of the nickel, zinc, and iron cation fractions with an added fourth dimension in Fig. 54. Figure 54 was developed using MatLab®, which used a meshgrid to plot the surface contour of the measured Snoek's product. The meshgrid

produced a three-dimensional coordinate array creating the contour. Each composition has a fixed 2% cobalt amount. Within this space, the composition exhibiting the greatest Snoek's product was $Ni_{0.19}Zn_{0.39}Co_{0.05}Fe_{2.38}O_4$.

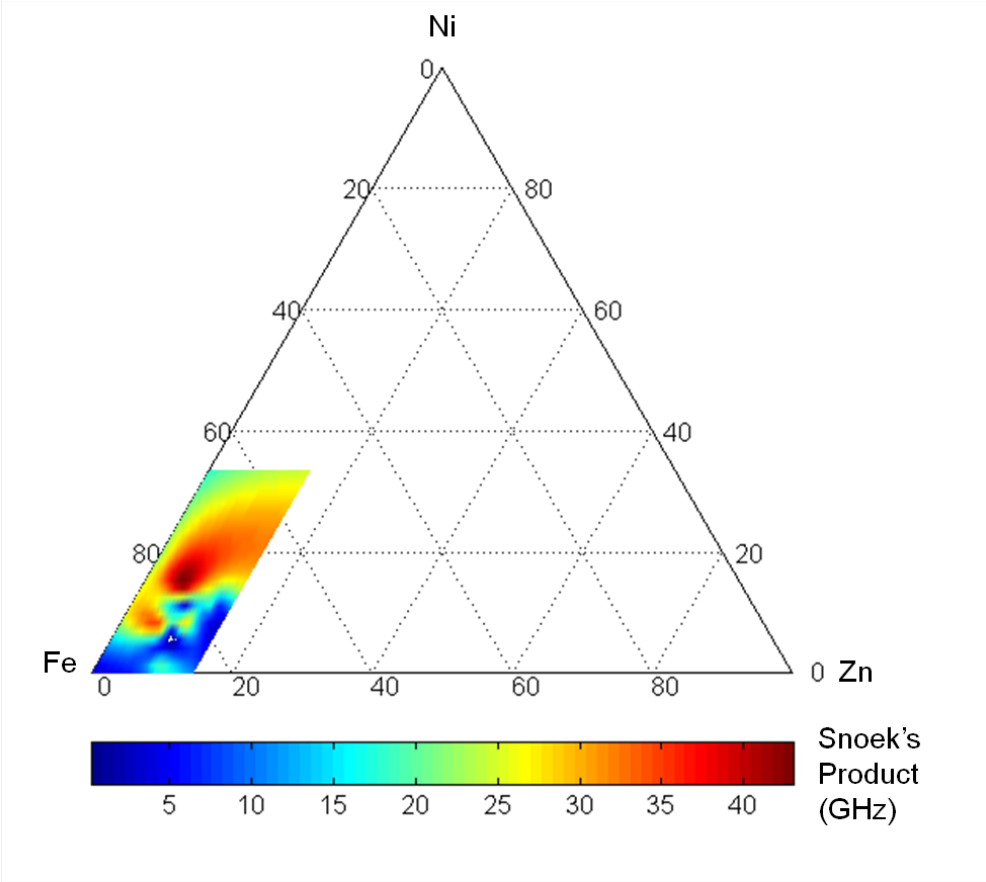

Fig 54. Typical Snoek's product values for Ni-Zn-Co ferrite are on average 17.34 GHz, where Co is added at a constant concentration of 2% [46].

MAGNETIC RESULTS AND DISCUSSION

The purpose for adding cobalt originally was to increase the frequency. The results shown in Fig. 55, that plots magnetism versus applied magnetic field, shown that

the magnetic saturation, M_S, and remnant, M_R, field has increased seen in Fig. 55. For the composition $Ni_{0.24}Zn_{0.61}Co_{0.02}Fe_{2.13}$ the magnetic saturation is 556 emu/cc (0.70 T), the remnant magnetization is 332 emu/cc (0.41 T) and the coercive field is 91.3 Oe. This hysteresis loop suggests it is a soft magnet given the shape of the loop and narrowness of the loop. Note in figure, two hysteresis loops were taken.

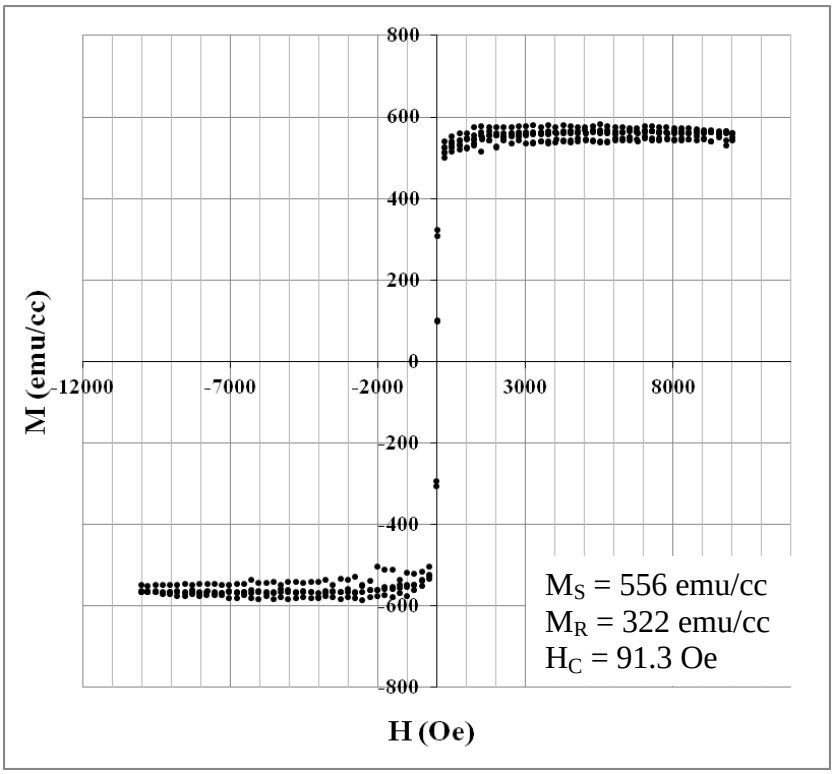

Fig. 55. Hysteresis loop for $Ni_{0.24}Zn_{0.61}Co_{0.02}Fe_{2.13}$.

Coercivity is used to distinguish between hard and soft magnets. It is a structure sensitive magnetic property, and can easily be affected by heat treatment or deformation. The coercivity of a soft magnet typically ranges from 12-125 Oe (954.9 A/m to 9947.2

A/m), whereas it is typically hard magnet is greater than 125 Oe for a hard magnet [6]. Additionally, magnetic inclusions, such as second-phase particles, with different magnetic properties from those in the matrix material cause changes in the hysteresis properties which in turn change the shape of the loop [47]. Second-phase particles introduce pinning sites that impede domain wall motion which increase coercivity and hysteresis loss [48]. The particle diameter also influences the coercive field in the magnetic hysteresis loop as seen in extensive length by Herzer *et al*. [5, 49, 50]. When the grain sizes are larger than the critical exchange length, L_{ex} ($\cong$ 40 nm), the coercivity decreases as the grains divide into multidomain grains (MD) [5].

A typical diagram plotting the coercivity as a function of a grain size is shown in Fig. 56 for materials. Herzer *et al*. was one of the first to publish results for soft magnetic materials in 1990 [49]. Shown in Fig. 56 there is an increase in H_c with grain size in the single-domain (SD) region, D^6, for grains up to 40 nm in diameter [45, 49]. For grains in the region labeled 1/D, they reside in the multidomain (MD) region, more than one domain per grain [45, 49].

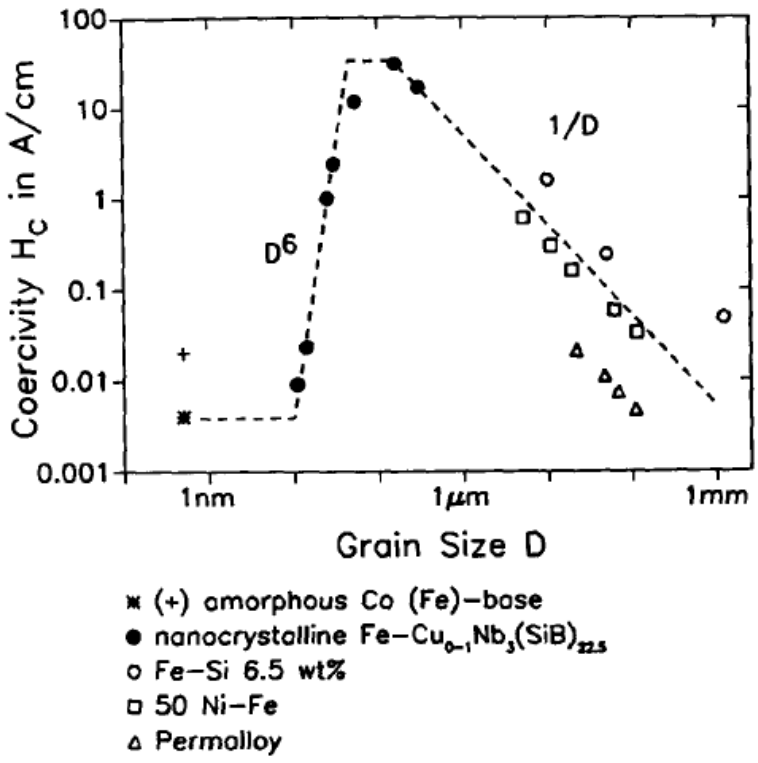

Fig. 56. Coercivity as a function of grain size for various soft magnetic material [49].

Since all materials behave differently, spinel ferrites from literature were plotted the same way in order to see where the spin-spray deposited thin films would fall on the graph, this is shown in Fig. 57. The trend formulated is very similar to what Herzer *et al.* established in 1990, however, the data collected from ASU's deposited films from the spin-spray process does not quite fit on the graph. This is most like caused by the magnetic domains. For the Ni-Zn-Co ferrites the spin-spray deposition method creates multi-grain domains (MGD), which essentially means there is more than one grain per magnetic domain region; this will be discussed at length in chapter 4. There are many different domain theories, including but not limited to the Stoner-Wohlfarth Model, the

Kittel Theory, the Phenomenological Theory, and the Random Anisotropy Model [45, 51-54].

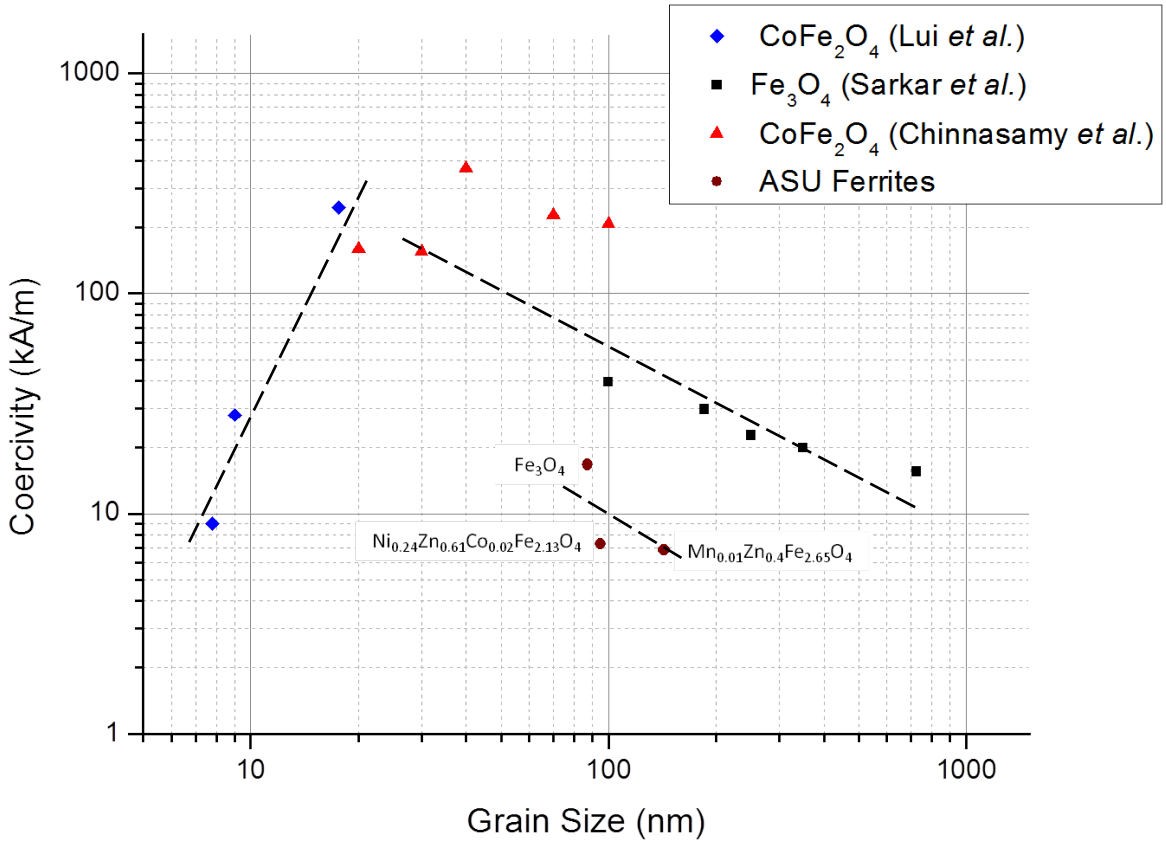

Fig. 57. Coercivity as a function of grain size for various spinel ferrites reported in the literature and compared to the ASU samples [54-56].

Stoner-Wohlfarth Model.

The Stoner-Wohlfarth Model is widely used for single-domain grains, which assumes the particle has uniaxial anisotropy and is in an equilibrium state [53]. The next assumption is that all the magnetic moments within in the particle are always aligned

parallel at any given point [53]. Stoner *et al.* used the second derivative of the energy of a system, shown in Eqn. (18) and plotted a hysteresis loop [53].

$$E = K_u V \sin^2(\phi - \theta) - \mu_0 M_s V H \cos\theta \tag{18}$$

where V is the volume, M_s is saturation magnetization, and μ_0 is the vacuum permeability. By taking the second derivative of Eqn. (18) and plotting m_h vs. h, a hysteresis loop is made [53].

$$\frac{\partial^2 \eta}{\partial^2 \phi} = \cos\big(2(\phi - \theta)\big) + h\cos\phi > 0 \tag{19}$$

Different materials produce different shapes of curves [53]. The hysteresis loop shape strongly depends on the angle between the magnetic field and the easy axis; the larger the angle, the more reversible the rotation occurs [53]. These calculations apply to identical, isotropic and uniaxial magnetocrystalline particles [53]. In reality, each material, or sample, will have a unique K_u value [53]. From the hysteresis loop the domain states, single-domain or multidomain, can be measured by plotting M_{rs}/M_s vs. H_{cr}/H_c [57]. Where M_{cr} and H_{cr} are the remanent saturation and remanent coercivity, respectively [58].

Kittel Model.

By 1950, another theory emerged, established by Charles Kittel, which was much simpler than the Stoner-Wohlfarth Model. Kittel *et al*. performed a simple experiment to saturate a sample consisting of magnetic particles suspended in a non-magnetic matrix

[45, 59]. The field required to saturate nickel or iron is considerably larger in a multidomain particle than in a single-domain particle [59]. The first sample (a) has particles so small that it never forms a domain wall, and thus is always is single-domain; and (b) a larger particle, with a multidomain structure [59].

(a) Had a virtually spherical shape and was 200 Å in diameter. The field required to saturate the sample was 550 Oe [45, 59]. From the saturation value, single-domain particles can be concluded, even though the value was slightly higher than expected [59].

(b) To saturate the particle, it is necessary to overcome the maximum demagnetizing field, $4\pi I_s/3$ for a sphere. For sample (b) The spherical carbonyl particles, 8 μm in diameter, and saturated at 2100 Oe [59]. Hence the particles in sample (b) formed a multidomain structure [59].

In summary, Kittel *et al*. stated the idea that the energy density for multidomain particles must be supplied by an external magnetic field, while with single domain particles the amount of energy density is always present. Refer to Eqn. (20) for single domain particle and Eqn. (21) for multidomain particles [45, 59, 60].

$$H_s = \frac{2K}{M_s} \tag{20}$$

$$H_m = \frac{4\pi M_s}{3} \tag{21}$$

Here M_s, is the magnetization saturation and K is a constant [60].

Phenomenological Theory.

In 2006, Abe *et al*. established their own domain theory for the spin-spray deposition method [51]. The "Phenomenological Theory" suggests columnar growth of spin-spray plated spinel nanocrystallites that are smaller than the individual domain, shown in Fig. 58 [51]. Each crystallite saturates along an easy axis lying in the film plane, and exchange coupling occurs within a group of crystallites, forming a domain with a well-defined direction [51]. Due to the demagnetizing effect, the film is divided into magnetic domains, shown in Fig. 58a, where each crystallite is aligned along one of the six easy magnetization directions, and the overall orientation is random [51].

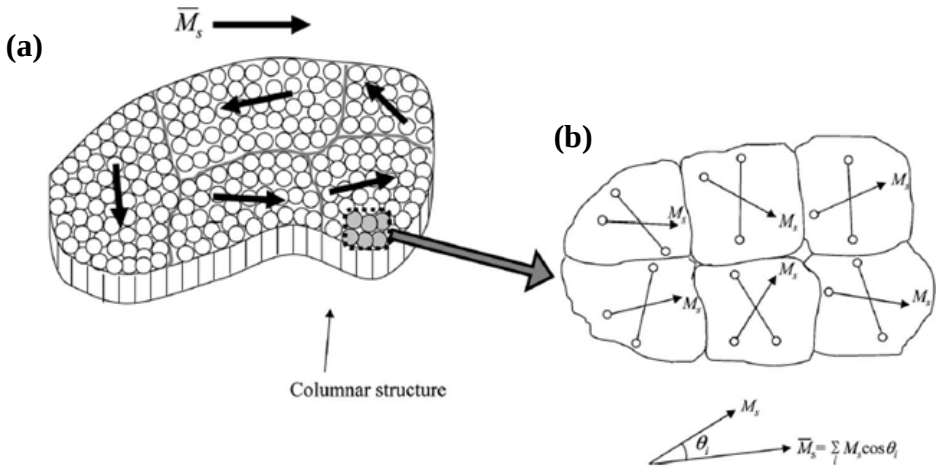

Fig. 58. An illustrated magnetic domain structure as proposed by Abe and Matsushita in spin-sprayed ferrite films with the columnar structure, (a) macroscopic magnetization, $\overline{M}_s$, and (b) magnetization of crystallites along easy magnetization directions [51].

The in-plane properties for a two-dimensional material is similar to a multidomain polycrystalline material [51]. Therefore, the random symmetry along the plane yields $D_x = D_z = 0$, and $D_y = 1$ (film is thin) and there is no net depolarization effect [51, 61]. For a field applied in a random direction on the plane the susceptibility would be the average of X_{xx} and X_{zz}, which is seen in Eqn. (23).

$$X_{xx} = 0, X_{yy} = \frac{4\pi M_s}{H^A + 4\pi M_s(D_y - D_x)}, X_{zz} = \frac{4\pi M_s}{H^A + 4\pi M_s(D_z - D_x)} \quad (22)$$

$$X_{avg} = \frac{4\pi M_s}{2H^A} \quad (23)$$

Where D_x, D_y, and D_z are depolarization factors, and X_{xx}, X_{yy}, and X_{zz} are directional susceptibilities, and hence X_{avg} is the average susceptibility [61]. From these equations the permeability can be derived using the relation, $X_{avg} = \mu - 1$.

The phenomenological theory gives a plausible explanation for exceeding Snoek's limit using the spin-spray method, however there are many problems with this journal article [51]. The first issue is with the misleading title of "Phenomenological theory of permeability in films having no in-plane magnetic anisotropy: Application of spin-sprayed ferrite films [51]." In actuality, the high permeability and high frequency occur when Co^{2+} is added to spin-spray process while an external magnetic field is applied. Abe *et al*. have reported their highest Snoek's product producing films using this method [9].

Chapter 4

STRUCTURE AND MAGNETIC PROPERTIES

Spin-spray deposition of spinel ferrite films at low temperatures was developed by spraying a reaction solution ($FeCl_2$, $NiCl_2$, and $ZnCl_2$) and oxidizer solution simultaneously onto a heated rotating platen. Lorentz TEM observations of magnetic domain walls, grain boundaries, and cross-sections were performed on Ni-Zn-Co ferrite thin films. The films were deposited uniformly and have columnar crystallites 80 – 150 nm in diameter. Multi-grain domains (MGD) were observed owing to the high Snoek's product. The magnetic domains were on average 235.71 ± 109.54 nm and the smaller physical grains were on average 95.13 ± 38.76 nm in size. This observation suggested an explanation why these materials have higher Snoek's products than for bulk materials where the physical grain size is larger than the magnetic domain size.

INTRODUCTION

Recently spinel ferrites have received a great deal of attention for their uniquely tunable properties such as resistivity, permeability, coercive field and core losses [6, 62]. Ferrite films are usually developed using vapor deposition or epitaxy techniques [6]. However, with one extra advantage of developing deposition techniques for ferrite thin films at low temperatures, 90°C, is that a variety of substrate materials can be used, including on plastics. This method was first demonstrated by Abe *et al.* [16, 63]. In this study, the Ni-Zn-Co ferrite films were deposited and magnetically characterized into the gigahertz range, well beyond conventional bulk ferrites. These films are isotropic

materials which make them viable for low-loss broadband communications, miniaturized low-microwave inductors, or for antenna applications.

For most applications, such as electromagnetic interference (EMI) devices, the permeability and resonant frequency are the main consideration [52, 64]. In this research, the Multi-Grain Domains (MGD) contribute to the high permeabilities and high resonant frequencies built up by the μ-droplet regime [16, 63]. In order to prove this theory Lorenz transmission electron microscope (TEM) of the magnetic domains were imaged, as well as the grain boundaries and cross-sections of the film.

Magnetic domains are formed to reduce the magnetostatic energy which is the magnetic potential energy in the flux lines [6]. Their size and geometries are determined by the reduction of magnetostatic, magnetocrystalline anisotropy, magnetostrictive, and domain wall energy [6]. Other factor contributing to the domain structure are voids, grain boundaries, and non-magnetic inclusions [6].

EXPERIMENTAL PROCEDURE

Nickel zinc cobalt ferrite films, of compositions $Ni_{0.24}Zn_{0.61}Co_{0.02}Fe_{2.13}O_4$ (Film #1) and $Ni_{0.18}Zn_{0.50}Co_{0.05}Fe_{2.27}O_4$ (Film #2), were deposited onto silicon wafers using the spin-spray plating method. The reactant solution of $FeCl_2$ + $NiCl_2$ + $ZnCl_2$ + $CoCl_2$ and the oxidant solution containing $NaNO_2$ + CH_3COOH + NH_4OH were sprayed simultaneously onto a rotating platen heated to 90°C [15, 65]. The ferrite layer built up through sequential exposure and reaction.

The complex permeability spectra were measured to distinguish between the domain wall and spin rotation contributions [66]. The instrument used to measure the real, μ', and imaginary permeabilities, μ'', effects on frequency were a vector network analyzer with a customized microstrip permeameter [42, 67].

The samples were then prepared for examination by TEM first by sectioning and cutting them down to size a size that would fit in the instrument. The next step was to thin the actual sample by polishing down to about 100 μm thickness, and then dimpled to create thin area with thickness smaller than 10 μm. Further thinning was down by argon ion-milling, rendered the material to be electron transparent regions [68].

RESULTS AND DISCUSSION

Permeability Measurements.

Figure 59 plots the real and imaginary parts of the complex permeability for film #1, $Ni_{0.24}Zn_{0.61}Co_{0.02}Fe_{2.13}O_4$, and film #2, $Ni_{0.18}Zn_{0.50}Co_{0.05}Fe_{2.27}O_4$. Both films exhibited high permeability and high frequency properties. The Snoek's limit was exceeded for both films and calculated for each film as 18.4 GHz and 12.0 GHz, respectively. These values are at least a factor of 10 greater than bulk $(Ni, Zn, Co)_xFe_{2-x}O_4$ spinel ferrite which is typically 1 - 3 GHz. Figure 59b, film #2, has considerable noise compared to film #1 due to its relative thickness. It reached the lower limits of the permeameter, which is about 300 nm. These are typical permeability graphs for spin-

spray deposited films using the μ-droplet regime, and are comparable to plots in literature for films deposited by the continuous liquid layer regime.

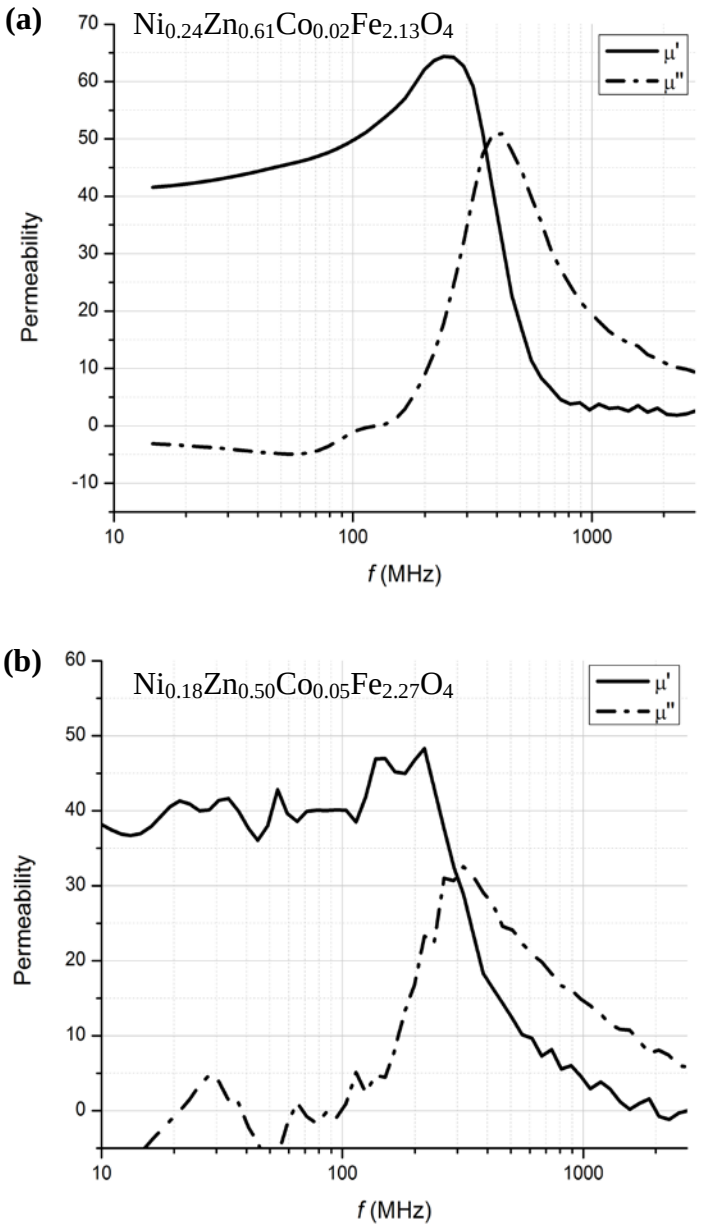

Fig. 59. Complex permeability spectra of (a) film #1 and (b) film #2.

Sample Morphology by Scanning Electron Microscopy.

Each sample was analyzed by SEM (Hitachi S7800) for thickness, grain morphology and sizes, and structural changes. Typical thicknesses, excluding the substrate, range from 0.6 – 12 μm. The growth rate and particle size were dependent on the oxidant pH. If the pH was higher (pH > 9.0) the growth rate and particle size increases. Current growth rate ranges from 4.0-18.0 nm/min, with the optimum growth rate at 4.0 nm/min. The microstructure for Ni-Zn ferrite and Ni-Zn-Co ferrite was very similar. The thin films were columnar in appearance consisting of a nanocrystalline substructure, seen in Fig. 60-63. There are different substructures ranging in size from, 15-30 nm nanocrystalline substructures, the tops of the columns range from 100 - 500 nm, and 0.3 – 12 μm thickness. Figure 64 displays a significantly higher growth rate and a non-uniform structure. This difference is caused by the significantly low amount of zinc and the high pH of the aqueous solution.

Imaging the thicknesses of the thin films is crucial to this research, as well as documenting the conditions of this deposition. The thickness was dependent on the position of the nebulizers; which was directly beneath the nebulizers. The difference in thickness across the film is caused from not having a continuous liquid layer on the substrate; which was found by simulated results using CFD in Fig. 65, by Heath Lorzel [69]. Matsushita and Abe resolved this issue by placing two separate sample substrates, 5 cm by 5 cm, directly underneath the nozzles [11], instead of attempting to deposit uniformly over the entire substrate. The fluid flow simulation assisted in re-positioning

the nebulizers in order to maximize the deposition area uniformly and utilize the μ-droplet growth regime.

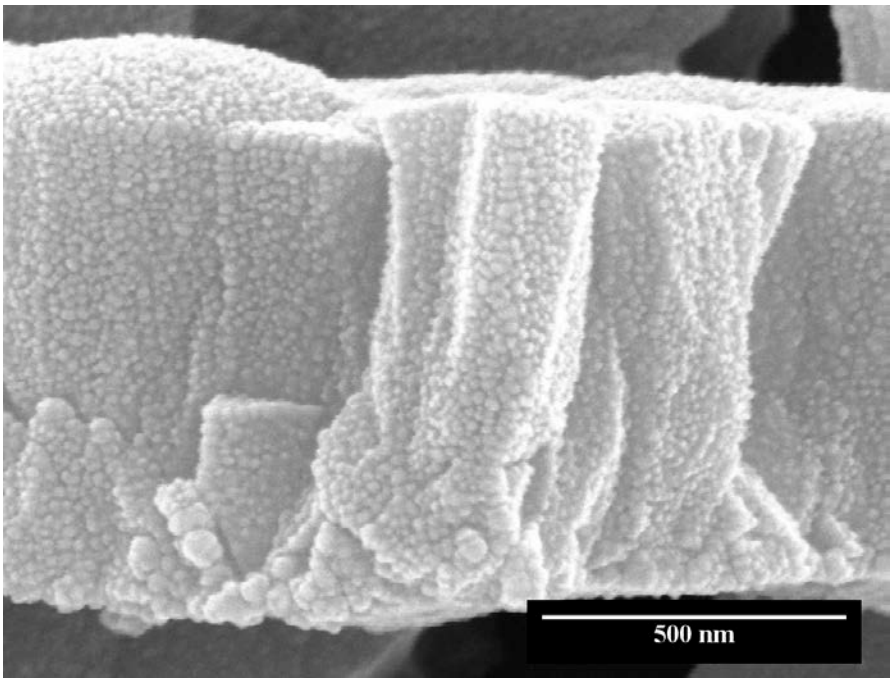

Fig. 60. Columnar structure of $Ni_{0.19}Zn_{0.30}Co_{0.05}Fe_{2.46}O_{4,}$ sample NZCF110128.

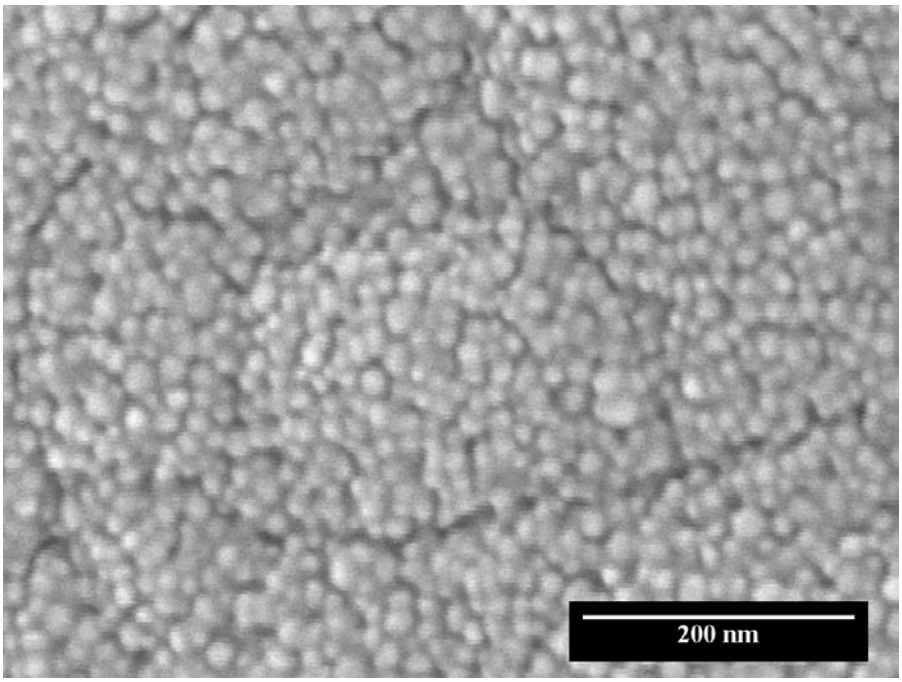

Fig. 61. . Ni-Zn-Co ferrite plan view sample with a composition,

$Ni_{0.19}Zn_{0.30}Co_{0.05}Fe_{2.46}O_4$, sample NZCF110128.

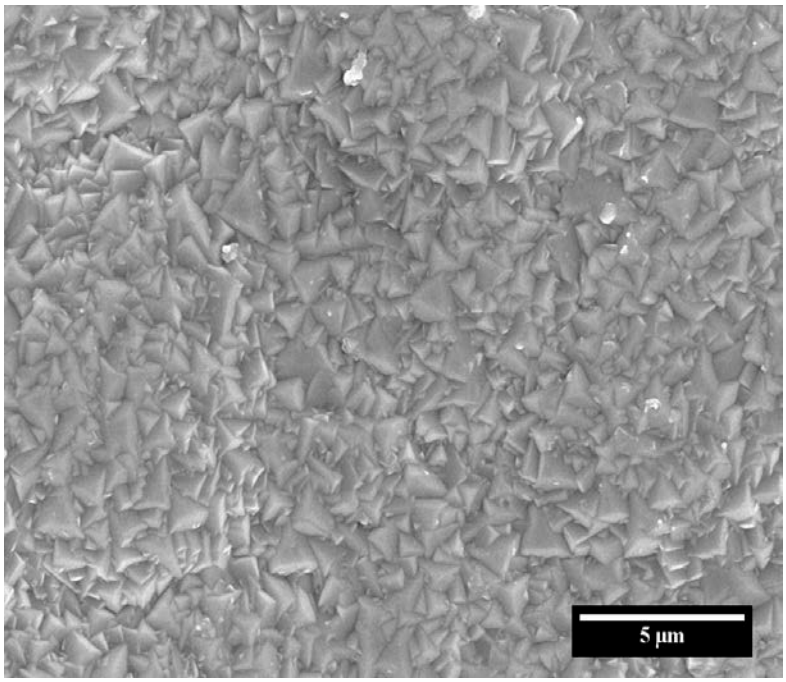

Fig. 62. After long-term deposition, in plan-view, with a composition $Ni_{0.31}Zn_{0.25}Co_{0.04}Fe_{2.40,}$ sample NZCF111117.

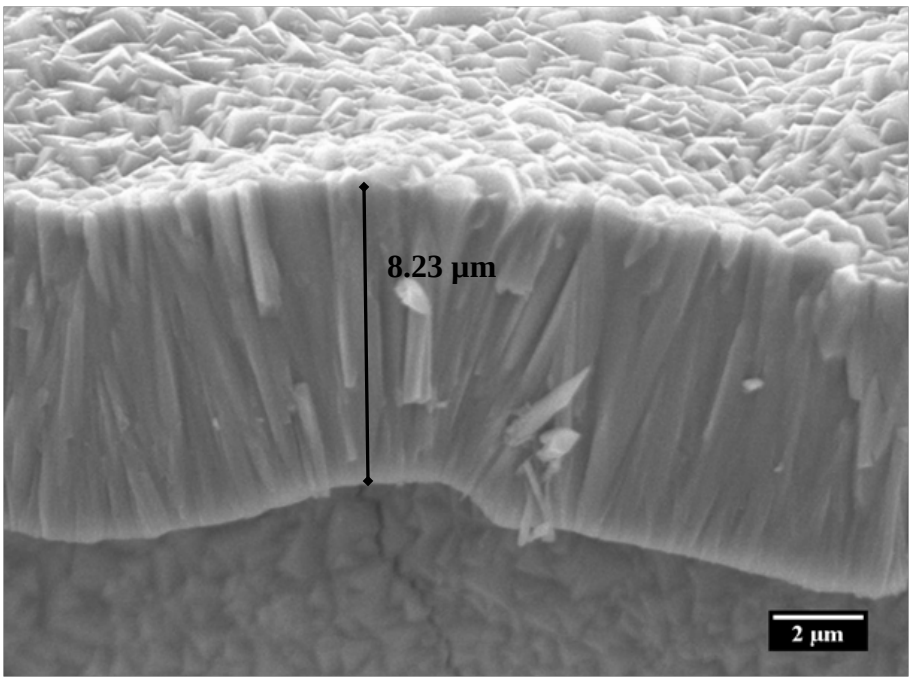

Fig. 63. Ni-Zn-Co ferrite sample with a composition, $Ni_{0.31}Zn_{0.25}Co_{0.04}Fe_{2.4}O_4$, thicker film grown than usual but the properties and microstructure have been maintained, sample NZCF111117.

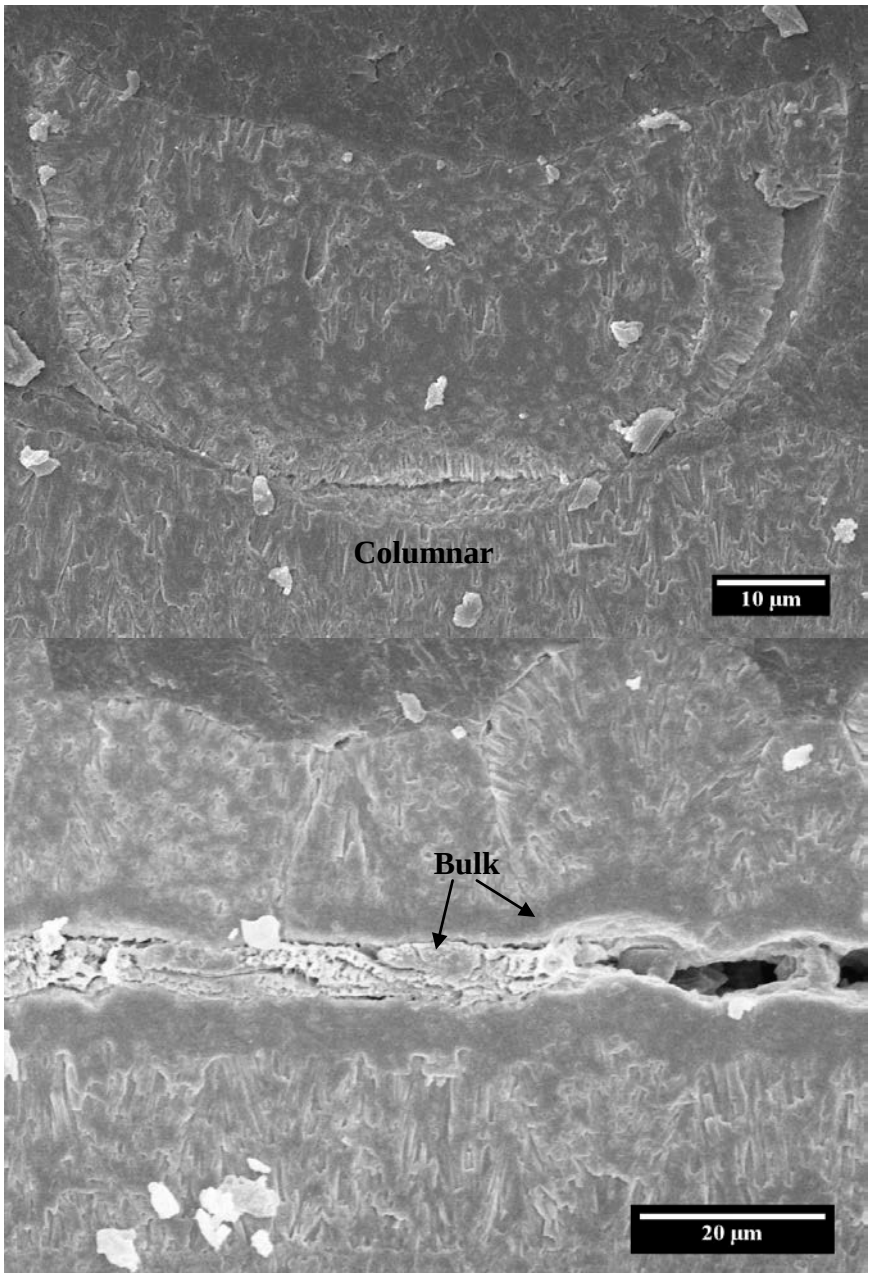

Fig. 64. Spinel ferrite sample, NZCF110823, composition $Ni_{0.23}Zn_{0.33}Co_{0.05}Fe_{2.40}O_4$, depositing at an extremely fast rate of 375 nm/min, (a) representing columnar features and (b) showing bulk material.

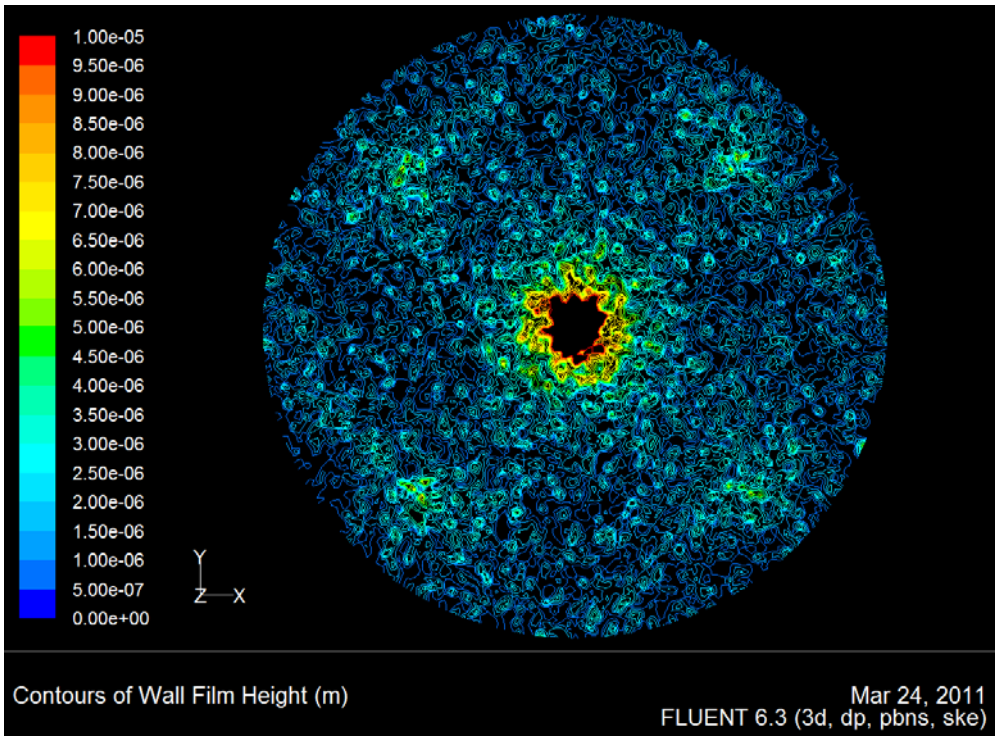

Fig. 65. FLUENT simulation of the contours of droplet density represented as average liquid film height on reactor platen (using six nebulizers) [69].

Lorentz TEM.

Figure 66 presents a bright-field TEM image in plan-view geometry, from which the nanocrystalline amorphous column geometry and size could be determined. The diffraction contrast is caused by the different crystal directions among the nanocrystalline columns. Bright areas between some of the grains suggest porosity, although some of these were generated by the milling process.

Figure 67 is a high magnification plan-view TEM image. The purpose of this is to reveal substructures and defects within the nanocrystalline columns. Defects and defect

systems such as dislocations and stacking faults (labeled in Fig. 67) reveal a mottling in the contrast that suggests domain sizes that are much smaller than the physical grain itself. Combined with the lattice strain, these defects contribute to an especially complicated diffraction contrast in the image. Notice that bright field images are constructed using diffraction contrast, in Fig. 66 the mottling seen is caused by different crystallographic orientations and compositional variations. The light regions in the bright field image are caused from pores formed by the milling process.

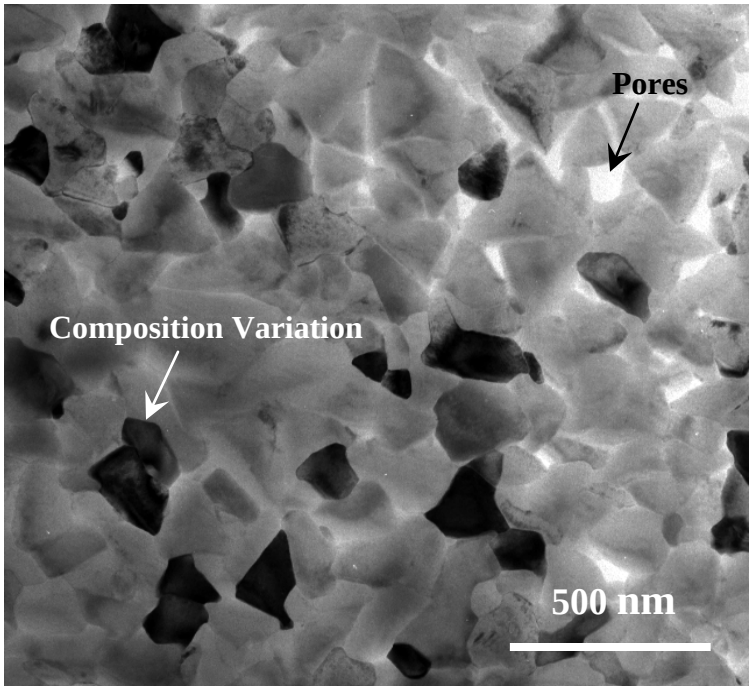

Fig. 66. Bright-field TEM image with grain size averaging 95.13 ± 38.76 nm of film #1.

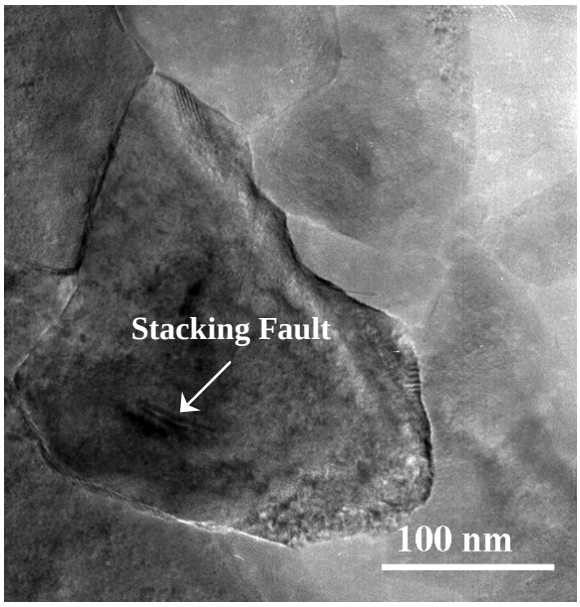

Fig. 67. High magnification TEM plan-view image, film #1.

Since compositional variation was noticed on the bright field images, a scanning transmission electron microscopic (STEM) image was taken with a corresponding energy dispersive x-ray spectroscopy (EDXS) line profile. The line profiles of nickel, zinc, cobalt, and iron decrease fractionally about the same; it is likely the graph is changes as an artifact of the measurement. The estimated beam size is about 2 nm and has an energy resolution of 130 eV, see Fig. 68a and 68b.

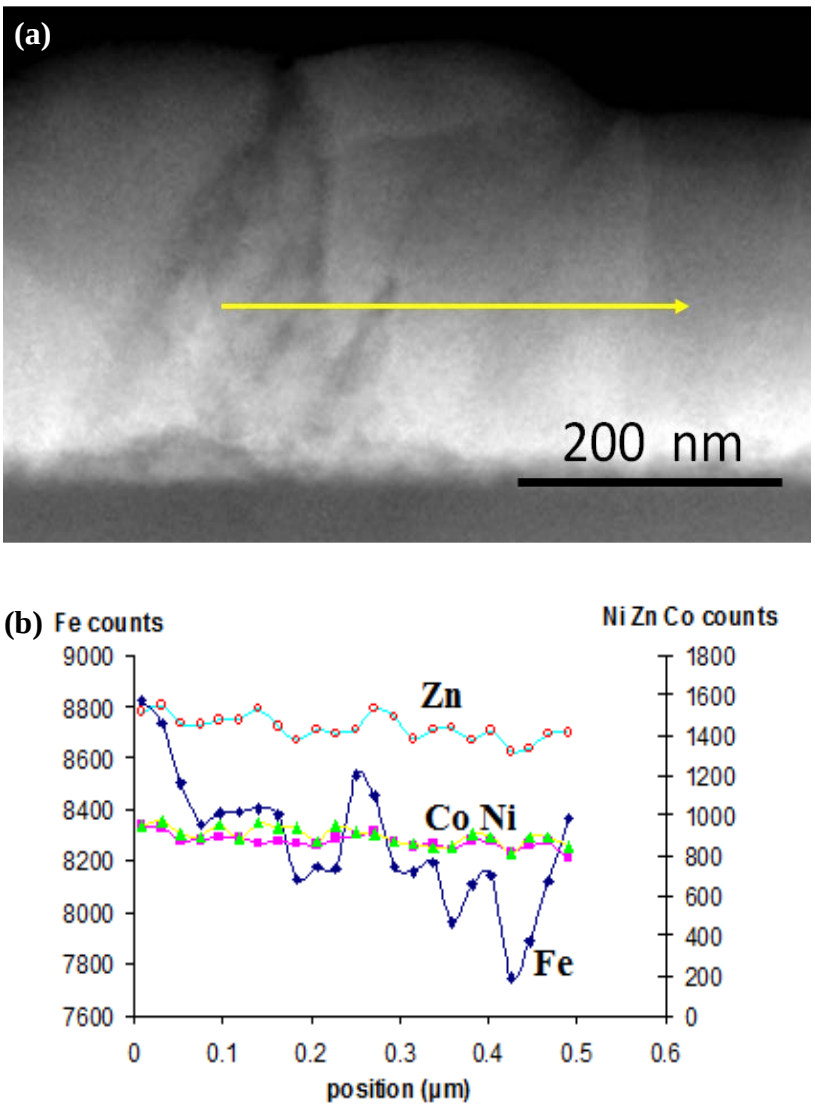

Fig. 68. (a) STEM image showing the (b) corresponding line profiles for Ni, Zn, Fe, and Co using EDXS.

Each grain column consists of a nanocrystalline substructure, each of which looks like single crystal texturing within a larger grain. This can be concluded from Figs. 69 and 70, even if there is not a perfect crystal within the actual column. In other words the nanocrystalline column boundaries are seen as crystal grain boundaries; see Fig. 70 for a

wider representation. The boundaries vary in shape and size, and often are filled with amorphous material, which may influence the magnetic properties. Since the magnetic domain boundaries are broken up to reduce the total energy in the system the magnetic field does not penetrate the amorphous regions in the material.

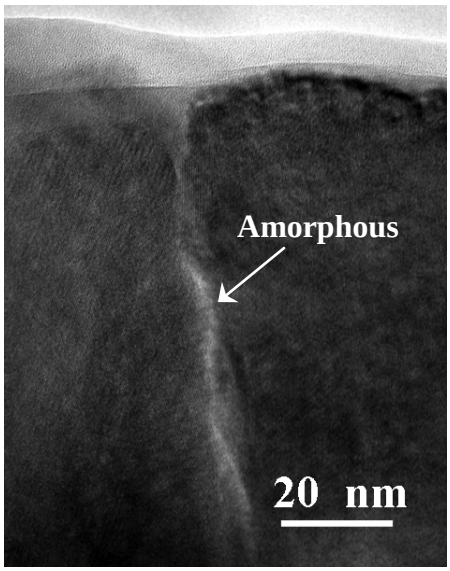

Fig. 69. TEM cross-section, showing a grain boundary filled with amorphous material in film #2.

The low magnification bright field cross-section TEM image, Fig. 70, establishes a very clear view of the columnar structure. This image shows a high quality film growth in the μ-droplet regime. The ferrite columns are firmly attached to the glass substrate, and show a uniform thickness.

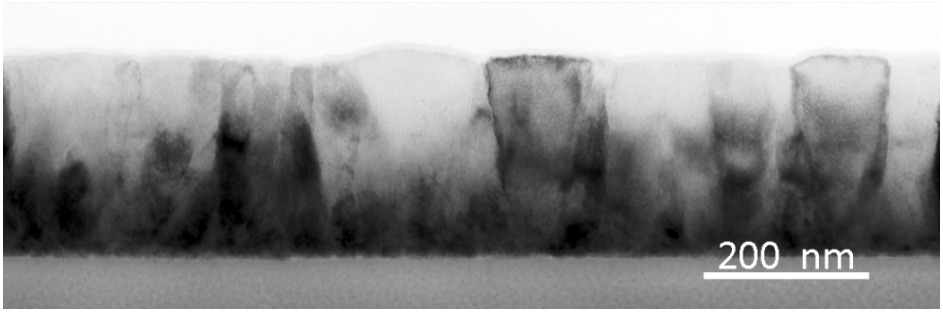

Fig. 70. Cross-section of film #2 showing single crystalline spinel ferrite.

Using off-axis electron holography an electron phase distribution map can be generated. The electron phase map contours parallel to magnetic field lines integrated in the incident beam direction. To locate the magnetic domain, the direction of the phase gradient on the sample is needed. With "Digital Micrograph" (DM) software processing the gradient map is obtained. The color represents the gradient directions of the magnetic field, and the color wheel indicates the relation between the gradient and color. From the gradient map the magnetic domain can be established on the original image, see Fig. 71.

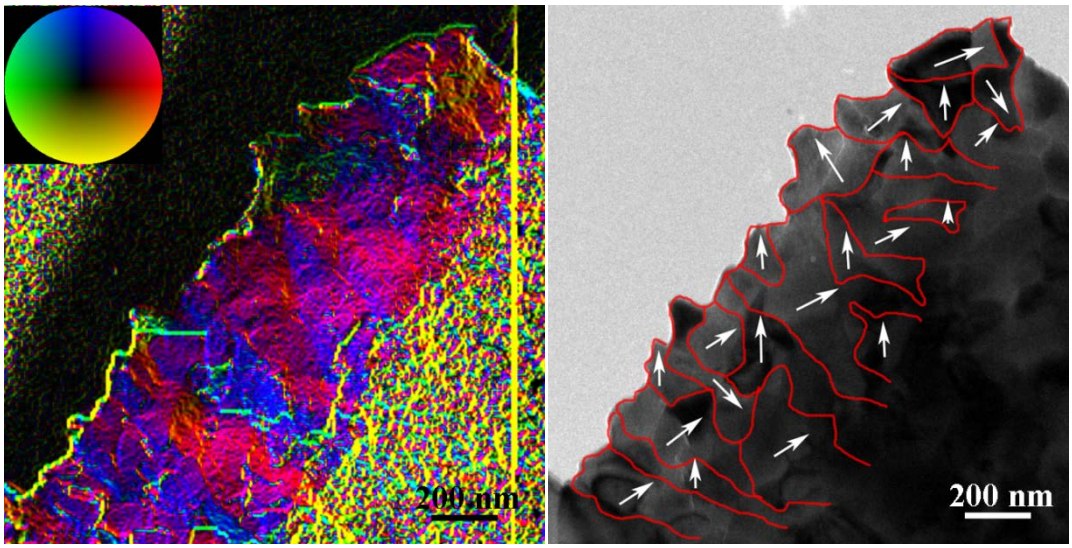

Fig.71. Off-axis electron holography (Left) electron gradient map and (Right) Lorentz image with magnetic domains labeled.

In the image on the right, the white arrows indicate the direction of magnetic induction for each domain that shown outlined in red. It is important to note that the magnetic domain often comprise of several physical crystal grains, or portions of several grains, otherwise known as multi-grain domains (MGD). The size and geometry of the magnetic domains are affected by crystal structure, and the magnetic domain boundaries often follow and coincide with the column boundaries. A statistical analysis indicates that the magnetic domain boundaries coincide with the physical grain boundaries 41.55% of the time.

In hard magnets comprising of large grain structures, the domains divide into regions of 90° or 180° magnetic orientations in order to lower the external stray energy field [5]. The 90° and 180° domains organize to accommodate internal flux closure to

prevent demagnetization of the hard magnet. Figure 72 illustrates 90° and 180° domains within a single crystal while Fig. 73 shows and example of nanocrystalline grains in an amorphous matrix of random anisotropy [5, 70].

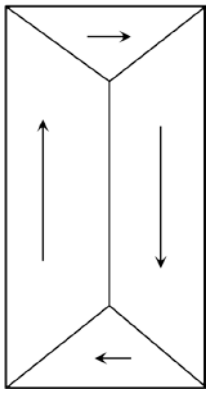

Fig. 72. Hard magnet

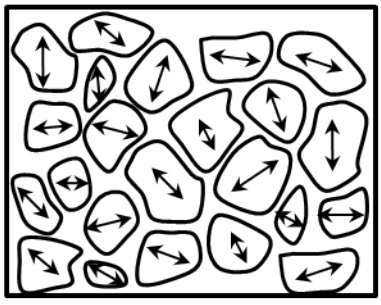

Fig. 73. A soft magnet with random anisotropy.

Thermodynamically, it is more advantageous to have the magnetic structure divided into domains that minimize the free energy, rather than be uniformly magnetized throughout in one direction [4]. In the electron holography image there are few, if any, 90° domain walls visible. In general the domains are aligned in Fig. 71 diagonally from bottom left to upper right; however they are not perfectly aligned. The material acts more like a soft magnetic material with nanocrystalline grains than a hard magnetic material.

Random Anisotropy Model.

The random anisotropy model best represents the magnetic domains in the Ni-Zn-Co ferrite thin films deposited using the spin-spray plating method. The ferrite films deposited display a multiphase material with nanocrystalline grains with amorphous boundary features shown in Figs. 66 – 71. Nanocrystalline texturing is often seen within what appears to be single grains that are less than 100 nm [70]. Particle reduction is a well know method to divide into single-domain particles, which increases the coercivity value to a maximum, controlled by the anisotropies [70].

The random anisotropy model (RAM) basically explains the high frequency and high permeability properties by considering exchange-coupled nanocrystals with uniaxial magnetocrystalline anisotropy, *K* [71]. The magnetocrystalline anisotropy is relates to the crystal symmetry, and for cubic crystals the easy axis has 6 major directions [70]. The fundamental idea to understanding the effect of magnetocrystalline anisotropy is to recognize that the grains are much smaller than the ferromagnetic exchange length, L_{ex}^{0},

the minimum length the magnetic moments are forced to align; which is given by Eqn. (24) [70].

$$L_{ex} = \sqrt{A/\langle K_1 \rangle} \tag{24}$$

Where A is the exchange stiffness (relates the exchange integral J_{hkl} with interaction parameter), and K_1 is the anisotropy [70, 72].

The magnetocrystalline anisotropy is averaged over the randomly fluctuating anisotropies, drawn in Fig. 51 [50, 70]. Essentially, ferromagnetically coupled grains, of size D, with magnetocrystalline anisotropies K_1 are oriented at random [50]. Within the volume of the exchange length, L_{ex}, the effective anisotropy, $\langle K \rangle$, is a product from the mean fluctuation amplitude of the anisotropy energy [50]. Hence, if the grain size, D, is less than the exchange length, L_{ex}, than [73]

$$\langle K \rangle = K_1 \cdot \left(\frac{D}{L_{ex}^0}\right)^6 = K_1^4 \cdot \frac{D^6}{A^3} \tag{25}$$

Equation (25) is true for three-dimensional structures; however spin-spray deposited ferrites are considered having a two-dimensional structure, so the equation changes to [50, 73]

$$\langle K \rangle = K_1^2 \cdot \frac{D^2}{A} \tag{26}$$

The dependence of grain size is still important, by an exponential factor of 2; however other factors also play a role.

The coercivity and initial permeability plays an important role in the random anisotropy model and are closely correlated to the effective anisotropy by Eqns. (27) and (28) in the case of two-dimensional materials [50].

$$H_c = p_c \frac{\langle K \rangle}{M_s} \approx p_c \frac{K_1^2}{M_s A} \cdot D^2 \tag{27}$$

$$\mu_i = p_i \frac{M_s}{\mu_0 \langle K \rangle} \approx p_\mu \frac{M_s A}{\mu_0 K_1^2} \cdot \frac{1}{D^2} \tag{28}$$

Where p_c and p_μ are dimensionless pre-factors close to unity [50, 70, 73].

There is not much data for two-dimensional materials with coercivity or initial permeability plots to compare the Ni-Zn-Co ferrite films with, however, Herzer started collecting data on three dimensional materials. He was able to find the critical grain size at which the exchange length begins to equal the grain size, $D = L_{ex} \approx 40$ nm, labeled in Fig. 74 [50]. If the grain size exceeds the domain wall width, domains form within the grain, and the coercivity and initial permeability decrease [50, 70].

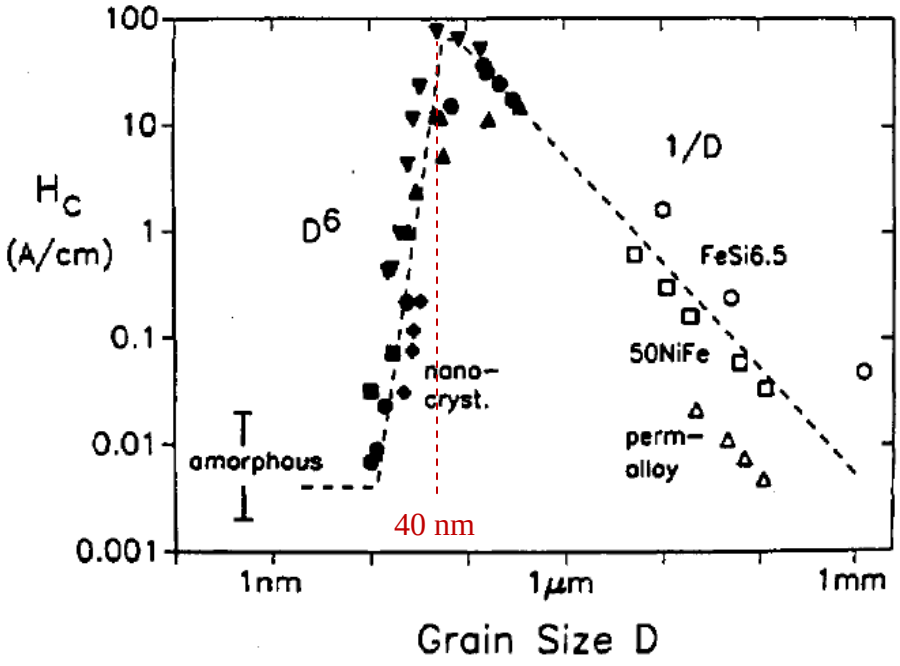

Fig. 74. Effect of grain size on coercivity for 3D materials made of magnetic metal alloys [50, 70].

Summary.

Multi-grain domains were experimentally observed definitively for the first time. Electron holographic imaging revealed the size of magnetic domains, L_{ex}, to be greater than the physical grain size (e.g., Fig. 71). Though spin-spray deposition exhibited soft magnetic properties within the plan of the film, such behavior is not exceeded in the third dimension [50, 70].

Chapter 5

LAMINATION OF THIN FILMS

This chapter discusses the lamination of Ni-Zn-Co spinel ferrites for antenna applications. This lamination procedure has been filed as a provision patent under the U.S. Application Serial No. 61/552,208, filed on October 27, 2011 [74].

PREPARATION

Thin films ferrites are prepared using the spin-spray deposition method. First, the metal chloride (Fe, Ni, Zn, Co, Mn, etc…) and oxidant solutions are prepared using deionized water. In this case the precursor is used for Ni-Zn-Co ferrite. It consists of iron chloride tetrahydrate, nickel chloride hexahydrate, zinc chloride, and cobalt chloride hexahydrate. The oxidizing solution is a mixture of sodium nitrite ($NaNO_2$), which acts as the oxidant, and sodium acetate (CH_3COONa) which buffers the solution ranging from a pH of 7.0 – 11.0. When the deposition is completed, distilled water is pumped through the entire system, washing the vessel, tubing, nebulizers and thin films for at least 20 minutes.

Substrate.

The substrate can ultimately have any thickness, in this case 12.5 - 25.4μm thick polyether ether ketone (PEEK) substrate was used. As seen from Fig. 75 and 76 depositing on a glass substrate gives a much more uniform coverage firmly attached to the surface than a thermoplastic substrate. However, the PEEK substrate has many

benefits such as its glass transition temperature (GTT), deformation properties, and coefficient of thermal expansion (CTE).

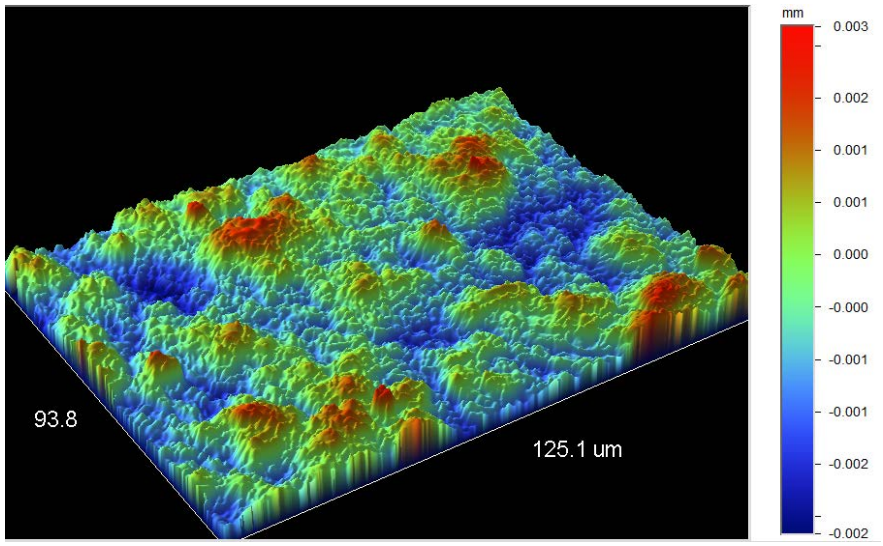

Fig. 75. Confocal microscope image of Ni-Zn-Co ferrite deposited on thermoplastic substrate.

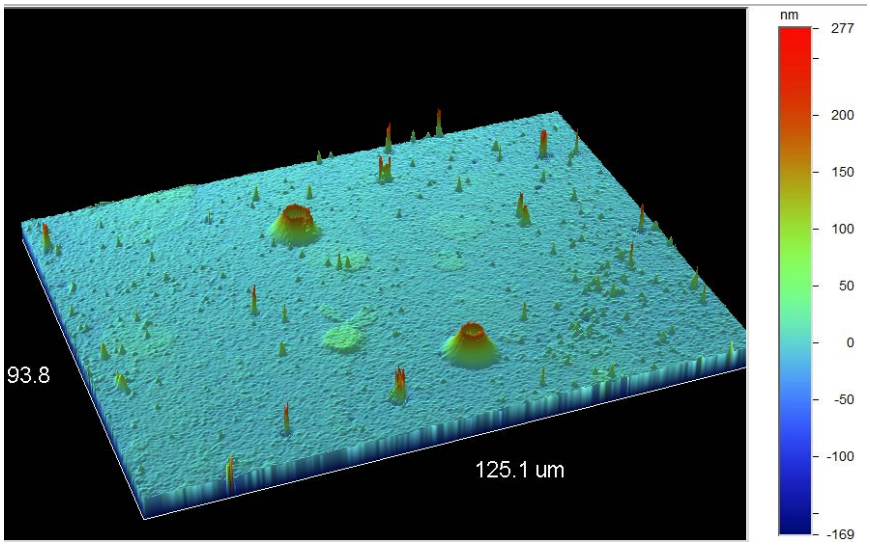

Fig.76. Confocal microscope image of Ni-Zn-Co ferrite deposited on glass substrate.

The GTT was measured using a differential scanning calorimeter (DSC) to measure the thermal transitions for the polymer and the thin film deposited onto the polymer [75]. According to the graph in Fig.77 the GTT of the PEEK is at 341°C, and it is an exothermic reaction. The DSC measures the sum of all heat flows, which makes it sometimes difficult to interpret the data, when measuring composites, however in the case of PEEK it straight forward [75]. When ferrite is deposited onto the substrate the GTT does not change.

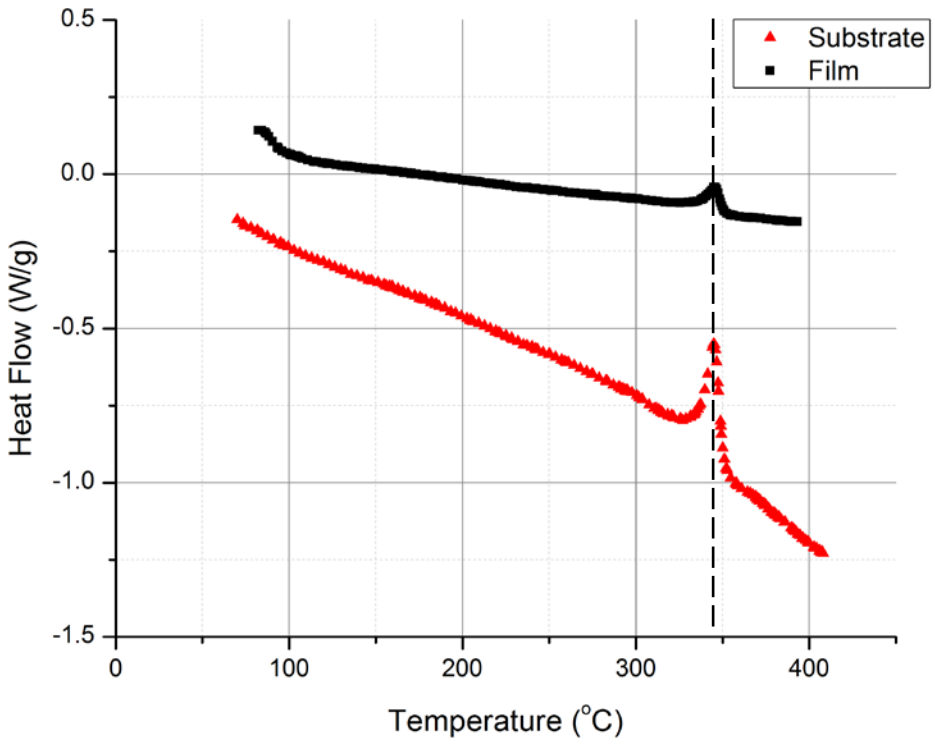

Fig. 77. The measured glass transition temperature of the plastic substrate in red and in black a deposited Ni-Zn-Co ferrite thin film same substrate.

LAMINATION

The second stage is preparing the films for lamination. After the films are washed and cooled down the reactor top is taken off and the nitrogen is blown carefully on the films to dry them off. The films are then cut to the desired size and stacked into layers with for the desired thickness and width.

Next, the stacked layers of Ni-Zn-Co ferrite are placed in between two aluminum blocks, *i.e.* laminate mold seen in Fig. 78. If needed, pressure is applied to keep the laminate mold closed tightly. Then the layered sample is placed into a 3-zone tube furnace and heated to 330 - 400ºC for about two hours in a helium atmosphere, in order to keep the ferrite from oxidizing. The temperature ramp rate is held at 15-50ºC/minute. When the cycle is finished the layered sample is left to cool down without disturbance at the same ramp rate.

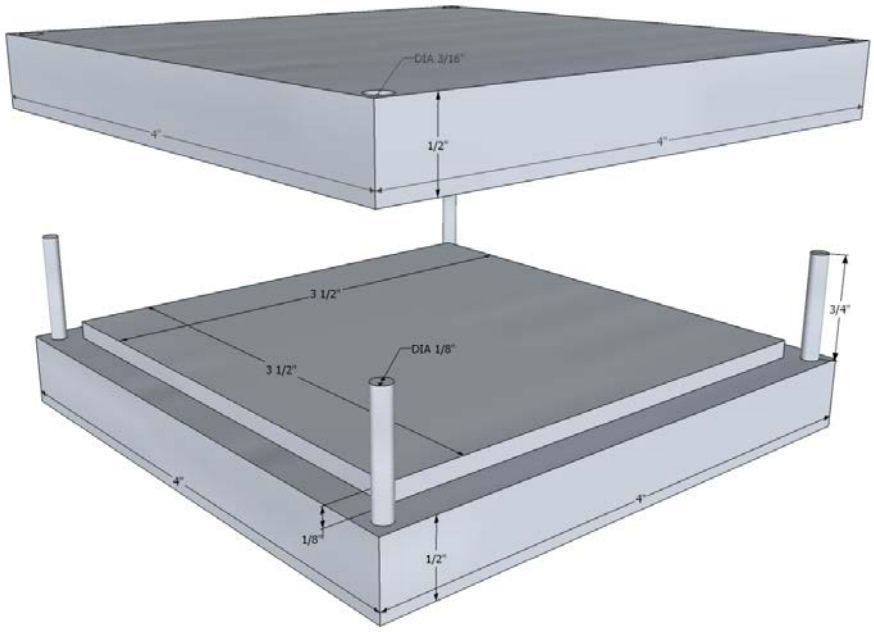

Fig. 78. Aluminum mold for thin film laminate.

Results.

Figure 79 shows an optical image of laminate of this method used on Ni-Zn-Co ferrite, and Table IV shows the characteristics of the layers used in this example. The final sample was 3" x 3" x 0.2", and each layer had 12 μm PEEK and 12 μm Ni-Zn-Co ferrite with approximately the same composition. To maximize the efficiency of this process the laminate was stacked in a mosaic; each layer could consist of 1, 2 or 3 separate sections to complete the layer. Since this laminate was too large to fit in the permeameter, Dr. Sergio Clavijo simulated the results using a prototype with the same samples, see Fig. 80 [76].

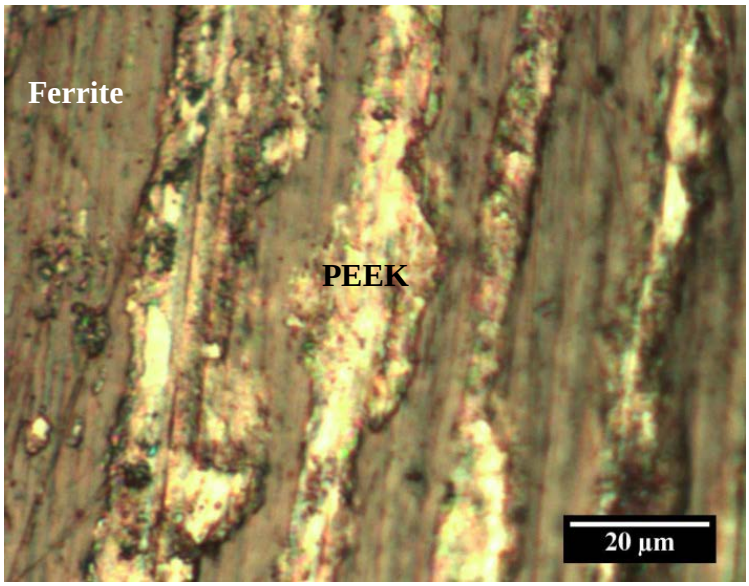

Fig. 79. Optical image of ferrite and PEEK layers.

Table IV. Characteristics of the individual sample layers for L111017.

Sample ID	Composition
NZCF20110927	$Ni_{0.19}Zn_{0.22}Co_{0.05}Fe_{2.54}$
NZCF20110930	$Ni_{0.19}Zn_{0.29}Co_{0.04}Fe_{2.48}$
NZCF20111004	$Ni_{0.20}Zn_{0.24}Co_{0.06}Fe_{2.50}$
NZCF20111006	$Ni_{0.16}Zn_{0.32}Co_{0.04}Fe_{2.48}$
NZCF20111101	$Ni_{0.43}Zn_{0.34}Co_{0.04}Fe_{2.19}$
NZCF20111102	$Ni_{0.37}Zn_{0.30}Co_{0.05}Fe_{2.28}$
NZCF20111107	$Ni_{0.18}Zn_{0.13}Co_{0.04}Fe_{2.65}$
NZCF20111108	$Ni_{0.37}Zn_{0.22}Co_{0.05}Fe_{2.36}$
NZCF20111110	$Ni_{0.31}Zn_{0.31}Co_{0.05}Fe_{2.34}$
NZCF20111114	$Ni_{0.24}Zn_{0.07}Co_{0.04}Fe_{2.64}$
NZCF20111115	$Ni_{0.29}Zn_{0.30}Co_{0.05}Fe_{2.37}$
NZCF20111116	$Ni_{0.27}Zn_{0.22}Co_{0.05}Fe_{2.45}$
NZCF20111117	$Ni_{0.31}Zn_{0.25}Co_{0.04}Fe_{2.40}$
NZCF20111129	$Ni_{0.34}Zn_{0.34}Co_{0.05}Fe_{2.27}$
NZCF20111130	$Ni_{0.28}Zn_{0.27}Co_{0.06}Fe_{2.40}$
NZCF20111201	$Ni_{0.27}Zn_{0.26}Co_{0.04}Fe_{2.43}$
NZCF20111202	$Ni_{0.35}Zn_{0.34}Co_{0.05}Fe_{2.26}$
NZCF20111203	$Ni_{0.35}Zn_{0.21}Co_{0.04}Fe_{2.44}$
NZCF20111204	$Ni_{0.30}Zn_{0.35}Co_{0.05}Fe_{2.30}$

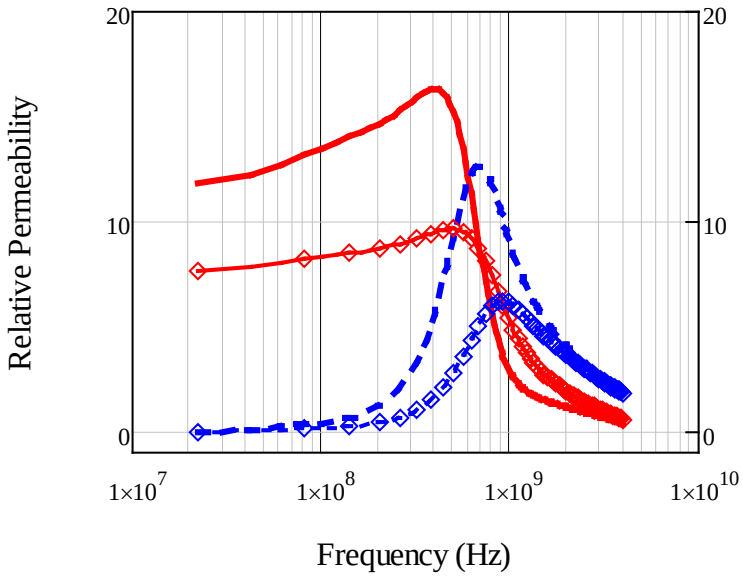

Fig. 80. Predicted permeability for a 3" x 3" x 0.2" laminate. The solid (red) and dashed (blue) curves represents the initial and imaginary permeability, respectively, if there are no pores or cracking in the laminate. The curves with symbols represent a small degree of cracking induced in the layering procedure.

SUMMARY

The spinel ferrite laminates have many applications in the high frequency range. The spin-spray deposition method provides an operation advantage synthesizing at low temperatures. The laminate applications include antennas, low-loss broadband communication devices, miniaturized low-microwave inductors, and electromagnetic noise suppressors.

Chapter 6

CONCLUSIONS & FUTURE WORK

Throughout this dissertation, the fabrication and characterization of nanocrystalline spinel ferrite thin films fabricated by the spin-spray deposition was examined and discussed. The spin-spray deposition method is an aqueous reaction that occurs at low temperature with the delivery of reactants via a dual spraying of metal chloride and oxidizing reactant onto a rotating platen. The basic principle behind the aqueous reaction is converting the iron oxidation states from Fe^{2+} to Fe^{3+}.

As demonstrated in chapter 4, the magnetic domain structure is considered multi-grain domain (MGD) with a complex nanocrystalline substructure. Understanding the magnetic properties through nanocrystalline magnetic domain behaviors became a large part of this project, which led to interpreting the data trend analysis. The MGD structure can be interpreted through the random anisotropy model, which is basically modeled after the idea that the ferromagnetic exchange length, L_{ex}, is larger than the grain size [50, 70, 73].

The optimum pH_{EFF} for deposition is found for depositing the optimum Ni-Zn-Co ferrite film in μ-droplet regime of the rotating platen. There is a steep decline in Snoek's product with an increase in deposition rate, which can be caused from the reaction kinetics of iron (Fig. 48), crystallite size, porosity, or cracking. The last three causes can

lead to a significantly lower Snoek's product value, in which the materials will act like a bulk powder.

To give an example of how well these films perform compared to others in literature, they have been plotted on the same graph as De-Sheng *et al.* [77]. He compares the anisotropy field from the hard plane (H_{a1}) and the easy plane (H_{a2}) to determine the Snoek's limit [77]. There is a line drawn in shown in black where H_{a1}/H_{a2} =1, which is equivalent to Snoek's limit for bulk materials (or spherical particle composites), in which the spinel ferrite thin films have exceeded, shown in Fig. 81 [77].

PROCESS IMPROVMENTS

Film Properties.

For the last four years, only a limited composition range has been targeted in order to understand the spin disc reactor better. As of late the processing mechanisms for the spin disc reactor were analyzed in chapter 3. The next step in this process, in which has already begun, is to map the different cation fractions contributing to spinel ferrite films, see Fig. 82, to see if there are any other compositions that can increase the frequency range into to GHz range while maintaining the Snoek's product.

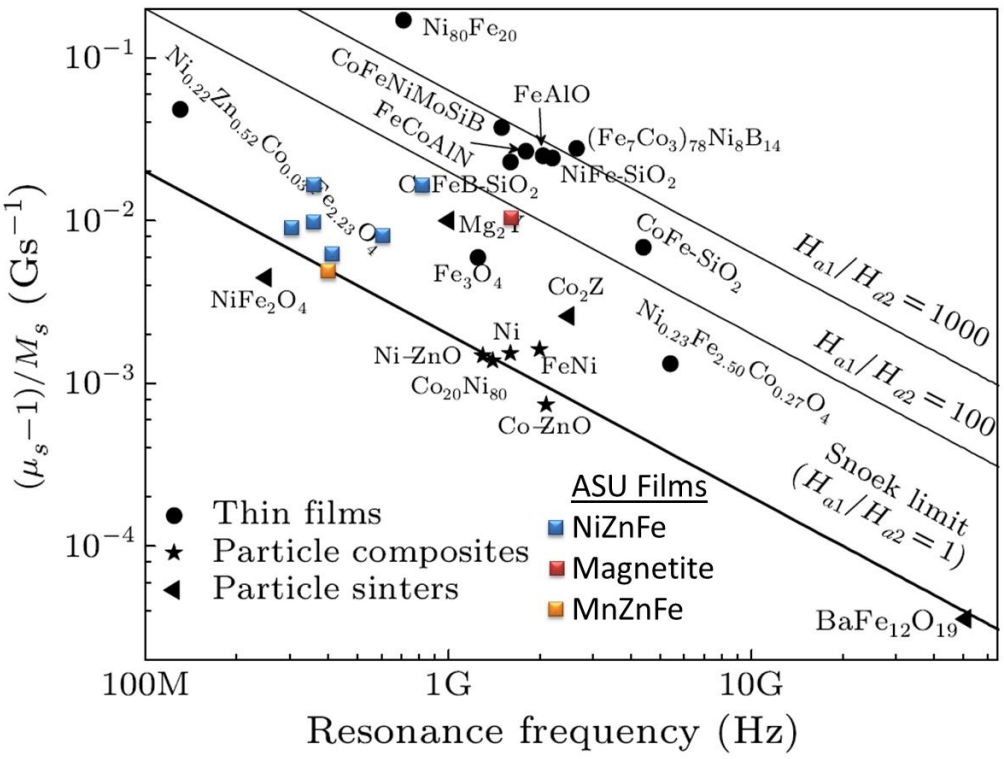

Fig. 81. The ratio of (μ-1)/M_s of various types of spinel ferrite thin films deposited using the spin-spray method plotted as a function of the resonance frequency [77].

Another improvement that could be made to the process is buffering the chloride solution. The metal chloride solutions used in this study have not been buffered, and ranges from 3.70 – 4.30. By varying the $pH_{Chloride}$ it will allow for morphology changes within the spinel structure, which in turn relates to the Snoek's product values.

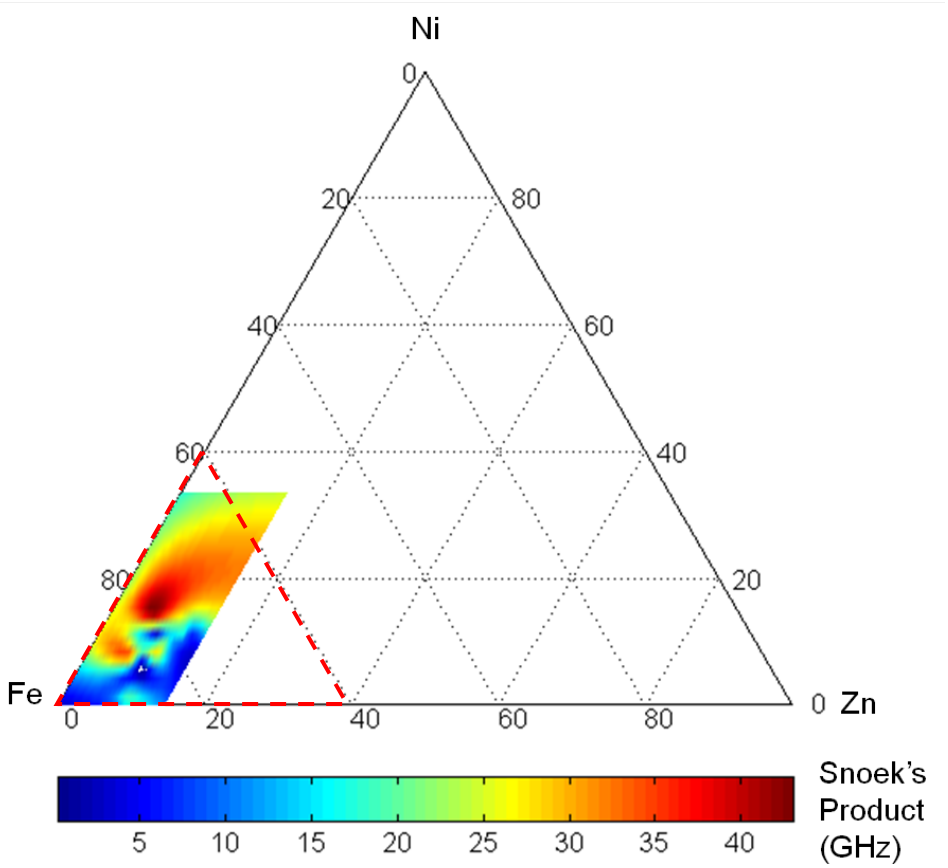

Fig. 82. Cation fraction map with highest Snoek's product labeled in red areas.

EXPERIMENTS

Environmental Testing.

Experimentally, the spinel ferrite films developed during the spin-spray deposition method need to be tested under extreme environments. Since Ni-Zn-Co ferrite films will be used for electromagnetic interference devices (EMI) they will need to be tested for thermal shock, hardness testing, and damp heat testing [78].

Thermal shock testing for ceramics depend not only on temperature change but mechanical and thermal properties as well [44]. It basically measures the ability of a material to withstand failure under rapid cooling [44]. Therefore it is best to have high fracture strengths, thermal conductivities, low elastic moduli, and low thermal expansion coefficient [44]. Since Ni-Zn-Co ferrite are brittle materials, thermal stresses as a consequence of thermal changes may lead to fracturing or plastic deformation [44]. The main sources of thermal stress are thermal expansion and temperature gradients during heating and cooling [44].

Next hardness testing is used, which measures a materials resistance to localized plastic deformation [44]. There are many different types of hardness tests including the Rockwell, Brinell, Vickers, and Knoop hardness tests. Hardness tests are very common tests to perform over other mechanical tests for several reasons. They are inexpensive, simple, and easy to learn since they have been studied for over 250 years [79]. It a near non-destructive test with only a small indent occurring during the test [44]. Another advantage using this test is through the hardness data other mechanical properties can be extrapolated, such as tensile strength [44]. In the case on Ni-Zn-Co spinel ferrite thin films the Vickers hardness test method would be applied, however, instead of using a microindenter, a nanoindenter would be used in order to test the individual columns.

The damp heating tests are proposed to be used to expose materials to environments for testing delamination, electrical and magnetic degradation behavior [80]. Damp heating experiments are usually performed for 1000 hours at 85°C in an 85%

humid environment. The experiment is rather extreme, and the failures seen in the experiments may not be seen in the field [80]. For thin film ferrites, the largest concern would be the substrate, especially if it were deposited onto a plastic. The polymer may absorb water, or deuterium, which in turn changes the electrical properties of the overall laminate.

The last test proposed would be measure the magnetic properties at different temperatures using the superconducting quantum interference device (or SQUID) from 10 K – 400 K (-263.15°C – 126.85°C). When the material is exposed to a higher or lower temperature, the area (i.e. loss) of the hysteresis loop will change due to disorder [6]. At higher temperatures the direction of dipole moments randomize, decreasing the area of the hysteresis and giving disorder with no net polarization [81]. Also phase transitions can be found during temperature cycles, it which there will be an increase in polarization [81]. The permeability is an important property that is strongly dependent on the temperature, and is one of the most important properties measured when evaluating the electromagnetic properties [6]. Figure 83 is an example extracted from Liu *et al*. depicting ferromagnetic behavior in synthesized cobalt ferrite nanoplatelets dispersed in ethanol [55].

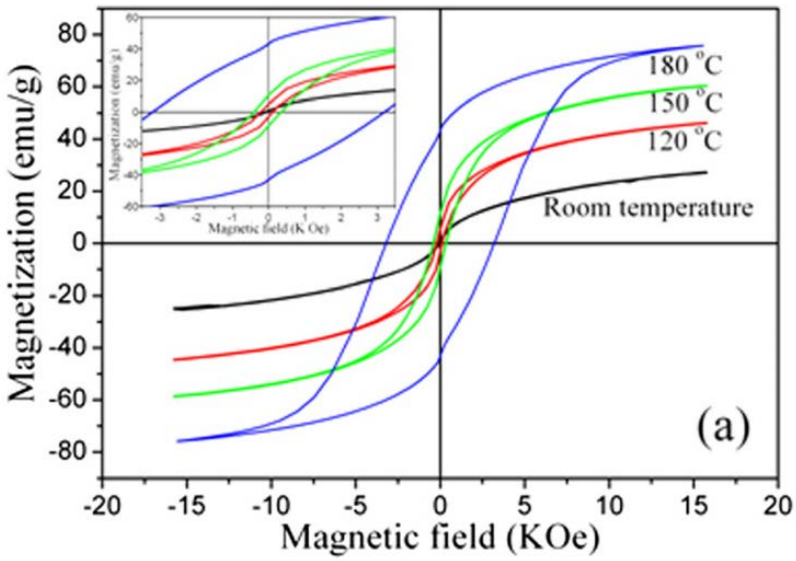

Fig. 83. Hysteresis loops of $CoFe_2O_4$ at different temperatures [55].

REFERENCES

1. Vishwakarma, R.K., *Dual-band stacked rectangular microstrip antenna for mobile applications.* Antenna Test and Measurement Society, 2010.

2. Kondo, K., et al., *Spin sprayed Ni(‾Zn)‾Co ferrite films with natural resonance frequency exceeding 3 GHz.* Journal of Applied Physics, 2007. **101**(9): p. 09M502.

3. W. D. Kingery, H.K.B., and D. R. Uhlmann, *Introduction to Ceramics*1960, New York: John Wiley and Sons, Inc. 1032.

4. Wijn, J.S.a.H.P.J., *Ferrites*1959, New York: John Wiley & Sons. 369.

5. Jiles, D., *Introduction to Magnetism and Magnetic Materials*. 2 ed1998, New York: Chapman and Hall. 536.

6. Goldman, A., *Modern Ferrite Technology*. 2 ed2006, Pittsburgh, PA: Springer. 438.

7. Snoek, J.L., *New Developements in Ferromagnetic Materials*1947, New York: Elsevier Publishing Company, Inc. 136.

8. Neelakanta, P.S., *Handbook of Electromagnetic Materials: Monolithic and Composite Versions and Their Applications*1995, Boca Raton, FL: CRC Press.

9. Nabuhiro Matsushita, T.N., and Masonori Abe, *Ni-Zn-Co Ferrite Films Prepared at 90 ºC Having μ'' = 30 at 3 GHz.* IEEE, 2002. **38**(5): p. 3.

10. Tamaura, M.A.Y., *Ferrite-Plating in Aqueous Solution: A New Method for Preparing Magnetic Thin Film.* Japanese Journal of Applied Physics, 1983. **22**(8).

11. Nobuhiro Matsushita, C.P.C., Tomohiro Mizutani, and Masanori Abe, *High-Rate Low-Temperature (90 ° C) Deposition of Ni-Zn Ferrite Films Highly Permeable in Gigahertz Range.* IEEE, 2002. **38**(5): p. 3156-3158.

12. M. Abe, A.I.S., N. Matsushita, and Y. Shimada, *Ferromagnetic Resonance Study on Magnetic Homogeneity in Spin-Sprayed NiZn Ferrite Films Highly Permeable at Gigahertz Frequencies.* IEEE, 2003. **39**(5): p. 3142-3144.

13. Nobuhiro Matsushita, M.T., Masataka Shigemori, and Masanori Abe, *High Deposition Rate Obtained for Spin-Sprayed Ni-Zn Ferrite Films Without Using Ammonia Ions.* IEEE, 2004. **40**(4): p. 2817-2819.

14. Lau, J.G.M.D., *Improvement of High-Frequency Properties of Iron-Deficient Ni-Zn-Co Ferrites by Reduction of Grain Size* IEEE, 1969. **5**(3): p. 1.

15. Matsushita, N., et al., *Ni–Zn ferrite films with high permeability (μ'=~30, μ''=~30) at 1 GHz prepared at 90 °C.* Journal of Applied Physics, 2002. **91**(10): p. 7376.

16. Tamaura, M.A.Y., *Ferrite plating in aqueous solution: New technique for preparing magnetic thin film.* Journal of Applied Physics, 1984. **55**(6): p. 3.

17. Abe, M., *Ferrite plating: a chemical method preparing oxide magnetic films at 24–100 °C, and its applications.* Electrochimica Acta, 2000. **45**: p. 7.

18. Makoto Ojima, F.S., Yoshitaka Kitamoto and Masanori Abe, *Ultrasound Enhanced Ferrite Plating of Polymer Microspheres for Magnetic Cellular Segregation.* IEEE, 1999. **35**(5): p. 3.

19. Nabuhiro Matsushita, T.N., and Masonori Abe, *Spin-sprayed Ni-Zn-Co ferrite films with high μr''>100 in extremely wide frequency range 100 MHz-1 GHz.* Journal of Applied Physics, 2003. **3**(10): p. 7133-7135.

20. Matsushita, N., et al., *Ni-Zn ferrite films synthesized from aqueous solution usable for sheet-type conducted noise suppressors in GHz range.* Journal of Electroceramics, 2006. **16**(4): p. 557-560.

21. Wagata, H., et al., *Single-Step Fabrication of ZnO Rod Arrays on a Nonseeded Glass Substrate by a Spin-Spray Technique at 90 °C.* Crystal Growth & Design, 2010. **10**(8): p. 3502-3507.

22. P. J. van der Zaag, P.L., Y. Kitamota & M. Abe, *The permeability of plated ferrite films.* IEEE, 1999. **35**(5): p. 3.

23. Peter Lubitz, S.H.L., Frederic J. Rachford and Brian J. Rappoli *Effects of Annealing on the Microwave Properties of Spin-Spray Ni-Zn Ferrites.* IEEE, 1994. **30**(6): p. 3.

24. Zhang, Q., et al., *Preparation of NiZn ferrite films by spin-spray ferrite plating on oxygen-plasma-treated substrates.* Journal of Applied Physics, 1993. **73**(10): p. 6284.

25. Lu, N.X.S.K., *Grain-size limit of polycrystalline materials.* Physical Review B, 1999. **59**(9): p. 3.

26. Liu, M., et al., *Spin-spray deposited multiferroic composite $Ni_{0.23}Fe_{2.77}O_4/Pb(Zr,Ti)O_3$ with strong interface adhesion.* Applied Physics Letters, 2008. **92**(15): p. 152504.

27. Scherer, C.J.B.a.G.W., *Sol-Gel Science: The Physices and Chemistry of Sol-Gel Processing*1990, Boston: Academic Press Inc. 462.

28. D.M. Dobkin, M.K.Z., *Principles of Chemical Vapor Deposition*2003, Netherlands: Kluwer Academic Publishers. 279.

29. Nabuhiro Matsushita, T.N., and Masonori Abe, *Ni-Zn-Co ferrite films prepared at 90C having μ"=30 at 3 GHz.* IEEE, 2002: p. BW 11.

30. Ray, N.M., *SDR III System Flow Chart*, 2012.

31. Donald A. Palmer, P.B.a.D.J.W., *Solubility of Nickel Oxide and Hydroxide in Water*, in *Properties of Water and Steam*2004: Kyoto. p. 264-269.

32. PElERR TREMAINEI, R.V.M., AND G. R. SHIERHJAN, *A CALCULATION OF GIBBS FREE ENERGIES FOR FERROUS IONS AND THE SOLUBILITY OF MAGNETITE IN H2O AND D2O TO 300° C.* Thermochimica Acta., 1977. **19**: p. 287-300.

33. Ailoor, S.K., et al., *Coupling of MnZn-ferrite films onto electronic components by a novel solution process for high frequency applications.* Journal of Materials Chemistry, 2009. **19**(31): p. 5510.

34. Nobuhiro Matsushita, C.P.C., Tomohiro Mizutani, and Masanori Abe, *High Rate Low-Teperature (90 °C) Deposition of Ni-Zn Ferrite Films highly Permeable in Gigahertz Range.* IEEE, 2002. **38**(5): p. 3156-3158.

35. Abe, M., *Nano-Crystalline and Thin Film Magnetic Oxides*. High Technology, ed. M.A. Ivan Nedkov. Vol. 72. 1998, Netherlands: Kluwer Academic Publisher.

36. Petuskey, W.T., *Growth Hypothesis*, 2011: PowerPoint.

37. Lorzel, H., *Particle Traces Colored by Particle Z Velocity (m/s)*, in *Computation Fluid Dynamics (CFD)*2010.

38. Lorzel, H.M., *Comparisons With Experimental Results Attempt to Establish a Correlation Between Computed Fluid Variables and Observed Film Growth*, in *FLUENT*2012.

39. Rose, H.H., *Optics of high-performance electron microscopes.* Science and Technology of Advanced Materials, 2008. **9**(1): p. 014107.

40. Paul Barnes, T.C., Simon Jacques *Advanced Certificate in Powder Diffraction on the Web*. Bragg's Law, 2006.

41. Tom Sebastian, S.A.C., and Rodolfo E. Diaz, *Improved accuracy thin film permeability extraction for a microstrip permeameter.* Journal of Applied Physics, 2012: p. 8.

42. Diaz, R.E., W.M. Merrill, and N.G. Alexopoulos, *Analytic framework for the modeling of effective media.* Journal of Applied Physics, 1998. **84**(12): p. 6815.
43. *MDI Jade 9.0*, 2011.

44. William D. Callister, J., *An Introduction to Materials Science and Engineering*. 7 ed2007, New York: John Wiley & Sons Inc.

45. Cullity, B.D., *Introduction to Magnetic Materials*1972, Canada: Addison-Wesley Publishing Co., Inc. 666.

46. Ray, N.M., *Cation Fraction versus Snoek's Product*, in *MatLab*2013, MatLab.
47. de Lacheirrerie, E.D.T., *Magnetism: Materials and Applications*2005, New York: Springer Publishing.

48. Lui Yi, D.S., and David J. Sellmyer, *Handbook of Magnetic Material*. Vol. 1. 2006, New York: Springer Publishing.

49. Herzer, G., *GRAIN SIZE DEPENDENCE OF COERCIVITY AND PERMEABILITY IN NANOCRYSTALLINE FERROMAGNETS.* IEEE, 1990. **26**(5): p. 1397 - 1402.

50. Herzer, G., *Nanocrystalline Soft Magnetic Materials.* Physica Scripta, 1993. **T49**: p. 307 - 314.

51. Abe, M., et al., *Phenomenological theory of permeability in films having no in-plane magnetic anisotropy: Application to spin-sprayed ferrite films.* Journal of Applied Physics, 2006. **99**(8): p. 08M907.

52. Yoshikawa, H., et al., *TEM observations of magnetic domains and grain boundaries on spin-sprayed ferrite films exhibiting high permeability usable for gigahertz noise suppressors.* IEEJ Transactions on Electrical and Electronic Engineering, 2007. **2**(4): p. 445-449.

53. E. C. STONER, F.R.S.A.E.P.W., *A MECHANISM OF MAGNETIC HYSTERESIS IN HETEROGENEOUS ALLOYS.* IEEE, 1991. **27**(4): p. 3475 - 3518.

54. Chinnasamy, C.N., et al., *Unusually high coercivity and critical single-domain size of nearly monodispersed CoFe[sub 2]O[sub 4] nanoparticles.* Applied Physics Letters, 2003. **83**(14): p. 2862.

55. Liu, W., et al., *Understanding the formation of ultrafine spinel CoFe2O4 nanoplatelets and their magnetic properties.* Journal of Applied Physics, 2012. **112**(10): p. 104306.

56. Sarkar, D., M. Mandal, and K. Mandal, *Domain controlled magnetic and electric properties of variable sized magnetite nano-hollow spheres.* Journal of Applied Physics, 2012. **112**(6): p. 064318.

57. R. DAY , M.F., and V.A. SCHMIDT, *HYSTERESIS PROPERTIES OF TITANOMAGNETITES: GRAIN-SIZE ANDCOMPOSITIONAL DEPENDENCE.* Physics of the Earth and Planetary Interiors, 1977. **13**: p. 260-267.

58. Dunlop, D.J., *The rock magnetism of fine particles.* Physics of Earth and Planetary Interiors, 1981. **26**: p. 1-26.

59. C. Kittel, J.K.G., *Ferromagnetic Domain Theory.* Solid State Physics, 1956. **3**: p. 437 - 564.

60. Kittel, C., *Theory of the Structure of Ferromagnetic Domains in Films and Small Particles.* Physical Review, 1946. **70**(11-12): p. 965-971.

61. Diaz, R.E., *Interim Report,* 2007, Arizona State University.

62. Subramani, A.K., et al., *A simple process for ferrite film preparation from one solution without using hazardous oxidizing agent.* Journal of Applied Physics, 2007. **101**(9): p. 09M504.

63. Tamaura, M.A.Y., *Ferrite-Plating in Aqueous Solution: A New Method for Preparing Magnetic Thin Films.* Journal of Applied Physics, 1983. **22**(8): p. 3.

64. Subramani, A.K., et al., *NiZnCo ferrite films by spin spray technique: morphology and magnetic properties.* Journal of Materials Science, 2007. **43**(7): p. 2372-2376.

65. Matsushita, N., T. Nakamura, and M. Abe, *Spin-sprayed Ni–Zn–Co ferrite films with high $\mu r''>100$ in extremely wide frequency range 100 MHz–1 GHz.* Journal of Applied Physics, 2003. **93**(10): p. 7133.

66. Kawano, K., et al., *The grain size effect on the magnetic properties in NiZn ferrite and the quality factor of the inductor.* Journal of Magnetism and Magnetic Materials, 2009. **321**(16): p. 2488-2493.

67. Sebastian, T., S.A. Clavijo, and R.E. Diaz, *Improved accuracy thin film permeability extraction for a microstrip permeameter.* Journal of Applied Physics, 2013. **113**(3): p. 033906.

68. D. V. Sridhara Rao, K.M.a.C.J.H., *TEM specimen preparation techniques.* Microscopy: Science, Technology, Applications and Education, 2010. **2**: p. 1232 - 1244.

69. Lorzel, H., *Contours of Wall Film Height*, in *FLUENT*2011.

70. Herzer, G., *THE RANDOM ANISOTROPY MODEL: A Critical Review And Update.* NATO Science Series II: Mathematics, Physics and Chemistry, 2005. **184**: p. 15.

71. Buschow, K.H.J., *Handbook of Magnetic Materials*. Vol. 18. 2009, Great Britain: Elsevier.

72. Velle, L.R., *New topics in Condensed Matter Research*, 2007, Nova Science Publishers, Inc.: New York. p. 221.

73. Herzer, G., *Magnetization process in nanocrystalline ferromagnets.* Materials Science and Engineering: A, 1991. **133**: p. 1 - 5.

74. Ray, W.T.P.a.N.M., *Thin Film ferrite Lamination Method*, 2011.

75. Nielsen, S., *Food Analysis*2010, New York: Springer. 602.

76. Clavijo, S., *Predicted permeability for a laminated spinel ferrite.*, 2011: Year end report, 2011. p. Predicted permeability for a laminated 3” x3” x0.2” ferrite. The solid and dashed curves show the permeability of the laminated ferrite if cracking would be zero. The curves with symbols represent the expected permeability when a small degree of cracking is induced in the layering procedure.

77. De-Sheng, X., *Bianisotropy Picture of Higher Permeability at Higher Frequencies.* Chin. Phys. Lett., 2008. **25**(11).

78. Hall, J.R.J.P.S., *Handbook of Microstrip Antennas*. Vol. 1. 1989, London: Peter Peregrinus Ltd. 1295.

79. Walley, S.M., *Historical origins of indentation hardness testing.* Materials Science and Technology, 2012: p. 17.

80. Owen, J.I., *Growth, Etching, and Stability of Sputtered ZnO:AI for Thin-Film Silicon Solar Cells*2011, Zentralbibliothek: Forschungszentrum Jülich. 192.

81. *Temperature dependence of the Hysteresis loop*. 2004-2012; Available from: http://www.doitpoms.ac.uk/tlplib/ferroelectrics/temp_dependence.php.

82. Lorzel, H., *Simulation of complex permeability effects on domain*, in *FLUENT*2012. p. Simulations of real and imaginary permeability for single and multi-domain grains.

APPENDIX A

SDR SYSTEMATICS

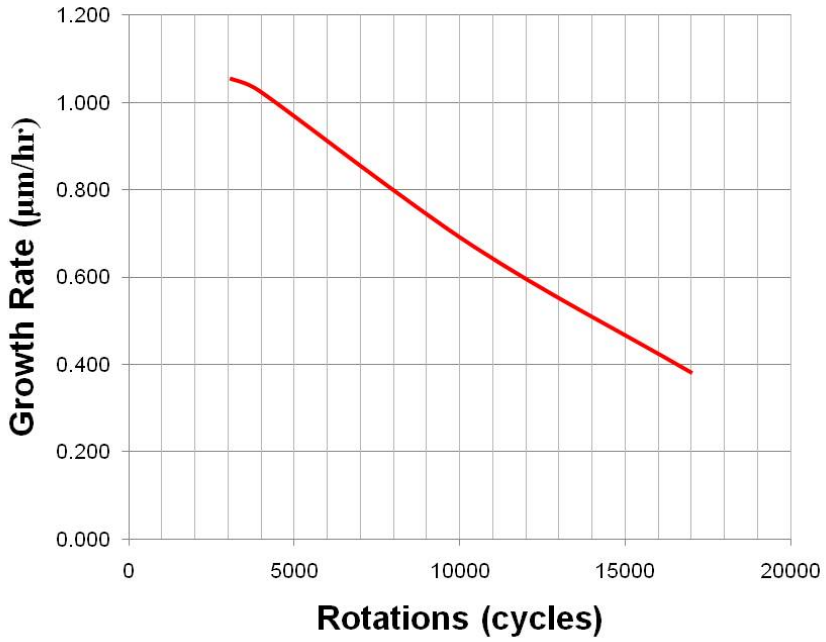

Fig. 84. Effect of number of cycles, or rotations, on growth rate.

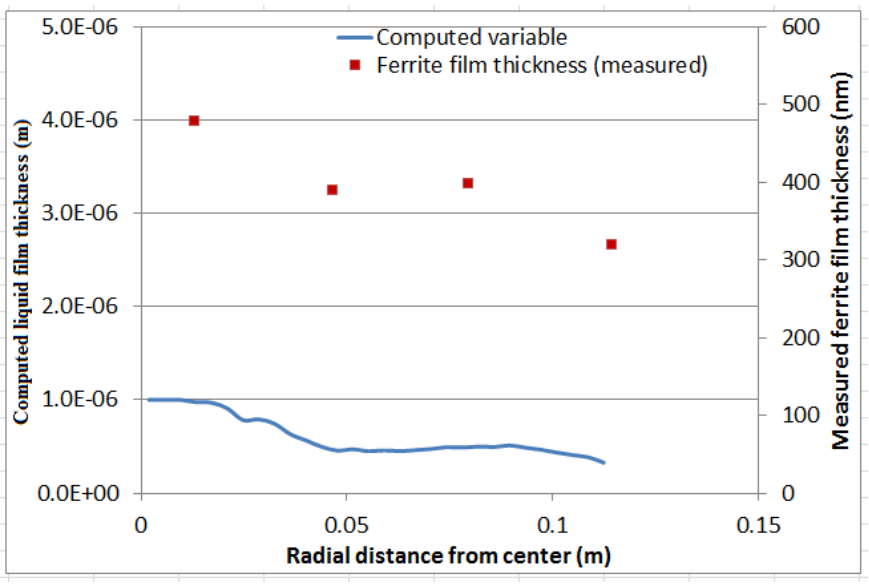

Fig. 85. Computed variable for droplet density represented as average liquid film height [82].

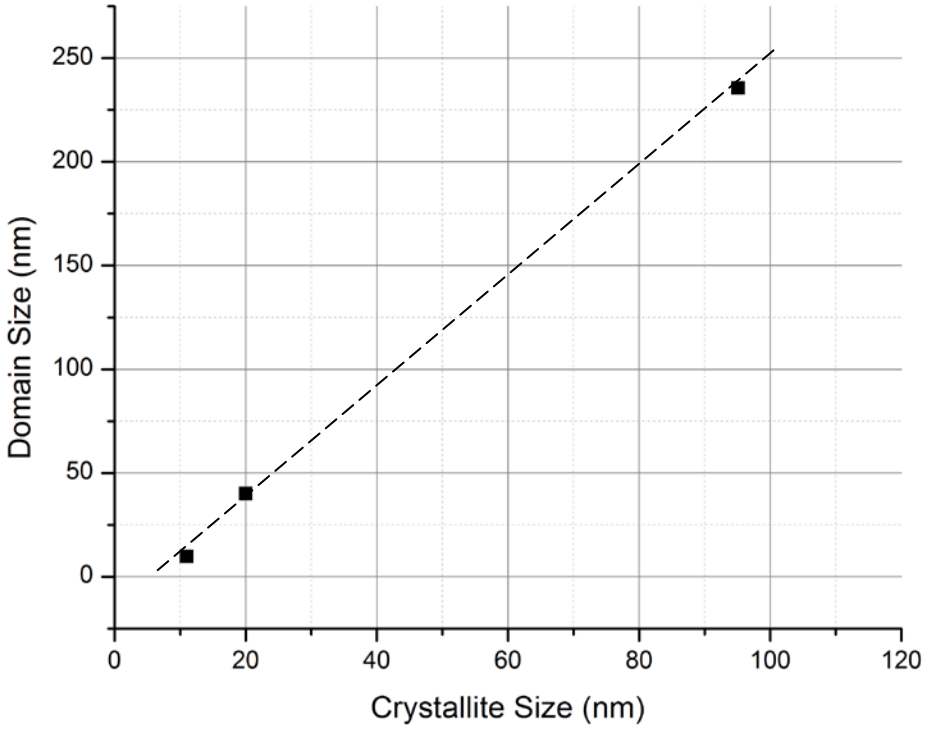

Fig. 86. Domain size effect with crystallite size, extrapolated data from journal articles and ASU data [54, 55].

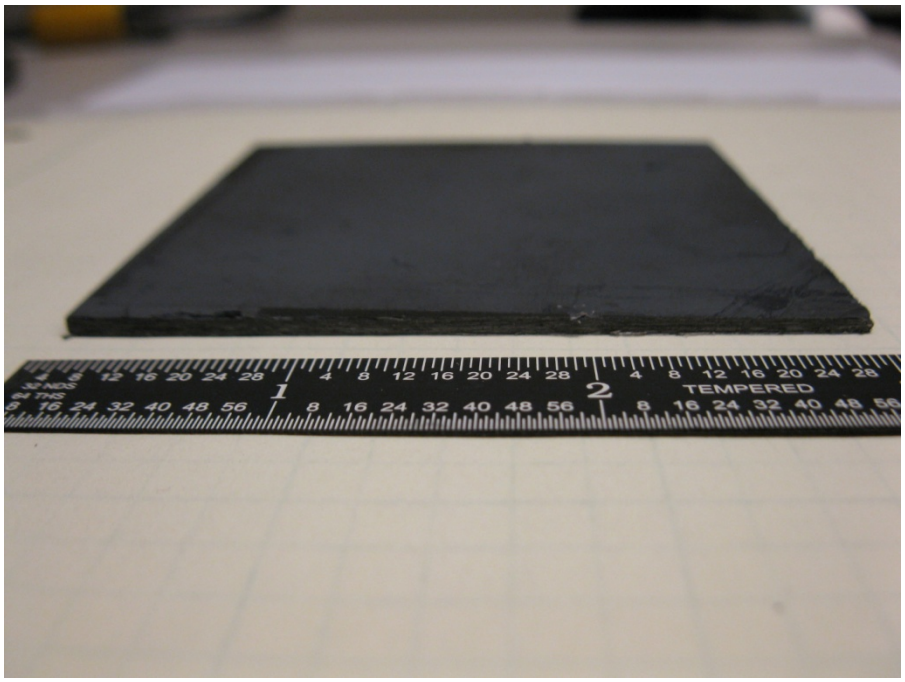

Fig. 87. Laminate, L111214, developed using the thin film lamination method.